Finanziato dall'Unione europea NextGenerationEU
Ministero dell'Università e della Ricerca
Italiadomani PIANO NAZIONALE DI RIPRESA E RESILIENZA
Università degli Studi di Messina

Department of Chemical, Biological, Pharmaceutical and Environmental Sciences

Ph.D. Course in Applied Biology and Experimental Medicine

Curriculum: Pharmaceutical Sciences

XXXVIII CYCLE

S.S.D. CHEM-07/A

In Silico Strategies To Identify Novel Dermatological Agents Targeting Elastase And Tyrosinase Enzymes

PhD Thesis of:

Giovanna Pitasi

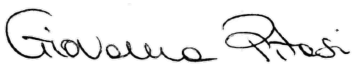

Supervisor:

Prof. Laura De Luca

Coordinator of Ph.D. course:

Prof. Emanuela Esposito

2024/2025

INDEX

ABSTRACT

Skin disorders arise from dysregulation in the main molecular pathways responsible for maintaining the integrity of the extracellular matrix, pigmentation homeostasis, immune regulation, and cell transformation. Among the biological targets involved in these processes, elastase and tyrosinase play a key pathological role. Their overactivity contributes, respectively, to the deterioration of the extracellular matrix associated with skin aging and inflammation, and to the alteration of melanogenesis leading to hyperpigmentation. Consequently, the discovery of selective elastase and tyrosinase inhibitors represents a promising therapeutic strategy for the treatment of dermatological conditions.

In recent years, computer-aided drug design (CADD) techniques have established themselves as powerful tools for simplifying the identification of effective compounds and accelerating the optimization of small bioactive molecules. By providing virtual screening of large compound libraries and rational design of new chemical patterns, CADD significantly reduces costs, trial times, and failure rates in new drug discovery.

This doctoral research project focused on the computational exploration of these two enzyme targets, with the aim of identifying new inhibitory chemotypes with potential dermopharmaceutical applications. Additionally, the training period at Farmacia Marra srl. allowed me the opportunity to evaluate commercially available formulations, offering a practical perspective to complement the theoretical framework. The opening chapters provide an overview of CADD methodologies and summarize the structural, biological, and therapeutic relevance of elastase and tyrosinase, along with the current landscape of commercialized inhibitors. (Chapters 1 and 2). In the subsequent chapters, my experimental studies on the enzyme elastase (Case study 1) and on tyrosinase (Case study 2) are described, which led to the identification of novel inhibitors.

Case study 1 focuses on the identification of new non-peptide elastase inhibitors. The first part reports on the research work accomplished during an experience at the University of Chemistry and Technology, Prague, Czech Republic, under the supervision of Prof. Andrea Brancale. A combination of structure-based drug modelling, alanine scanning, molecular docking, and molecular dynamics simulations guided the design and prioritization of candidate molecules. The selected compounds were synthesized, and

their biological activity was assessed in collaboration with the research group of Prof. Antonella Fais (University of Cagliari), leading to the identification of promising structures. Furthermore, collaboration with the research group of Prof. Domenico Trombetta (University of Messina) enabled the evaluation of natural extracts as elastase inhibitors. (Chapter 3)

Case study 2 focuses on the rational development of new tyrosinase inhibitors. Several series of compounds were designed and evaluated computationally to determine their binding affinity and interaction profile. Subsequent biological validation, performed in collaboration with the research groups of Prof. Antonella Fais (University of Cagliari), Prof. Scheuermann, Jörg (Institute of Pharmaceutical Sciences, ETH Zürich), and Prof. Maria Paola Germanò (University of Messina), confirmed the inhibitory activity against *Agaricus bisporus* tyrosinase and human tyrosinase. The antioxidant activity of the most promising derivatives was also evaluated. Furthermore, collaboration with Prof. Paola Bonaccorsi's group (University of Messina) has enabled the evaluation of derivatives that incorporate a well-established tyrosinase inhibitor pharmacophore conjugated to fluorophores, with the aim of studying their dual potential as therapeutic agents and imaging probes. (Chapter 4)

Overall, this PhD thesis combines computational chemistry and experimental validation to promote the discovery of new modulators of enzymes relevant to dermatology, laying the basis for future optimization towards effective treatments for skin disorders.

ABBREVIATION LIST

AbTYR – Tyrosinase from *Agaricus bisporus*
ADMET – Absorption, Distribution, Metabolism, Excretion, and Toxicity
ALI – Acute Lung Injury
ARDS – Acute Respiratory Distress Syndrome
CADD – Computer-Aided Drug Design
ECM – Extracellular Matrix
ELN – Elastin
EMA – European Medicines Agency
FDA – Food and Drug Administration
GA – Genetic Algorithm
GB – Generalized Born
GOLD – Genetic Optimization for Ligand Docking
HaCaT – Human keratinocyte cell line
HNE – Human Neutrophil Elastase
HTVS – High-Throughput Virtual Screening
hTYR – Human tyrosinase
LBDD – Ligand-Based Drug Design
MM-GBSA – Molecular Mechanics Generalized Born Surface Area
MM-PBSA – Molecular Mechanics Poisson-Boltzmann Surface Area
NMR – Nuclear Magnetic Resonance
PAINS – Pan-Assay Interference Compounds
PPE – Pancreatic Porcine Elastase
QSAR – Quantitative Structure–Activity Relationship
RMSD – Root-Mean-Square Deviation
SAR – Structure–Activity Relationship
SASA – Solvent Accessible Surface Area
SBDD – Structure-Based Drug Design
SPF – Sun Protection Factor
TYRP1 – Tyrosinase Related Protein 1
TYRP2 – Tyrosinase Related Protein 2
UV – Ultraviolet
UVB – Ultraviolet B
VDss – Volume of Distribution at Steady State
VS – Virtual Screening
VSGB – Variable Soft-Sphere Generalized Born

LIST OF PUBLICATIONS

I. *Investigating the ligand-binding properties of N-Arylbenzimidazoles as novel elastase Inhibitors.* **Pitasi, G**, Floris, S, Mancuso, F, Savoca, G, Gitto, R, Fais, A, De Luca, L; ChemMedChem, **2025**.

II. *Depigmenting action and bioimaging of luminescent BODIPY-based piperazinyl phenol derivatives.* Mirabile, S, Barattucci, A, Bonaccorsi, PM, Calderaro, A, De Luca, L, Germanò, MP, Gitto, R, Giuffrida, A, Monforte, M, Patanè, GT, **Pitasi, G,** Gangemi, CMA. Bioorganic Chemistry **2025**

III. *Structure-based design and evaluation of tyrosinase inhibitors targeting both human and mushroom isozymes*. Mirabile S, **Pitasi G**, Floris S, Schira K, Khettabi L, Soler-Lopez M, Scheuermann J, Gitto R, Germanò MP, Fais A, De Luca L. RSC Med Chem. **2025**

IV. *Computational Approach to Identifying New Chemical Entities as Elastase Inhibitors with Potential Antiaging Effects.* **Pitasi G**, Brancale A, Floris S, Fais A, Gitto R, De Luca L. Int J Mol Sci. **2024**

V. *Exploitation of the nitro- and/or 4-Trifluoromethyl-decorated phenyl fragment to develop small inhibitors of Alpha-Syn fibril aggregation.* **Pitasi G**, Fornt-Suñé M, Bucolo F, Gitto R, Ventura S, De Luca L. Bioorg Med Chem Lett. **2024**

VI. *Ligand-Based Discovery of a Small Molecule as Inhibitor of α-Synuclein Amyloid Formation.* De Luca L, Vittorio S, Peña-Díaz S, **Pitasi G**, Fornt-Suñé M, Bucolo F, Ventura S, Gitto R. Int J Mol Sci. **2022**

VII. *In Silico Insights towards the Identification of SARS-CoV-2 NSP13 Helicase Druggable Pockets.* Ricci F, Gitto R, **Pitasi G**, De Luca L. Biomolecules. **2022**

Chapter 1

DRUG DISCOVERY APPROACHES AND COMPUTATIONAL TOOLS

1.1 OVERVIEW OF THE DRUG DISCOVERY PIPELINE

Drug research and development represents a highly complex and multidisciplinary process comprising several sequential phases, including drug discovery, clinical evaluation, and regulatory authorization for production. Among these stages, drug discovery is particularly demanding in terms of both time and financial investment, often extending over several years and requiring expenditures of millions of dollars. This phase generally involves identifying targets, discovering and optimising leads, and conducting a preclinical assessment.[1,2] (Figure 1)

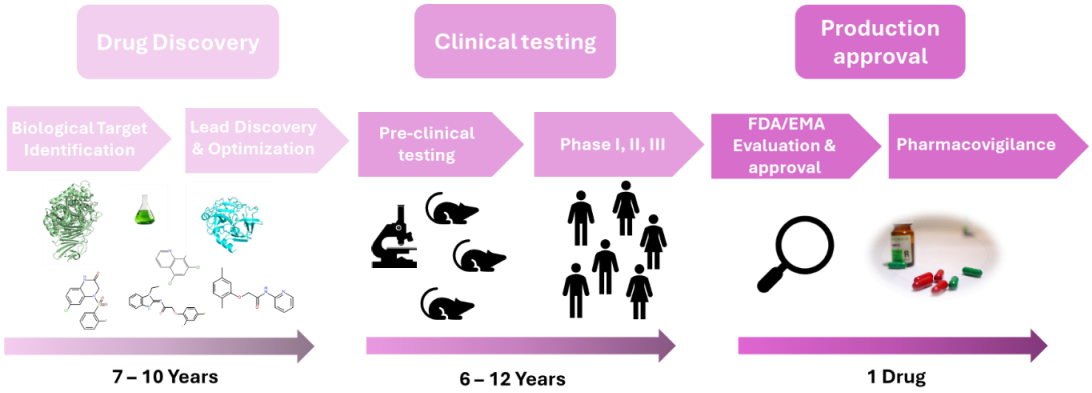

Figure 1: Overview of the drug discovery pipeline.

In the conventional paradigm, drug discovery typically begins with the identification of a pathological condition, followed by the selection of an appropriate biological target, the rational design and synthesis of biologically active compounds, and subsequent preclinical testing. Despite the continuous improvement of experimental methodologies, the overall success rate of clinical trials remains below 15%. Notably, approximately 50% of failures in drug discovery are associated with suboptimal pharmacokinetic and pharmacodynamic profiles, collectively designated as ADMET (Absorption, Distribution, Metabolism, Excretion, and Toxicity).

Over the past decades, the introduction of computational approaches has markedly enhanced both the efficiency and predictive accuracy of the drug discovery process. Nonetheless, the development of novel therapeutic agents continues to represent a time-

consuming and costly effort. To overcome the limitations of traditional experimental screening, modern drug discovery increasingly integrates computational methodologies that enable the virtual assessment of compounds in early research phases. The advent of high-throughput virtual screening (HTVS) has been a breakthrough, allowing the evaluation of millions of molecules per day.[3]

This acceleration, together with advances in structural biology and spectroscopic techniques, has established virtual screening and computer-aided drug design (CADD) as fundamental components of contemporary drug discovery. While preclinical and clinical stages remain inherently resource-intensive due to strict safety and efficacy requirements, the early discovery phase is more amenable to acceleration through computational approaches. Overall, the integration of computational tools within the drug discovery pipeline has substantially improved the exploration of chemical space and reduced attrition rates. By enhancing both the efficiency and rationality of candidate identification, computational drug design has become a cornerstone of next-generation pharmacological innovation.[1,4]

1.2 COMPUTER-AIDED DRUG DESIGN (CADD)

CADD plays a key role in drug discovery, integrating computational methodologies with biochemical and pharmacological knowledge. Its multidisciplinary nature allows for the rapid screening and optimization of drug candidates, improving the efficiency and accuracy of pharmaceutical research in the early stages. By predicting molecular behaviour and drug-target interactions, CADD contributes significantly to reducing experimental costs and failure rates in the drug development pipeline.[5]

CADD includes a wide range of computational strategies, all aimed at supporting the discovery and development of active compounds with favourable biochemical properties. Various molecule libraries are regularly evaluated using methods such as pharmacophore modelling, virtual screening (VS), molecular docking, and quantitative structure-activity relationship (QSAR) analysis. Among these, virtual screening plays a particularly dominant role, enabling the rapid exploration of large chemical collections to identify successful structures with optimal binding properties. Importantly, VS methodologies

also contribute to drug repurposing, offering a strategic pathway to accelerate and reduce risks in drug discovery and development.[1]

Depending on the biological data available, CADD workflows are generally classified into ligand-based drug design (LBDD) and structure-based drug design (SBDD). SBDD approaches, including molecular docking, molecular dynamics simulations, and de novo modelling, leverage experimental or predicted protein structures to design molecules capable of optimal interactions within the target binding site. In contrast, the LBDD technique relies on data derived from known active ligands through QSAR modelling, similarity searches, and pharmacological hypothesis generation, enabling the prediction of new compounds when structural information on the target is limited. Although mechanically distinct, these methodologies share the common goal of virtually selecting and refining molecular entities to improve physicochemical profiles, pharmacokinetics, and ADMET safety characteristics, ultimately promoting high-quality lead compounds in drug development pipelines.[6] (Figure 2)

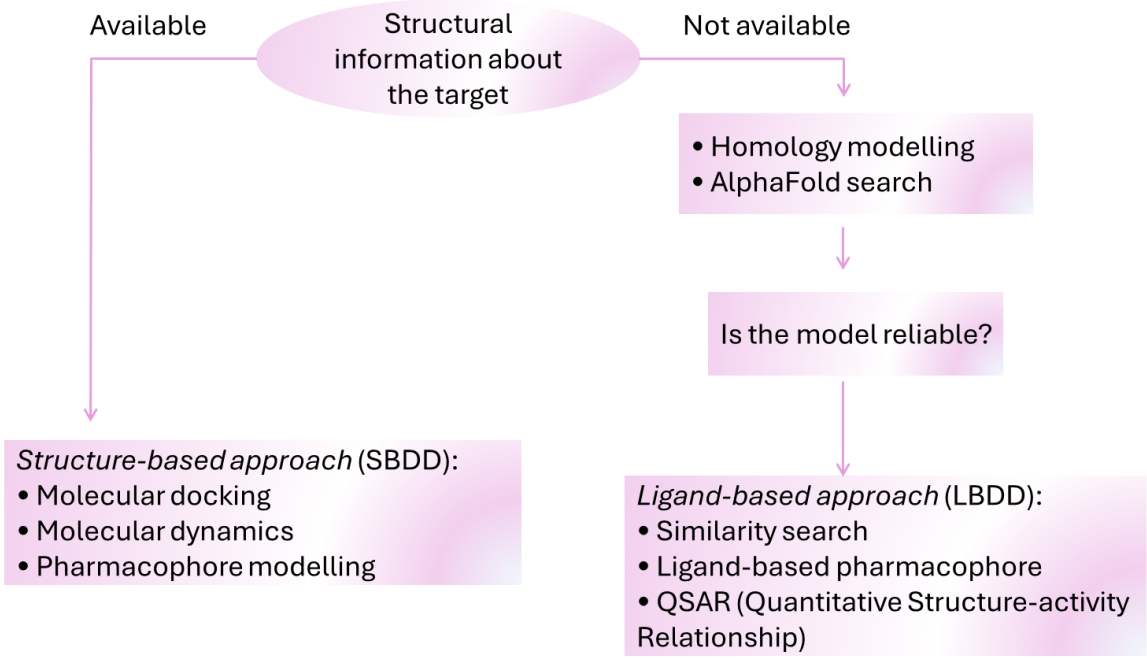

Figure 2: Schematic workflow of CADD approaches.

1.2.1 PHARMACOPHORE MODELLING

A pharmacophore model defines the spatial arrangement of the electronic and steric characteristics needed for a ligand to optimally interact with a biological target, ultimately determining the desired pharmacological response. These chemical features, such as hydrogen bond donors and acceptors, charged or ionizable groups, hydrophobic substituents, and aromatic systems, represent the interaction pattern necessary for molecular recognition at the active site. It should be noted that pharmacophore models can be developed through ligand-based or structure-based approaches, depending on the experimental information available.[7]

Ligand-based drug modelling represents a valuable approach in the absence of an experimentally determined three-dimensional structure of the biological target. In this case, a set of well-known active compounds is analyzed to identify the chemical features they share, assuming that these common elements are responsible for biological activity. Techniques such as QSAR help capture key physicochemical properties, facilitating the construction of predictive models that can be used for virtual screening to identify new leads with similar interaction characteristics. In contrast, structure-based drug design exploits the three-dimensional structure of the target protein, typically obtained from X-ray crystallography or cryo-electron microscopy, to characterise key interaction regions within the binding pocket. This strategy allows pharmacological characteristics to be extrapolated from a ligand in complex with the protein or, alternatively, from the binding cavity of the apo form, characterizing the residues and their interaction potential. Because it relies on precise molecular details of the target, this approach generally offers greater reliability and interpretability than ligand-only methods and can also be developed from a single co-crystallized ligand. A limitation may arise if too many features are initially detected, requiring careful refinement to maintain a balance between model accuracy and usability.[8,9]

1.2.2 MOLECULAR DOCKING

Molecular is among the most extensively applied methodologies in SBDD. It is a computational technique designed to predict both the binding affinity and optimal

position of a ligand within the target protein binding site. The process explores distinct ligand binding poses and conformational states within the binding cavity, and computational scoring functions are then employed to estimate the probability of the predicted interaction.[10]

Docking approaches for small molecules can be classified based on the degree of conformational flexibility considered for the ligand and receptor. In rigid docking, both the ligand and the protein are treated as rigid bodies, in line with the classic "lock-and-key" view of molecular recognition. Although computationally efficient, this method can lack accuracy when significant conformational adjustments occur upon binding. A more representative approach is provided by semi-flexible docking, in which the ligand can move around its internal bonds while the protein remains rigid. This approach more effectively captures the adaptability of the ligand within the active binding pocket while maintaining a relatively low computational cost.[11,12] Effective biomolecular recognition, however, involves mutual structural adaptation. To address this limitation, methods incorporating protein flexibility have been developed. Side-chain flexibility docking keeps the backbone structure of the protein fixed while allowing local rearrangement of selected side chains, particularly those close to the ligand or known to influence binding.[11, 13]

A more comprehensive approach is induced-fit docking, in which both the ligand and the protein can change their conformation during the simulation. This lets the system get to a more realistic, mutually adaptive binding mode. While it is really accurate, it is computationally intensive and therefore not typically employed for routine applications, especially when dealing with highly flexible binding pockets.[14] Another strategy is ensemble docking, in which multiple receptor conformational states, derived from X-ray structures or molecular dynamics simulations, are used to better capture the dynamic panorama of the protein. This method is particularly suitable when the target has several functional states and a high degree of flexibility.[15, 16]

Overall, with the progressive introduction of flexibility, from rigid docking to docking with flexible ligands and finally to completely flexible receptor-ligand docking, the biological relevance and predictive accuracy of docking results increase, albeit at a higher computational cost.[7]

1.2.3 MOLECULAR DYNAMICS SIMULATIONS

Molecular dynamics simulations are a powerful computational approach capable of modelling the evolution of biomolecular systems over time at atomic resolution. Through the numerical integration of Newton's equations of motion, molecular dynamics provides information on conformational transitions, ligand-protein recognition, protein folding, ion permeation, and other mechanistic processes that are not captured by static crystallographic structures.[1, 17]

In contrast to molecular docking, which typically uses a rigid or semi-flexible representation, molecular dynamics simulations allow for full flexibility of both the ligand and the receptor, thus more accurately approximating realistic biochemical environments. This dynamic sampling helps reveal structural intermediates and binding modes that may be crucial for molecular recognition. The main limitation of dynamics simulations is their computational cost, as the required sampling can extend simulation times from nanoseconds to microseconds and scale poorly with system size.[4, 6, 18]

A crucial element of classical molecular dynamics is the force field, a mathematical model that describes interatomic interactions through bonded (bond lengths, angles, dihedral angles) and unbonded (electrostatics and van der Waals) terms. Among the most commonly used biomolecular force fields are AMBER, CHARMM, GROMOS, and OPLS, each parameterized to balance speed and accuracy depending on the application. For example, the AMBER family of force fields is widely validated for proteins and nucleic acids, CHARMM has a robust lipid parameterization, and OPLS works well in a chemical space similar to that of small molecule drugs.[19-22] An appropriate choice of force field ensures reliable sampling and accurate reproduction of thermodynamic properties.

One of the main advantages of molecular dynamics simulations is that it is possible to generate sets of receptor conformations, overcoming the limitations of individual static protein structures derived from cryo-electron microscopy or X-ray crystallography. These conformations can be used for set docking or to study induced-fit effects, improving binding site accuracy and hit discovery rates. Furthermore, molecular dynamics can be integrated with free binding energy calculations such as MM-PBSA and MM-GBSA,

which evaluate the contributions of electrostatic, van der Waals, and solvation terms to improve ligand affinity prediction. Entropic corrections can be evaluated via normal mode analysis, further refining the thermodynamic profile.[1,23]

In conclusion, molecular dynamics simulations complement docking by offering greater biological fidelity at the cost of computational resources. Their ability to explore conformational space, validate binding modes, and refine energy predictions makes them an indispensable component of modern CADD workflows.

1.2.4 SOFTWARE USED DURING THIS RESEARCH

To support the computational investigations presented in this research project, a variety of specialized CADD tools were employed, each selected based on its relevance to the specific task. The complete list of software and their roles within the workflow is summarized in Table 1.

Table 1: Overview of Computational Tools employed during the PhD research.

Software	Application in this project
LigandScout	Pharmacophore modelling, Virtual screening
Schrödinger Suite	Alanine scanning, Ligand and Protein Preparation, MM-GBSA (Prime)
GOLD	Molecular docking
Desmond*	Molecular dynamics simulations
SwissADME; pkCSM	ADMET prediction
Maestro; PyMOL	Molecular visualization and graphical representation

*Desmond is integrated within the Schrödinger Suite.

LigandScout. LigandScout[24] is an advanced molecular modelling platform widely recognized for its applications in drug discovery. The software is based on the well-established concept of pharmacophores, which describe drug-receptor recognition through essential chemical features, such as hydrogen bond donors and acceptors, charged or ionizable groups, hydrophobic hot spots, and aromatic systems, arranged in a 3D spatial orientation that reflects optimal ligand-target interactions.[24] It automatically extracts and visually represents the interaction characteristics between small molecules and the residues of a given binding site, using six main types of chemical features combined with shape and volume constraints to generate precise pharmacological hypotheses that capture the essential elements of ligand-receptor recognition. (Figure 3)

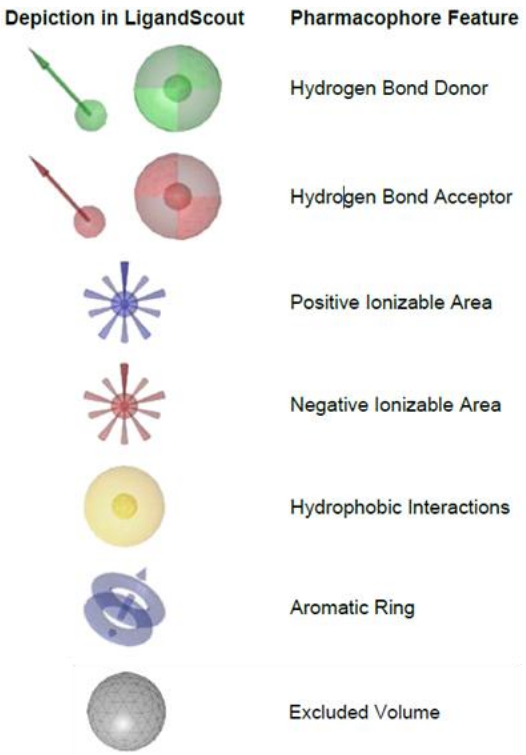

Figure 3: In LigandScout, pharmacophoric features are represented through intuitive 3D graphical elements: hydrogen bond donors and acceptors are visualized as arrows or spheres indicating interaction directionality; hydrophobic and aromatic features are depicted as spherical elements defining their spatial centroid and tolerance; charged interaction sites are indicated by star-shaped markers; and steric restrictions are conveyed via gray excluded-volume spheres that outline regions inaccessible to ligand atoms.

Pharmacophore models in LigandScout can be constructed using two complementary strategies: i) *structure-based*, analyzing interaction characteristics extracted directly from protein-ligand complexes using X-ray or NMR; or ii) *ligand-based*, identifying the maximum set of common chemical characteristics shared by multiple active ligands. One of the key advantages of this software is its integration of virtual screening based on pharmacophores, a computational method that efficiently explores large chemical libraries to prioritize molecules that best meet defined pharmacological constraints. Although *in silico* screening does not yet achieve the experimental success rates for false positives or false negatives, it far exceeds the productivity of traditional laboratories, thanks to the rapid processing of millions of compound conformations. To enable accurate shape recognition and electronic complementarity, LigandScout utilizes pre-generated multi-conformational databases, allowing for comprehensive conformational sampling without increasing screening times. This approach contributes to the suitability of the software for large-scale drug discovery applications.[25] (Figure 4)

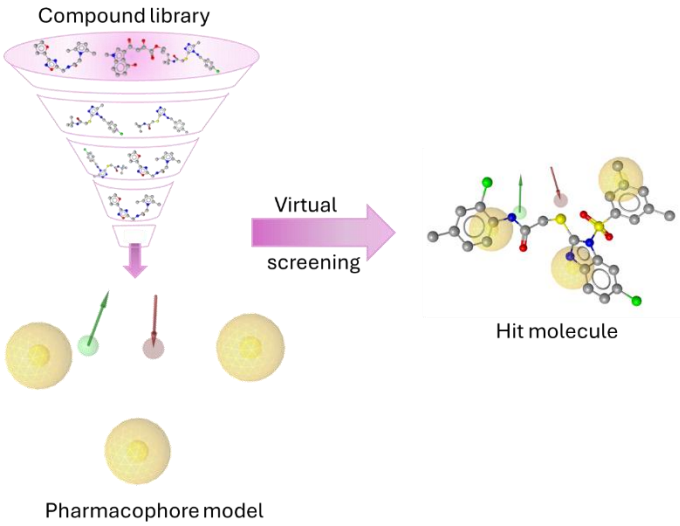

Figure 4: Virtual screening procedure using pharmacophore models.

Schrödinger Suite. The Schrödinger Suite[26] is an integrated computational platform that offers high-precision tools for molecular modelling, docking, and free energy calculations. Within this framework, *LigPrep* and *Protein Preparation Wizard* ensure

high-quality structural refinement by optimizing protonation states, correcting bond orders, assigning partial charges, and resolving steric or geometric inconsistencies prior to simulation or docking workflows.[11,27]

Alanine scanning mutagenesis from Schrödinger's BioLuminate module is useful for studying the specific contributions of residues to ligand recognition. This computational approach systematically replaces the side chains of selected amino acids with alanine and evaluates the corresponding change in free binding energy (ΔΔG). Since alanine maintains the geometry of the main chain while eliminating most side chain interactions, the method allows for the accurate determination of hot-spot residues, namely those that strongly stabilize ligand binding through hydrophobic contacts, hydrogen bonds, π-stacking, or electrostatic interactions.[28,29]

MM-GBSA estimates the free binding energy *(ΔG_{bind})* through the combination of molecular mechanics energies and implicit solvation models. This approach provides a more reliable post-docking classification of ligand poses while maintaining a significantly lower computational cost than molecular dynamics or free energy perturbation methods. MM-GBSA has become a widely adopted evaluation strategy in lead optimization efforts, providing acceptable accuracy for prioritizing results among tens to thousands of candidate ligands.[12,23,30] The ΔG_{bind} calculation takes into account the energy contributions of the complex, the free receptor, and the free ligand:

$$\Delta G_{bind} = \Delta G_{complex} - \Delta G_{free\ receptor} - \Delta G_{free\ ligand}$$

where each free energy term is approximated by the combination of the molecular mechanical energy and solvation effects. The generalized Born (GB) and solvent-accessible surface area (SASA) models are used to describe the polar and nonpolar solvation components, respectively, implemented through the VSGB solvation model to better represent the heterogeneous polarization within the protein.[30,31]

Desmond. Desmond, integrated into the Schrödinger Suite,[26] enables molecular dynamics simulations to be conducted to assess the stability and conformational behaviour of protein-ligand complexes under near-physiological conditions. Molecular

dynamics allows the study of dynamic interactions and induced adaptation effects that are not captured in static docking models, thereby improving the reliability of binding mode interpretation. Desmond is a highly optimized engine for explicit solvent simulations and is regularly incorporated into drug design workflows due to its computational efficiency and accuracy. Simulations are performed using the OPLS force field family, which was developed specifically to ensure realistic modelling of both protein flexibility and small molecule interactions, enabling better prediction of protein-ligand complex stabilization and secondary structure conservation.[22,30,32] In this research project, the OPLS4 and OPLS5 force fields were used, which represent the most advanced developments within the widely validated OPLS parameterization family. OPLS4 significantly expanded the coverage of chemical space and improved the accuracy of modelling noncovalent interactions, enabling more reliable predictions of protein-ligand binding thermodynamics. The most recent evolution, OPLS5, further refines the parameters for proteins, peptides, and small molecules, improving the stability of secondary structural elements, enhancing the description of charged and heterocyclic functionalities, and increasing compatibility with enhanced sampling molecular dynamics techniques.[22,33] Together, these tools provide a robust computational workflow for the accurate modelling, evaluation, and optimization of candidate inhibitors in drug discovery.

GOLD. Genetic Optimization for Ligand Docking (GOLD)[34,35] is a well-established structure-based molecular docking software used extensively to predict how small molecules bind within protein active sites. Its algorithm is based on a genetic algorithm (GA) that explores the conformational states and orientational space of the ligand by emulating evolutionary processes, including crossover, mutation, and selection, while maintaining the ligand flexibility and the receptor partial flexibility, particularly in the side chains. One of the key strengths of GOLD is the availability of multiple scoring functions, which evaluate the quality of each predicted pose by estimating the free binding energy and key molecular recognition features:

• *GoldScore*: energy scoring function combining hydrogen bonds, van der Waals forces, and ligand internal energy terms;

• *ChemScore*: evaluates metal coordination, lipophilic interactions, hydrogen bonds, and estimates free binding energy;

• *ASP* (Astex Scoring Potential): knowledge-based score derived from statistical analysis of protein-ligand complexes;

• *ChemPLP*: piecewise linear potential, optimized for high accuracy in pose prediction and commonly selected as the default setting in recent versions.

These complementary scoring functions enable flexible and robust classification strategies.[34-36]

SwissADME. SwissADME[37] is a freely accessible web platform designed to predict the main pharmacokinetic, physicochemical, and pharmacological similarity properties of small molecules. It evaluates descriptors such as lipophilicity (logP), water solubility, molecular flexibility, and polarity, and applies established medicinal chemistry rules, including Lipinski's, Veber's, and Ghose's filters, to assess oral bioavailability potential. SwissADME also integrates BOILED-Egg and P-gp substrate prediction models to estimate blood-brain barrier permeability and efflux susceptibility. These analyses support the early selection of compounds with favourable ADME profiles.[37-39]

pkCSM. pkCSM[40] is a predictive modelling tool that estimates the pharmacokinetics, toxicity, and safety endpoints of candidate compounds. It provides an *in silico* assessment of ADMET parameters such as hepatotoxicity, hERG inhibition, Ames mutagenicity, skin sensitization, and renal clearance mechanisms. These predictions facilitate the early identification of compounds with unfavourable safety profiles, minimizing experimental costs and improving compound prioritization.[40]

PyMOL. PyMOL[41] is a commonly used molecular visualization software for structural analysis and graphical representation of biomolecular systems. It enables high-quality rendering of protein-ligand complexes, facilitating inspection of key interactions at the binding site, such as hydrogen bonds, metal coordination, π-stacking, and hydrophobic contacts. PyMOL also supports structural overlay, surface analysis, and customizable scripting, enabling the generation of high-quality figures.[42,43]

Chapter 2

SKIN DISORDERS AND TARGETS OF INTEREST

2.1 GENERAL INTRODUCTION

The skin is a structurally and functionally complex organ that completely envelops the body surface, acting as the primary interface between the organism and the external environment. Its primary role is to provide a protective physical and biochemical barrier, preventing the loss of water and electrolytes, reducing the permeation of xenobiotic substances, and acting as protection against pathogenic microorganisms. Additionally, the skin plays essential roles in thermoregulation and provides immunologic surveillance.[44,45]

Anatomically, the skin is organized into three different layers such as the epidermis, the dermis, and the hypodermis, showing marked regional differences in the epidermal and dermal thickness, as well as in the distribution of epidermal appendages and in the melanocyte content.[46,47] Cutaneous changes related to chronological aging or photoaging, such as wrinkling, laxity, and pigmentary alterations, drive patients to seek cosmetic procedures to enhance the appearance of their skin.[44]

2.2 SKIN AGING, INFLAMMATION, AND PIGMENTATION DISORDERS

Various conditions may affect skin structure and function, particularly skin aging, pigmentation disorders, and inflammatory processes. These factors often interact, with overlapping mechanisms that contribute to the visible effects on the skin. Skin aging is a multifactorial, progressive process driven by both intrinsic and extrinsic factors.

Intrinsic (chronological) aging represents the natural physiological progression driven by genetically programmed biological changes.[48] It is characterized by progressive thinning of the epidermis, reduced elasticity, xerosis, fine wrinkling, and a decline in key dermal extracellular constituents such as elastin and collagen, largely due to reduced fibroblast number and metabolic activity. These alterations are compounded by reduced sebaceous gland density, diminished dermal vascularization, and loss of subcutaneous adipose tissue, contributing to skin atrophy, loss of elasticity, and increased fragility.[49] Despite these structural alterations, intrinsic aging generally produces moderate and

gradual aesthetic changes, principally fine wrinkles and dryness, whose severity depends on genetic background and individual physiology.[50]

In contrast, extrinsic (photoaging) aging is mainly driven by environmental insults, with chronic ultraviolet (UV) exposure accounting for up to 80% of total visible skin aging. UV radiation causes oxidative stress, DNA damage, and chronic inflammation, cumulating in deep wrinkles, loss of skin tone, spotty hyperpigmentation, and a rough texture.[48,51]

A notable feature of aged skin is also the remodelling of the dermal-epidermal junction, which results in decreased interfacial surface area between the epidermis and dermis, thereby compromising skin structure and function.[52] The phenomenon of inflammaging, defined as a state of chronic and low-grade inflammation associated with aging, further accelerates this cutaneous degeneration by sustaining a pro-inflammatory microenvironment rich in cytokines, chemokines, and growth factors. Inflammatory processes are crucial in the development not only of premature aging but also of skin tumorigenesis. Persistent inflammatory signalling activates pathways involved in DNA damage, oxidative stress, angiogenesis, and cellular proliferation.[53-55]

In addition to aging and inflammation, skin pigmentation disorders constitute another major class of dermatological conditions. Skin pigmentation is regulated by the combined influence of genetic, hormonal, and environmental factors. Genetic determinants govern the density and function of melanocytes, as well as the ratio of eumelanin to pheomelanin, which contribute to individual pigmentation patterns. Variations in melanosome size, number, and distribution also account for phenotypic differences across individuals and populations.[56]

UV exposure remains the predominant extrinsic stimulus for hyperpigmentation, stimulating melanogenesis through tyrosinase activation and ROS-mediated signalling, leading to melanin overproduction. Chronic UV exposure contributes to age spots, melasma, and post-inflammatory hyperpigmentation, often aggravated by hormonal fluctuations, such as pregnancy, oral contraceptives, or hormone replacement therapy. Conversely, hypopigmentation may result from genetic disorders, such as albinism, vitiligo, fungal or bacterial infections, trauma, or inflammatory dermatoses.[57]

Notably, pigmentation disorders are frequently linked to an inflammatory mechanism. For instance, acne-induced post-inflammatory hyperpigmentation is driven by ROS and cytokine release, which aberrantly stimulate abnormal melanocyte activity.

Additionally, hormonal dysregulation and various pharmacological agents, such as antibiotics, antimalarials, and tricyclic antidepressants, can modulate melanogenic pathways. Furthermore, with advancing age, the decline in melanocyte number, combined with functional hyperactivity of remaining melanocytes, leads to uneven pigmentation patterns typically observed in individuals over the age of 40.[55,58,59]

Collectively, aging, inflammation, and pigmentation disorders share convergent molecular mechanisms, most notably oxidative stress, chronic inflammation, and extracellular matrix remodelling. Elucidating these interconnected molecular processes is therefore critical for the formulation of targeted therapeutic strategies focused on retarding skin aging, limiting inflammation, and addressing pigmentation disorders.[60,61]

2.3 KEY MOLECULAR TARGETS IN CUTANEOUS PATHOPHYSIOLOGY

The pathophysiology of skin disorders is modulated by distinct molecular targets that regulate extracellular-matrix (ECM) homeostasis, pigment biosynthesis, inflammatory signalling, and neoplastic transformation. Among these, elastase and tyrosinase assume prominent roles and represent critical therapeutic targets.[62-65] The process of skin aging is strongly connected with ECM degradation, particularly the loss of elastic fiber integrity. Elastase is a serine protease that contributes significantly to the deterioration of essential ECM proteins, including elastin, collagen, and fibronectin.[62]

Elastin represents the core constituent of elastic fibers and imparts elasticity and resilience to skin, elastic ligaments, and cartilage, and it is therefore essential for their long-term functioning.[66] Their turnover in adult skin is extremely slow, rendering them particularly susceptible to cumulative damage. In aged and photoaged skin, elastic fiber networks are markedly altered, resulting in fragmentation and abnormal clumping, such as solar elastosis, as well as disrupted architecture.[66,67]

Dysregulated elastase activity is implicated in inflammatory skin disorders, including psoriasis, skin aging, and atopic dermatitis. Therefore, elastase inhibitors represent promising anti-aging and anti-inflammatory agents to preserve dermal structure and reduce photoaging-related damage.[62]

Tyrosinase is a copper-containing enzyme that is critically involved in the melanogenesis pathway. Hyperactivation of the tyrosinase enzyme is the underlying cause of hyperpigmentation disorders, including melasma, lentigines, and post-inflammatory hyperpigmentation. These conditions are also particularly related to UV exposure or hormonal stimuli. Different studies underscore tyrosinase as the primary molecular target in current hyperpigmentation management strategies.[68]

Inhibitors of tyrosinase are widely investigated as depigmenting agents to treat pigmentary disorders. Conversely, insufficient tyrosinase activity, as observed in albinism, results in hypopigmentation and impaired photoprotection. Targeting tyrosinase regulation thus represents a crucial therapeutic avenue in both hyperpigmentary and hypopigmentary conditions.[69-71]

In addition to elastase and tyrosinase, a network of other molecular mediators contributes significantly to skin pathology. Matrix metalloproteinases (MMPs), especially MMP-1, MMP-2, and MMP-9, are up-regulated in response to highly reactive oxygen species (ROS) and UV-induced signalling, promoting collagen degradation and ECM remodelling.[72] Pro-inflammatory cytokines, such as TNF-α, IL-6, IL-17, and IL-23, mediate chronic inflammation, contributing to both inflamm-aging and the pathogenesis of psoriasis and cutaneous neoplasms. Furthermore, transcriptional regulators like nuclear factor kappa-light-chain-enhancer of activated B cells (NF-κB) and mitogen-activated protein kinases (MAPKs) modulate the gene expression programmes underlying oxidative stress responses, inflammation, and ECM turnover.[73,74]

Taken together, the identification and strategic modulation of these molecular targets, such as elastase and tyrosinase, offer promising avenues for preventing and treating skin aging, inflammatory skin conditions, and pigmentary disorders.

2.3.1 ELASTASE: INVOLVEMENT IN SKIN AGING AND EXTRACELLULAR MATRIX DEGRADATION

Among the enzymatic mediators involved in ECM degradation, elastases, especially neutrophil elastase and fibroblast-derived elastase, play a pivotal role in the disruption of elastic fibers. Their activity contributes to reduced skin elasticity, increased laxity, and the development of wrinkles.[63] In detail, elastases constitute a subclass of serine proteases related to the chymotrypsin family and are primarily responsible for the degradation of the hydrophobic protein elastin, a key connective tissue protein responsible for tissue elasticity.[75] The progressive loss, fragmentation, or disorganization of the elastase enzyme is closely linked to the skin aging process, leading to decreased skin elasticity, wrinkle formation, and dermal thinning.[62,63,76,77]

Biochemical and molecular studies have identified three structurally related mammalian elastases, designated elastase 1, 2, and 3, as shown in Table 2. In humans, six elastase genes have been identified, encoding elastase 1, 2, 2A, 2B, 3A, and 3B.

Table 2: Classification of human elastase isoforms and their functions

Elastase Isoform And Gene name	Primary Tissue (Human)	Main Function	Notes
Elastase 1 (CELA1) (ELA1)	Keratinocytes	Epidermal homeostasis	The historical term 'pancreatic elastase 1' was incorrectly attributed to the human *CELA1* gene. Notably, *CELA1* is not present in the human pancreas, and the pancreatic elastolytic activity previously described as 'elastase 1' resulted from other pancreatic elastases (mainly CELA2 and CELA3 isoforms), not from CELA1.
Elastase 2 A/B (HNE) (ELANE; ELA2)	Neutrophils	Immunity, ECM degradation	HNE is a major mediator of ECM deterioration in the skin.
Elastase 3 A/B (CELA3A/B)	Pancreas	Digestion	These are the physiologically active human pancreatic elastases and the enzymes measured in clinical fecal elastase assays.

Human neutrophil elastase (HNE; EC 3.4.21.37, also known as elastase 2) is a neutrophil-derived protease traditionally recognized for its role in host defence. In addition to its antimicrobial and immunomodulatory functions, HNE is known to be a central mediator of ECM degradation within the skin. Importantly, several studies have clarified that the enzyme historically described as "pancreatic elastase 1" in humans does not originate from the ELA1 gene product: the authentic ELA1 locus is transcriptionally silent in the human pancreas due to mutations affecting enhancer and promoter regions. Consequently, the activity previously attributed to "elastase 1" reflects the action of other pancreatic elastases, such as CELA2-CELA3 isoforms. Thus, the enzyme relevant to ECM degradation and skin aging is HNE, whereas ELA1 does not contribute to these processes.[66,77-79]

HNE is localized within the azurophilic granules of neutrophils and plays a central role in the innate immune defence, antimicrobial activity, tissue remodelling, and inflammatory processes.[80] In addition, HNE has been shown to contribute directly to ECM damage in skin. In a hairless mouse model of repeated UVB exposure, increased neutrophil infiltration and elastase activity were observed, concomitant with enhanced activation of matrix metalloproteinases (MMP-1 and MMP-2) and significant connective tissue alteration. This supports a mechanistic link between elastase activity, inflammatory cell infiltration, and dermal ECM degradation in photoaged skin.[81,82]

Many reviews of elastases and related proteases, including neutrophil elastase, fibroblast elastase, and other elastin-degrading enzymes, emphasise their role in inflammaging, such as chronic low-grade inflammation associated with aging, and in ECM remodelling in various tissues, including the skin.[66,83]

Taking this into account, elastase represents a promising molecular target for combating skin aging and preserving the ECM. Strategies that inhibit elastase activity may slow dermal connective tissue degradation and preserve the structural integrity of the skin.[84-86]

Among the elastases expressed in human skin, HNE and CELA1 represent two biologically and anatomically distinct enzymes. HNE plays a predominant role in

inflammatory and immune contexts, while CELA1 seems to be more relevant to epidermal physiology. Their combined activities reflect the complexity of elastin regulation in the skin. During aging and photoaging processes, increased levels of inflammatory cytokines, ROS, and infiltrating neutrophils increase HNE activity, leading to elastin fiber degradation, fragmented elastotic material formation, and progressive weakening of the dermis. At the same time, CELA1 may contribute to alterations in the epidermal-dermal interface, although its precise role remains less characterized and represents an emerging field of investigation.[78,81]

Given the central role of HNE in the breakdown of the ECM, the fragmentation of elastin, and the weakening of the dermis during intrinsic aging and photoaging, the development of selective HNE inhibitors has emerged as a promising anti-aging strategy.[66,81]

HNE is a single-chain glycoprotein of -25 kDa and a primary sequence consisting of 218 amino acids. (Figure 5) The glycosylation occurs at the conserved N-linked glycan sites and plays a crucial role in modulating the enzyme's solubility, structural stability, as well as its interactions with endogenous inhibitors.[87] HNE is stabilized by four disulfide bonds, which are crucial for maintaining its correct folding and enzymatic activity. The first biochemical and structural investigations established these basic properties and confirmed the close relationship of HNE to other members of the chymotrypsin-like serine protease family.[87,88]

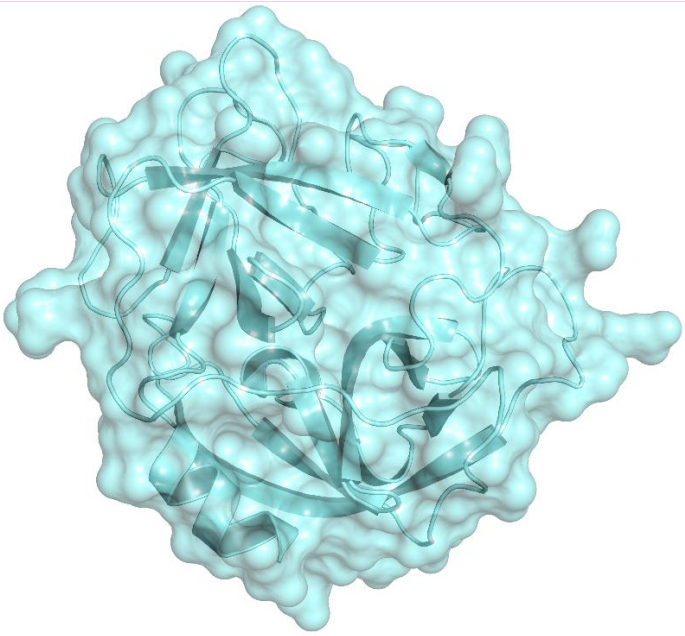

Figure 5: Structure of human neutrophil elastase (HNE – RSCB PDB: 3Q76).[89] The image is created using PyMOL.[90]

The binding site of HNE is located in a deep cleft between two β-barrel domains, and it is characterized by a catalytic triad that is formed of Asp102, His57, and Ser195, designated using chymotrypsin numbering (for clarity, Asp108, His60, and Ser203 using HNE renumbering). This designation is essential for structural and functional comparisons between elastase and related proteases. In addition to the catalytic triad, the binding site contains the oxyanion hole and several subsites.[91] Many studies conducted using oligopeptide substrates and mechanism-based inhibitors have shown the presence of at least six binding sites. In detail, four, namely S1, S2, S3, and S4, are located on the acyl side of the cleavage bond, while two sites, called S1' and S2', are located on the side of the leaving group (amide).[75,92] The S-subsites have been well characterised using non-competitive inhibitors that react with the protein to form an acyl-enzyme intermediate; however, the location of the S′ subsites on the leaving-group side of the catalytic triad remains poorly understood.[93]

Comparative sequence analysis has revealed that HNE shares approximately 40% sequence identity with porcine pancreatic elastase (PPE). (Figure 6)

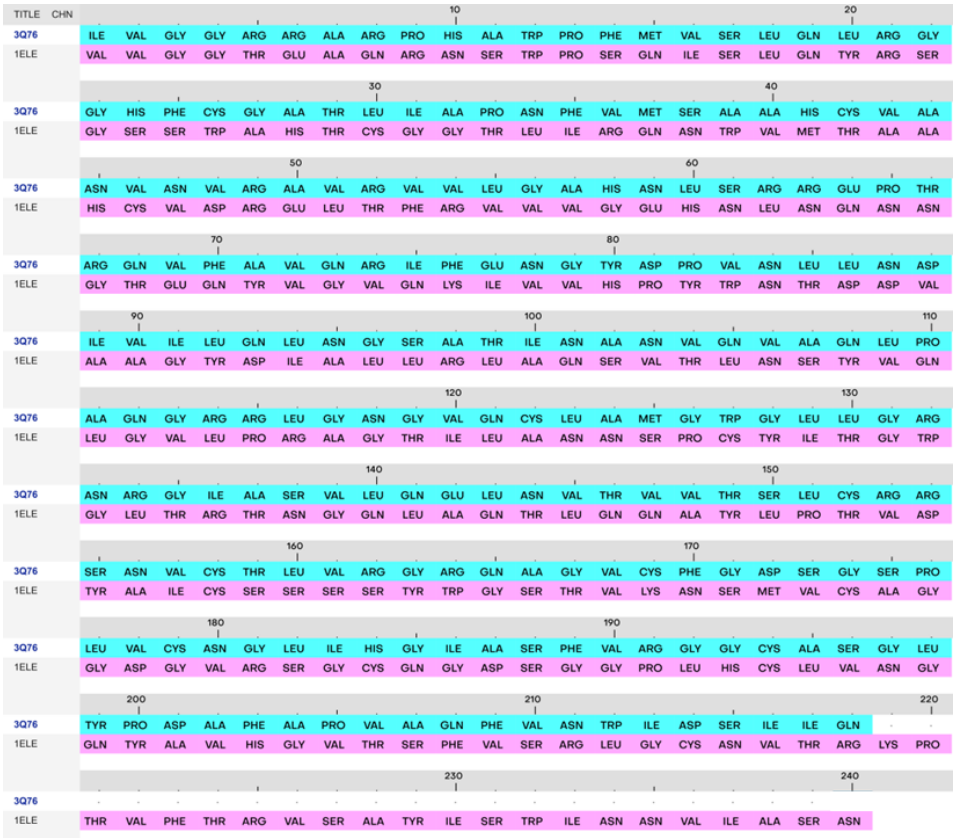

Figure 6: Sequence alignment of HNE (RCSB PDB: 3Q76)[89] and PPE (RCSB PDB: 1ELE)[94]. Residue numbering follows the chymotrypsin convention. The figure was generated using Maestro. [26]

Despite this moderate sequence homology, the two enzymes are very similar in the catalytic site area; in particular, their catalytic triad, Ser195, His57, and Asp102, and the principal residues of the binding site (189 to Ser195, 213-216, 226-228, residue 41) are conserved between HNE and PPE. (Figure 7) At the molecular level, PPE is a single polypeptide chain of 240 amino acids, starting at Val16 and ending at Asn245, also stabilized by four disulfide bridges.[75,88,95]

Based on this structural conservation of the active site, PPE is accepted as an excellent functional surrogate for HNE in enzymatic assays.[75] PPE offers experimental advantages, including high stability, low cost, easy purification, and broad commercial availability, in contrast with HNE, which requires isolation from human neutrophils or complex recombinant expression systems. For this purpose, PPE is routinely employed as a reliable model enzyme for the screening and mechanistic evaluation of elastase inhibitors.[75,96]

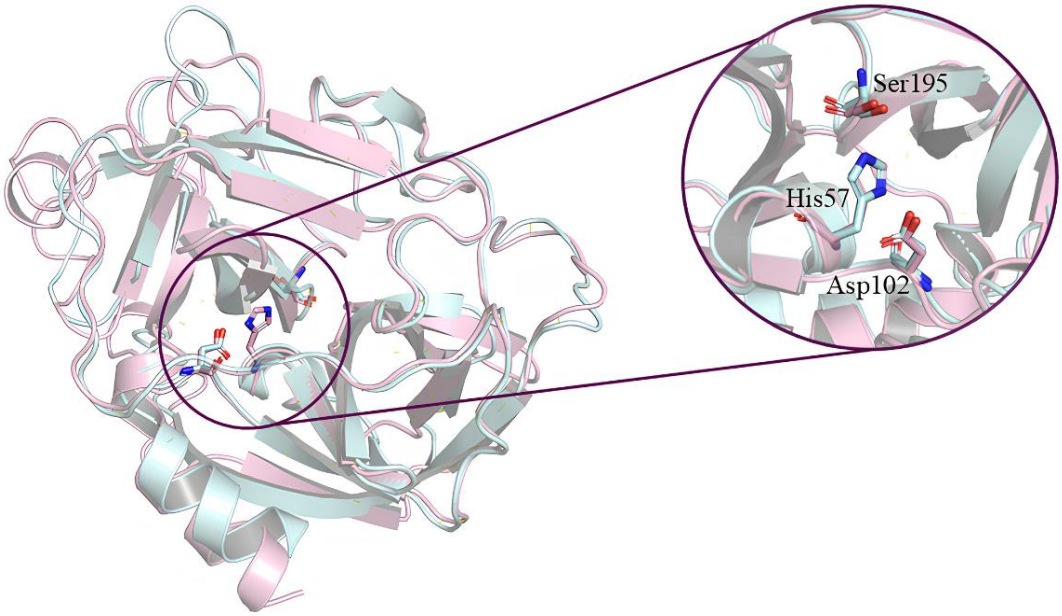

Figure 7: Superimposition of HNE (RSCB PDB: 3Q76)[89] and PPE (RSCB PDB: 1ELE)[94]. The HNE protein is represented as palecyan cartoon, and the PPE protein is shown as lightpink cartoon. The catalytic triad residues (Asp102, His57, and Ser195) are described as sticks with the corresponding colour for each enzyme. The figure was created with PyMOL[41].

The catalytic mechanism of elastases is characteristic of chymotrypsin-like serine proteases, and it proceeds through the nucleophilic attack of the catalytic Ser195 on the carbonyl carbon of the substrate, assisted by His57 and stabilized by Asp102. The generation of a tetrahedral intermediate is followed by its collapse into an acyl–enzyme complex. The leaving group is then released and subsequently hydrolyzed, regenerating the free enzyme. The oxyanion hole stabilizes the high-energy intermediates throughout this process.[91,97] (Figure 8)

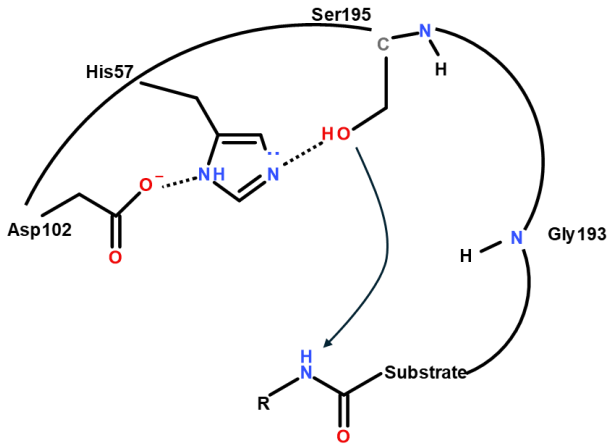

Figure 8:Catalytic mechanism of elastases, initiated by nucleophilic attack of the catalytic Ser195 on the carbonyl carbon of the substrate, supported by His57 and stabilized by Asp102. This mechanism involves the formation of a tetrahedral intermediate.

Elastase inhibitors exploit this catalytic machinery through several distinct mechanisms, which can be broadly classified into covalent irreversible inhibitors, covalent reversible (mechanism-based) inhibitors, and non-covalent inhibitors.[75]

Each class differs in its interaction modality with the active site. Reversible inhibitors typically act through the creation of a serine trap in which a peptide-type recognition element facilitates binding of the inhibitor within the active site, forming a reversible tetrahedral adduct. This class of inhibitors mimics the transition state of substrate hydrolysis. Within this group of inhibitors, carbonyl derivatives are of particular importance. In contrast, irreversible inhibitors act through a mechanism of action derived from the formation of a stable covalent bond with one of the residues of the catalytic triad. Within this class, phosphoryl fluoride derivatives represent a prominent class due to their high reactivity. Elastase inhibitors can also be classified according to their kinetic behaviour and binding site on the enzyme. Competitive inhibitors exhibit a structural similarity to the elastase enzyme substrate and compete for binding to the catalytic site. In contrast, non-competitive inhibitors bind to a distinct site from the active site and may induce structural alterations and toxic effects within the organism.[80,98]

2.3.2 TYROSINASE: ROLE IN MELANOGENESIS AND PIGMENTATION DISORDERS

Melanogenesis represents a complex multistep biochemical process responsible for the biosynthesis of melanin pigments, which are essential for skin, hair, and eye pigmentation and fundamental for photoprotection. This process takes place within specialized dendritic cells of neuroectodermal origin located in the basal layer of the epidermis, called melanocytes. In addition to the skin, melanocytes are also present in various extracutaneous tissues, including the uveal tract of the eye, the cochlea, the central and cardiovascular nervous systems, and adipose tissue.[64,65] In mammals, melanogenesis is regulated by a specific multienzyme complex that provides control of melanin biosynthesis. This pathway is modulated by multiple factors, such as genetic, epigenetic, and environmental factors, including DNA methylation, chromatin remodeling, and histone modifications, which together regulate melanocyte differentiation, enzyme expression, and melanosome maturation.[99,100]

At the biochemical level, melanogenesis begins with the conversion of L-tyrosine to L-3,4-dihydroxyphenylalanine (L-DOPA) through the monophenolase activity of tyrosinase enzyme, then the oxidation of L-DOPA to dopaquinone through its diphenolase activity. This reaction is considered the rate-limiting step in the melanin biosynthetic pathway.[68,101] Dopaquinone represents a highly reactive intermediate in the melanogenic process that leads to the synthesis of two chemically and functionally distinct types of melanin: eumelanin and pheomelanin. In the absence of thiol-containing compounds, dopaquinone proceeds through intramolecular cyclization followed by a series of oxidation steps to form eumelanin, an insoluble brown-black polymer. Conversely, in the presence of cysteine or glutathione, dopaquinone is diverted towards the development of pheomelanin, a soluble red-yellow polymer.[68,71,102] (Figure 9)

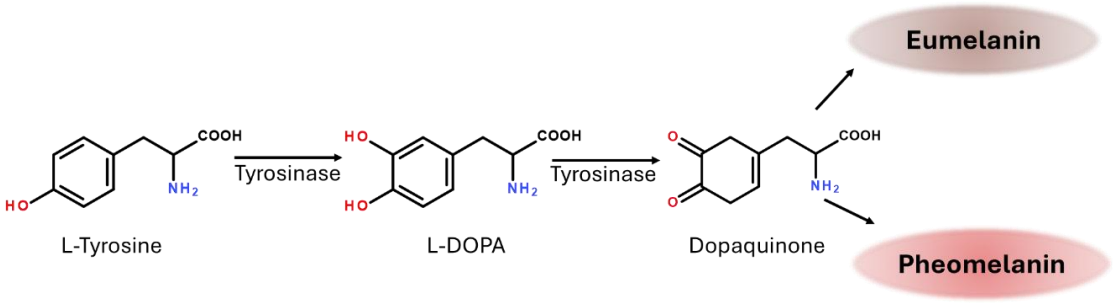

Figure 9: Schematic representation of the melanogenesis process.

In combination with tyrosinase enzyme, tyrosinase-related protein 1 (TYRP1) and tyrosinase-related protein 2 (TYRP2) are key components of the melanogenesis enzyme complex. These proteins contribute to the quality of melanin, polymer stabilization, and redox balance within melanosomes. In particular, L-tyrosine serves not only as the initial substrate for melanogenesis but also stimulates melanosome biogenesis and enhances tyrosinase activity, while L-DOPA acts as an autocrine and paracrine regulator that further amplifies melanogenic signaling. This regulatory cycle suggests that melanocytes actively control local and systemic melanogenic homeostasis by modulating the intracellular availability of L-tyrosine and the production of L-DOPA.[64,65]

Given its central role in the melanogenesis process, tyrosinase has been identified as a primary therapeutic target for the treatment of pigmentation disorders. Dysregulation of tyrosinase activity is associated with a large range of pigmentary disorders, including hypopigmentation disorders such as albinism and hyperpigmentation conditions such as melasma, freckles, neurodegenerative disease, risk of inflammation, and melanoma.[103] Consequently, numerous natural, semi-synthetic, and synthetic tyrosinase inhibitors, including kojic acid, arbutin, hydroquinone, azelaic acid, and novel polyphenolic derivatives, have been developed and studied for their ability to modulate melanin synthesis.[64,103,104] Targeting tyrosinase and its regulatory network remains a fundamental strategy in the management of pigmentation disorders and continues to be a focal point of research in cutaneous pharmacology and translational dermatology.

Human tyrosinase (hTYR) is a highly glycosylated transmembrane protein with a molecular weight of 67 kDa. It consists of 529 amino acids, of which 18 residues make up the N-terminal sequence of the protein, and seven residues are glycosylated.

Structurally, the enzyme has a structure that can be divided into four main regions: the N-terminal segment, the intramelanosomal domain, the transmembrane α-helix, and the cytoplasmic C-terminal domain. The transmembrane domain acts as an anchor for the entire protein structure, keeping the protein bound to the melanosomal membrane. The catalytic site, located in the intramelanosomal region, contains two copper ions, each coordinated by three histidine residues; specifically, the Cu_A ion is coordinated by residues His180, His202, and His211, while Cu_B is coordinated by His363, His367, and His390.[105,106]

hTYR is a transmembrane enzyme that presents considerable challenges in purification and crystallization procedures. As a result, the experimental three-dimensional structure of hTYR has not yet been determined, requiring the development of structural models using homology modelling techniques based on the similarity between hTYR and other proteins, namely TYRP1 and TYRP2. A representative model of the hTYR structure obtained through homology modelling is shown in Figure 10. This model was developed by the research group where I conducted my doctoral studies.[107]

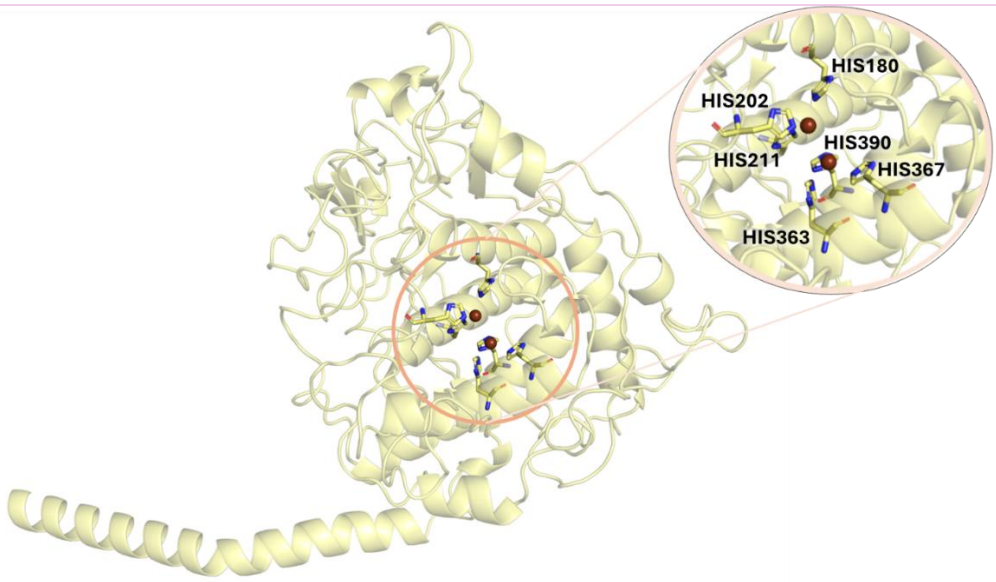

Figure 10: Structure of homology modelling of hTYR[107]. The protein is shown as paleyellow cartoon, while the six catalytic histidines are depicted as sticks of the same colour. The image was created using PyMOL.[41]

Among the different sources of tyrosinase, the mushroom tyrosinase from *Agaricus bisporus* (AbTYR) is an important and inexpensive source of tyrosinase with high similarity and homology to hTYR. AbTYR is a soluble tetrameric enzyme discovered in the cytoplasm. Although comparative sequence analysis revealed 22-24% sequence identity with mammalian tyrosinase, AbTYR and hTYR show similar composition in catalytic sites.[104,108,109]

AbTYR is a tetramer of approximately 130 kDa, formed by two H subunits, which have a higher molecular weight (43 kDa), and two L subunits, which have a lower molecular weight (13 kDa).[110,111] The H_2L_2 tetramer is stabilized by a set of interactions between the amino acids of the two different subunits. The H subunit consists of 392 residues and has a high degree of homology with TYRs found in other species. Within the H subunit is the catalytic site, located between a pair of antiparallel α-helices. The site contains two copper ions, called Cu_A and Cu_B, each coordinated by three histidine residues. Specifically, the Cu_A ion is coordinated by residues His61, His85, and His94, while Cu_B is coordinated by amino acids His259, His263, and His296. The L subunit consists of 150 amino acids and is formed by 12 antiparallel β-strands. The physiological role of the L subunit has not yet been identified.[112] Figure 11 shows a 3D representation of the structure of the AbTYR enzyme.

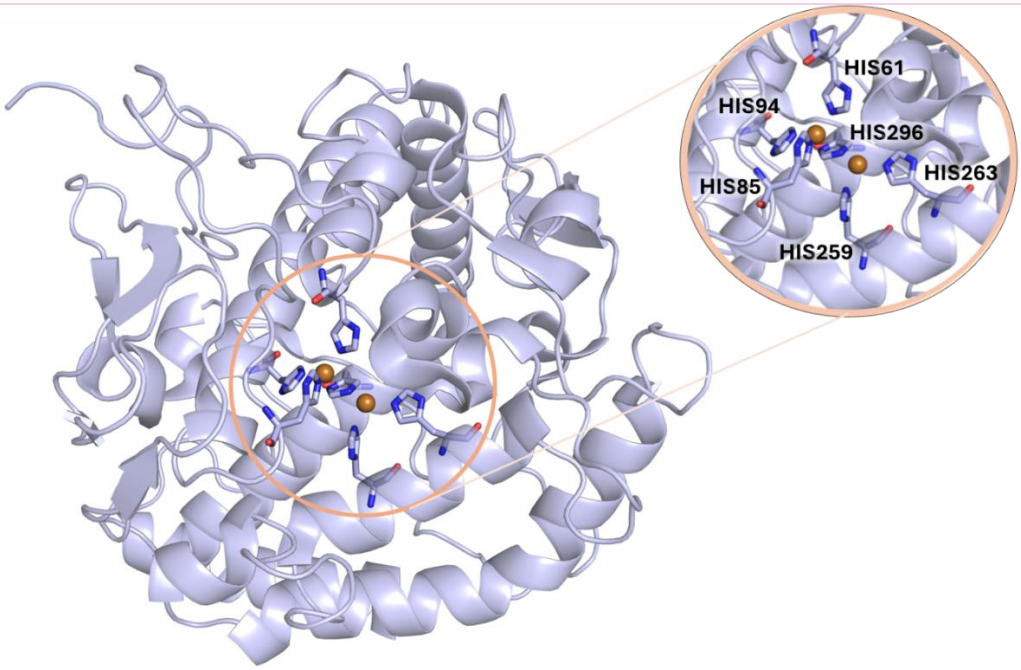

Figure 11: 3D representation of the AbTYR structure (RCSB PDB: 2Y9X).[112] The protein is shown as lightblue cartoon, while the six catalytic histidines are depicted as sticks of the same colour. Copper ions are shown as brown spheres. The image was created using PyMOL.[41]

2.4 CURRENT THERAPEUTIC APPROACHES FOR ELASTASE AND LIMITATIONS

Over the past decade, numerous small-molecule inhibitors, peptides, and natural compounds with anti-elastase activity have been identified. These include serine protease inhibitors, as well as plant-derived polyphenols and marine or fungal metabolites that exhibit selective inhibition of elastase.[97] Sivelestat (ONO-5046, Elaspol® 100) is a non-peptide HNE inhibitor (IC_{50} = 44 nM and Ki = 200 nM) approved in Japan and South Korea for intravenous treatment of ALI (Acute Lung Injury) and ARDS (Acute Respiratory Distress Syndrome) associated with systemic inflammatory response syndrome.[113] Other HNE inhibitors are Alvelestat (AZD9668), Freselestat (ONO-6818), which are extensively investigated in inflammatory and pulmonary indications.[76,114]

Although many natural HNE inhibitors have been identified, [115-117] they lack sufficient potency, selectivity, and metabolic stability for drug development. However, Lyngbyastatin 7 represents an exception: this 19-membered cyclic hexapeptide, isolated from marine cyanobacteria by Salvador et al. in 2013 and subsequently obtained by total

synthesis, exhibits potent HNE inhibition (IC_{50} = 23 nM) and remarkable selectivity against a panel of 68 proteases.[97,118,119] (Table 3)

Table 3: 2D structure of elastase inhibitors, Sivelestat, Alvelestat, Freselestat, and Lyngbyastatin 7. The structures were generated using Biovia Draw.[120]

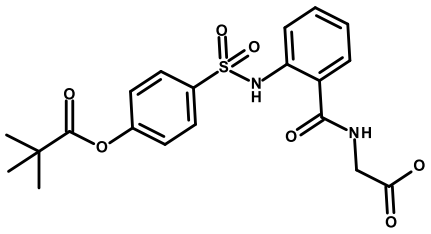	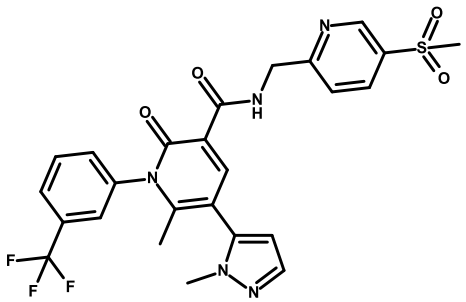
Sivelestat	**Alvelestat**
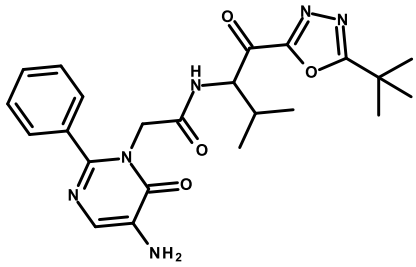	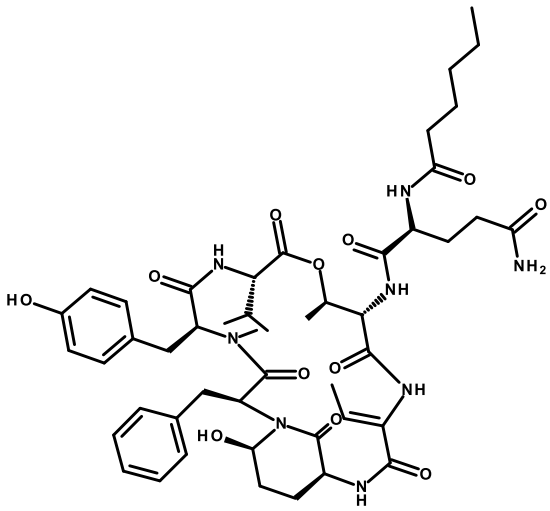
Freselestat	**Lyngbyastatin** 7

In preclinical models, selective inhibition of fibroblast elastase has been shown to prevent UVB-induced wrinkle formation in a dose-dependent manner, demonstrating a direct correlation between reduced elastase activity and improved dermal elasticity.[121] Similarly, topical formulations containing elastase-inhibiting peptides or polyphenolic antioxidants, including epigallocatechin gallate, resveratrol, or procyanidins, have been evaluated for their synergistic effects in maintaining ECM integrity and preventing solar elastosis.[77]

Despite these promising results, there are several limitations that hinder the translation of elastase inhibitors from experimental research to clinical dermatology. First, achieving

selectivity and specificity remains a challenge: elastases share a high structural homology with other serine proteases, which complicates the design of inhibitors that can selectively target HNE without affecting other essential proteolytic enzymes involved in normal tissue remodelling and immune defense.[66] Moreover, most HNE inhibitors were originally developed for systemic inflammatory or pulmonary conditions, with few optimized for cutaneous application.[97]

A second major limitation is related to skin delivery and bioavailability. Elastase activity is primarily localized in the dermal compartment; however, topical formulations must first traverse the epidermal barrier, which limits drug penetration and efficacy. Current research, therefore, focuses on advanced delivery systems, such as liposomes, nanoemulsions, and polymeric nanoparticles, to improve dermal bioavailability. However, despite significant technological progress, clinical validation of these systems remains poor.[122]

Finally, it is important to emphasize that skin aging is a multifactorial process. Consequently, monotherapies exclusively targeting elastase may be insufficient. There is an emerging consensus in support of multimodal therapeutic approaches that combine elastase inhibition with antioxidants, anti-inflammatory agents, and MMP modulators to preserve dermal architecture more effectively and counteract the biochemical cascades of photoaging.[66,77]

In summary, although elastase inhibition offers a promising therapeutic target for maintaining skin elasticity and delaying visible ageing, the current strategies face significant pharmacological and translational challenges. The next generation of elastase-directed therapies will likely require highly specific inhibitors, optimized topical delivery systems, and clinical evidence demonstrating both efficacy and long-term safety.

2.5 CURRENT THERAPEUTIC APPROACHES FOR TYROSINASE

Synthetic pharmacological agents have long been used in the treatment of hyperpigmentation disorders due to their ability to inhibit melanin synthesis and promote skin lightening. Conventional depigmenting agents, including hydroquinone,

corticosteroids, retinoids, and azelaic acid, mainly act by suppressing tyrosinase activity, interfering with melanosome maturation, or accelerating epidermal turnover. Despite their clinical efficacy, the long-term use of these compounds is often limited by adverse effects such as cytotoxicity, skin irritation, ochronosis, rebound hyperpigmentation, and regulatory restrictions, leading to the search for safer and more sustainable alternatives.[123]

Hydroquinone has historically been considered the best depigmenting agent due to its potent inhibitory effect on tyrosinase activity. Its mechanism of action is multiple: it involves not only the competitive inhibition of TYR but also the degradation of melanosomes and the induction of melanocyte necrosis. While these effects underlie its strong depigmenting efficacy, they are also responsible for significant cytotoxicity and genotoxicity problems, which have led to its withdrawal or strict regulation in many states. Structural glycosylation of hydroquinone produces arbutin, a naturally occurring plant-based β-D-glucopyranoside.

Unlike hydroquinone, arbutin reduces melanin synthesis without inducing melanocyte damage. Its depigmenting activity is mediated by multiple mechanisms, including downregulation of TYR expression, inhibition of post-translational modifications and tyrosinase maturation, irreversible inactivation of mature TYR, and its function as an alternative TYR substrate leading to enzymatic inactivation.[124,125]

Among synthetic and semisynthetic inhibitors, kojic acid represents one of the most widely studied tyrosinase inhibitors and is often used as a positive control in research on tyrosinase-mediated hyperpigmentation.[70] Kojic acid and its derivatives inhibit melanogenesis primarily through chelation of copper ions present in the active site of TYR, thereby preventing enzyme activation and subsequent oxidation of L-tyrosine and L-DOPA.[126]

Tropolone exhibits exceptionally high tyrosinase inhibitory activity described to date. Structurally analogous to the o-diphenol substrates of TYR, tropolone acts as a strong copper chelating agent and exhibits a slow-binding inhibition profile, characterized by the gradual formation of a stable enzyme–inhibitor complex. This kinetic behaviour increases its inhibitory efficacy but also raises concerns regarding selectivity and potential toxicity. Compounds with similar inhibitory mechanisms include 4-substituted

resorcinols, which have been extensively studied for their high affinity for the tyrosinase active site.[112,127]

Resorcinol derivatives currently represent the most clinically relevant class of tyrosinase inhibitors. Among these, 4-butylresorcinol, also known as Thiamidol™, has emerged as a reference compound in the global depigmenting agent market.

Thiamidol™ demonstrates high selectivity for human tyrosinase, superior inhibitory potency compared to classical agents, and a favourable safety profile, making it particularly suitable for long-term topical use. Its efficacy has been validated in multiple clinical studies targeting melasma, post-inflammatory hyperpigmentation, and solar lentigines.[128-130] (Table 4)

Table 4: 2D structure of tyrosinase inhibitors. The structures were created with Biovia Draw.[120]

	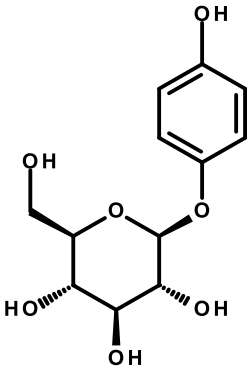	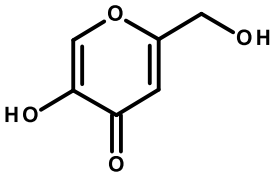
Hydroquinone	Arbutin	Kojic acid
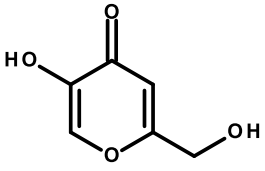	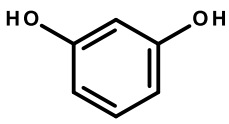	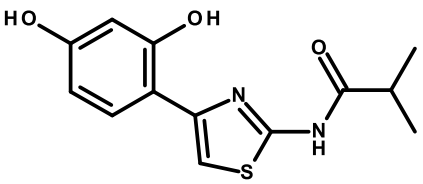
Tropolone	Resorcinol	Thiamidol™

In recent years, natural products have attracted increasing attention as alternative tyrosinase inhibitors due to their structural diversity, multitarget activity, and improved tolerability profiles. Numerous plant-derived polyphenols, flavonoids, phenolic acids, and alkaloids have demonstrated significant anti-tyrosinase activity through copper

chelation, competitive or mixed-mode inhibition, antioxidant effects, and modulation of melanogenic signalling pathways.[104,131,132]

In conclusion, although conventional depigmenting agents remain effective, their safety limitations underscore the necessity of innovative tyrosinase-targeted strategies with increased selectivity and reduced toxicity.

2.6 COSMECEUTICAL ACTIVES AND DERMOCOSMETIC PREPARATION FOR ANTI-AGING AND DEPIGMENTING THERAPIES

The concept of cosmeceuticals has emerged as a critical bridge between cosmetic science and pharmaceutical dermatology, describing topical formulations that combine aesthetic enhancement with biologically active therapeutic functions. Although Albert Kligman first coined the term in the 1980s, it still lacks formal recognition by regulatory agencies such as the U.S. Food and Drug Administration (FDA) and the European Medicines Agency (EMA), which continue to categorize topical formulations strictly as either cosmetics or drugs. Consequently, cosmeceuticals occupy a regulatory "grey zone," lacking standardized requirements for both safety and efficacy assessments.[133] Since regulatory agencies do not impose formal criteria for demonstrating efficacy, most high-quality cosmeceuticals are formulated using ingredients with established safety records, and their efficacy is generally evaluated through non-pharmacological clinical studies, typically supervised by dermatological research centers. These studies often evaluate the efficacy of the final formulation.[133,134] Modern formulations increasingly incorporate bioactive peptides, botanical polyphenols, liposomal carriers, enzymatic antioxidants, and biomimetic molecules capable of modulating pathways involved in skin aging, hyperpigmentation, ECM degradation, and oxidative stress. These compounds target key processes, such as collagen breakdown, elastase activity, melanogenesis, inflammation, and mitochondrial dysfunction, reinforcing the scientific foundation of cosmeceutical interventions.[135,136]

Despite these advances, significant limitations remain, particularly regarding standardization, reproducibility, and clinical validation. Many marketed products rely on *in vitro,* or *ex vivo* data without robust human trials, and their regulatory ambiguity complicates safety assessment and claim substantiation.[137]

A growing number of dermocosmetic preparations available in pharmacies integrate multiple active ingredients to address complex cutaneous conditions. For instance, anti-aging formulations commonly combine hyaluronic acid, peptides, retinoids, antioxidants, and polyphenols to counteract wrinkles, loss of elasticity, and dermal thinning. Products targeting hyperpigmentation frequently include tyrosinase inhibitors such as niacinamide, azelaic acid, Thiamidol™, resorcinol derivatives, or vitamin C, often supported by exfoliating agents or soothing botanical extracts.[129,136,138] Representative examples of such commercially available dermocosmetic formulations are offered by established brands, including Eucerin, Bionike, MIAMO, La Roche Posay, Apivita, Filorga, among others.

The dermocosmetics formulations adopt a multifactorial approach to address the complex pathophysiology of skin aging and hyperpigmentation. Clinical and preclinical evidence support the efficacy of several widely used formulations, particularly those containing Thiamidol™, niacinamide, or retinol, which demonstrate measurable improvements in skin texture, elasticity, and skin pigmentation irregularities. Despite these advances, most dermocosmetic treatments are only effective at a preventive or supportive level. This means that optimal results are typically achieved when such products are integrated into long-term treatments.[129,136,139,140]

In summary, dermocosmetics targeting skin aging and hyperpigmentation have become essential tools in both clinical and esthetic dermatology.

2.7 AIMS AND SCOPE OF THE THESIS

Building on the data reported in the previous chapter, the main purpose of this doctoral research is to explore the discovery and optimization of novel small molecules with

potential applications in the prevention and treatment of skin aging and pigmentation disorders.

The central goal of this work is to use *in silico* drug design methodologies, including rational design, virtual screening, and molecular modelling, to identify promising candidate compounds and clarify the key structural determinants governing enzyme–inhibitor interactions. The use of computational tools allows the quick selection of molecules with favourable interaction profiles and predicted biological activity before experimental testing.

The research is structured around two interrelated case studies.

The first focus is on designing and optimising elastase inhibitors using synthetic compounds as model systems for virtual screening and structure–activity relationship analyses. These compounds were also employed to refine and validate the computational workflow prior to extending the same strategy to natural molecules that are more expensive and difficult to obtain. This procedure allowed for a more extensive exploration of structural diversity and facilitated the identification of innovative bioactive candidates with potential inhibitory activity. All derivatives underwent *in vitro* enzymatic testing to validate their predicted activity and evaluate their inhibitory potential experimentally.

The second case study applies a comparable computational workflow to identify tyrosinase inhibitors with the aim of discovering novel chemical scaffolds capable of modulating melanogenesis. In this project, we have the possibility to determine biological activity against two distinct tyrosinase forms, mushroom and human, and to evaluate compounds in cellular models.

In both cases, the combined *in silico-in vitro* strategy allows for greater accuracy of computational results and provides a basis for future structure-based optimization.

At the same time, the training period at Farmacia Marra srl. provided valuable information on currently available commercial formulations and consumer demand. This experience made it possible to evaluate existing products, assess patient needs and expectations, thus helping to define more relevant and practice-oriented research objectives.

Overall, this thesis aims to contribute to the rational development of selective and efficient enzyme inhibitors relevant to dermatological research, while demonstrating the effectiveness of computational methodologies as guiding tools in the early stages of drug discovery.

Chapter 3

CASE STUDY I – ELASTASE

3.1 COMPUTATIONAL APPROACH TO IDENTIFYING NEW CHEMICAL ENTITIES AS ELASTASE INHIBITORS WITH POTENTIAL ANTIAGING EFFECTS

The results described in this section have been the object of:

- **Publication:**
  - **Pitasi G**, Brancale A, Floris S, Fais A, Gitto R, De Luca L. Computational Approach to Identifying New Chemical Entities as Elastase Inhibitors with Potential Antiaging Effects. *Int J Mol Sci.* **2024** Oct 17;25(20):11174. doi: 10.3390/ijms252011174.

- **Poster Communications**:
  - **Pitasi G**, Brancale A, Floris S, Fais A, Gitto R, De Luca L. SCISiCa2024-Società Chimica Italiana Congresso Congiunto delle Sezioni Sicilia e Calabria 2024: "*Pharmacophore-based virtual screening for the identification of a new elastase inhibitor for anti-ageing purposes"* Aula Magna "Vittorio Ricevuto" del Polo Papardo, Università degli Studi di Messina, Italy; 2 - 3 December 2024
  - **Pitasi G,** Brancale A, De Luca L**.** XXVIII Congresso Nazionale della Società Chimica Italiana**:** "*Identification of novel potential elastase inhibitors with anti-aging activity using computational alanine scanning and pharmacophore modelling;* Alliaz MiCo Congress Center-Milano, Italy; 26 - 30 August 2024
  - **Pitasi G,** Brancale A, De Luca L**.** MedChem 2024-XIII Meeting of the Paul Ehrlich Euro-PhD Network: "*Structure-based pharmacophore modelling, computational alanine scanning, virtual screening, and simulation studies for the identification of potential elastase inhibitors with anti-aging activity*"; Università La Sapienza-Roma, Italy; 17 – 19 June 2024
  - **Pitasi G,** Brancale A, De Luca L**.** European Workshop in Drug Design (EWDD24): "*Computational alanine scanning and pharmacophore modelling to identify new potential elastase inhibitors with antiaging activity*"; Certosa di Pontignano-Siena, Italy; 19 - 23 May 2024

The skin elasticity and structural integrity are primarily determined by the dermal extracellular matrix (ECM), a complex network rich in collagens, elastic fibers, glycoproteins, proteoglycans, and glycosaminoglycans. Within the dermis, fibroblasts play a central role in producing and maintaining these components. Among them, collagen and elastin (ELN) are key structural proteins responsible for skin firmness and elasticity.

Elastase catalyzes the degradation of elastin; consequently, inhibiting elastase activity has emerged as a promising therapeutic strategy to slow down skin aging, preserve dermal architecture, and prevent wrinkle formation. Over the years, numerous elastase inhibitors have been developed, ranging from peptide-based structures mimicking natural substrates to non-peptidic small molecules with improved stability and pharmacokinetic properties. Several synthetic inhibitors, such as sivelestat, alvelestat, and GW311616A, have been investigated or approved for inflammatory and pulmonary diseases, while a variety of natural phenolic compounds have also demonstrated anti-elastase activity, as described in paragraph 2.4.

Given the advantages of small molecules, including better physicochemical properties and easier structural optimization, this work focuses on the computational identification of novel non-peptidic elastase inhibitors with potential dermatological applications. A multistep virtual screening approach was employed to develop an optimized pharmacophore model, which was then applied to an in-house library of synthetic compounds. The most promising candidates were subsequently selected and tested against protein porcine pancreatic elastase (PPE) as a preliminary assay to discover new leads capable of preventing elastin degradation, maintaining skin elasticity, and delaying visible signs of aging.

3.1.1 RESULTS AND DISCUSSION

To develop a pharmacophore model aimed at identifying novel potential inhibitors of PPE, five enzyme–inhibitor complexes were selected from the Protein Data Bank (RCSB PDBs: 1BMA,[141] 1BTU,[142] 1ELE,[94] 1HV7,[143] and 1JIM,[144] The selection was based on crystallographic quality criteria (R factor less than 0.2 and resolution less than 2.5 Å), the structural diversity of the linked inhibitors, and their ability to bind within the enzyme's active site. This approach provided coverage of a large range of key molecular interactions essential for molecular recognition. The chemical structures of the selected inhibitors are reported in Figure 12.

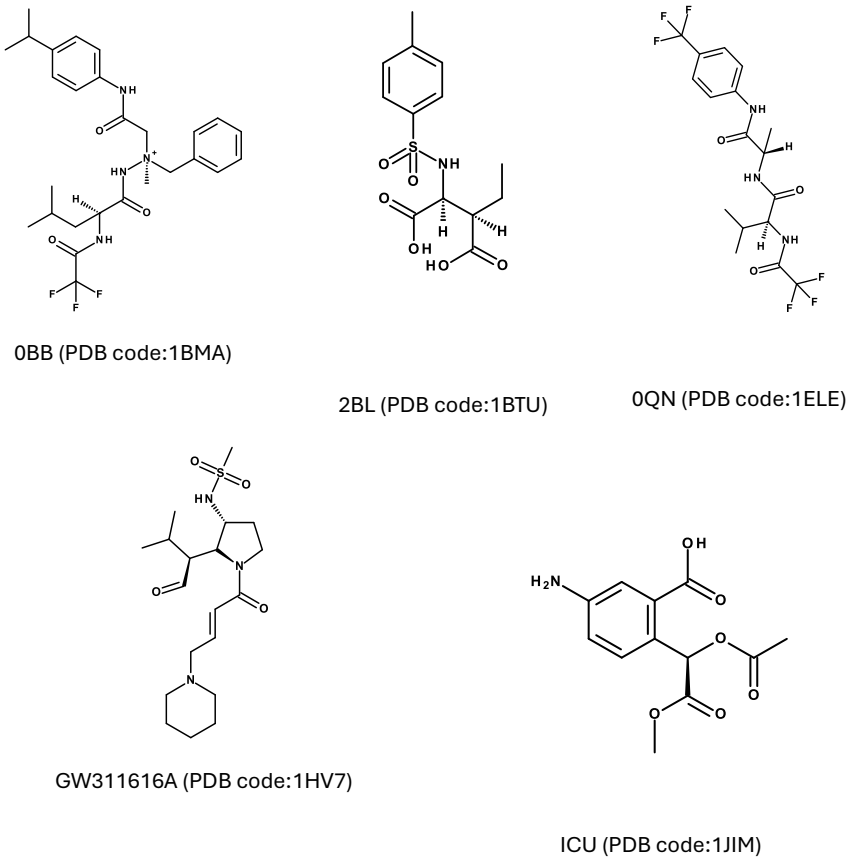

Figure 12: Two-dimensional representations of the five ligands bound to PPE in the selected Protein Data Bank complexes (RCSB PDBs: 1BMA,[141] 1BTU,[142] 1ELE,[94] 1HV7,[143] and 1JIM,[144] The structures were generated with BIOVIA Draw.[120]

These five distinct protein–ligand complexes were employed to create a structure-based pharmacophore model using LigandScout v2021.[24] For each complex, an individual pharmacophore model was developed, highlighting the key chemical features responsible for molecular recognition and interaction with specific amino acid residues within the catalytic site. The five resulting pharmacophores reflect fine variations in binding modes and interaction networks. A detailed description of each model is provided below. (Figure 13)

The model obtained from PDB entry 1BMA (Figure 13 A), which contains an aminimide-based peptidomimetic inhibitor (OBB), highlights five hydrophobic features (yellow spheres, H_1–H_5) associated with interactions with residues Val103, Thr221, Val224, Thr236, Thr152, Ala104, Thr182, and Phe223. In addition to these hydrophobic contacts, the backbone of Val224 contributes both a hydrogen bond acceptor (red arrow,

A_1) and a hydrogen bond donor (green arrow, D_1), emphasizing the role of backbone interactions responsible for stabilizing the ligand within the active site.

The pharmacophore extracted from 1BTU, shown in Figure 13 B, corresponds to the complex with the (3R)-3-ethyl-N-[(4-methylphenyl)sulfonyl]-L-aspartic acid (2BL). This model reflects the acyl–enzyme intermediate formed between the PPE protein and the ligand. Three hydrophobic features are observed (H_1, H_2, and H_6), mediated by residues Val103, Ile144, Thr221, Val224, Thr236, Trp98, and Thr100. Additionally, the model includes three hydrogen bond acceptors related to Gln200 (A_2), Gly201 (A_3), and Val224 (A_1), a hydrogen bond donor involving Ser222 (D_2), and one aromatic hydrophobic feature contributed by His60 (Ar_1).

Figure 13 C shows the pharmacophore derived from 1ELE, where Val103 again defines a hydrophobic feature (H_1). Additional hydrophobic features (H_2, H_4, and H_5) derive from interactions with Thr221, Val224, Thr236, Phe223, Ala104, and Thr182. This model presents a hydrogen bond acceptor with Val224 (A_1) and hydrogen bond donor features with Ser222 (D_2) and Val224 (D_1).

The pharmacophore of 1HV7, depicted in Figure 13 D, represents the complex with the trans-lactam inhibitor GW311616A in the opened form. In this case, one hydrophobic feature (H_2) is associated with Thr221, Val224, and Thr236, while three hydrogen bond acceptors arise from Gly201 (A_3), Ser203 (A_4) and Val224 (A_1).

Finally, the last model from 1JIM (Figure 13 E) for the ligand methyl(2-acetoxy-2-(2-carboxy-4-amino-phenyl))acetate (ICU) is simpler, consisting of two hydrogen bond acceptor features contributed by Gly201 (A_3) and Val224 (A_1). Although less complex, these features likely represent the key polar interactions necessary for ligand recognition.

All the different pharmacophore models were characterized by various excluded volumes that represented potential restrictions; in these areas, the ligand could not be localized.

Together, these five pharmacophore models provide complementary insights into the structural determinants of ligand binding, revealing how hydrophobic, polar, and aromatic interactions collectively define the specificity and affinity of inhibitors within the target binding site.

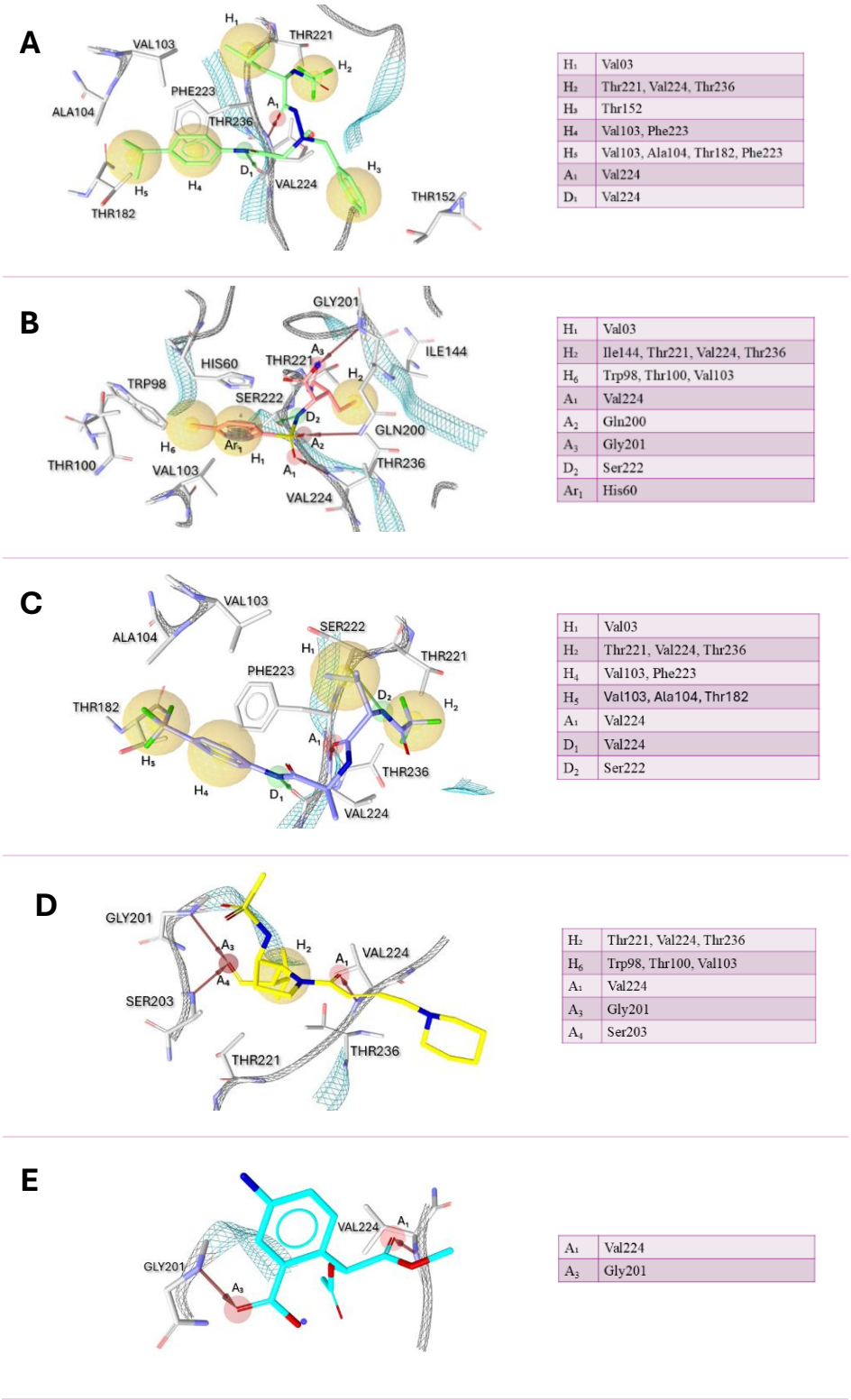

A	
H_1	Val03
H_2	Thr221, Val224, Thr236
H_3	Thr152
H_4	Val103, Phe223
H_5	Val103, Ala104, Thr182, Phe223
A_1	Val224
D_1	Val224

B	
H_1	Val03
H_2	Ile144, Thr221, Val224, Thr236
H_6	Trp98, Thr100, Val103
A_1	Val224
A_2	Gln200
A_3	Gly201
D_2	Ser222
Ar_1	His60

C	
H_1	Val03
H_2	Thr221, Val224, Thr236
H_4	Val103, Phe223
H_5	Val103, Ala104, Thr182
A_1	Val224
D_1	Val224
D_2	Ser222

D	
H_2	Thr221, Val224, Thr236
H_6	Trp98, Thr100, Val103
A_1	Val224
A_3	Gly201
A_4	Ser203

E	
A_1	Val224
A_3	Gly201

Figure 13: Three-dimensional structure-based pharmacophore models of PPE in complex with different inhibitors obtained from the X-ray crystal structures of PDB entries: (A) 1BMA, (B) 1BTU, (C) 1ELE, (D) 1HV7, and (E) 1JIM.[2,141-144] Target amino acid residues are shown as grey sticks. Hydrophobic features are represented as yellow spheres, while hydrogen bond acceptors and donors are represented by red and green arrows, respectively. The associated tables list the different features and the corresponding amino acid residues implicated in each interaction. Images were created with LigandScout.[24]

The construction of the pharmacophore model revealed numerous critical interactions between PPE and inhibitors, involving sixteen key amino acid residues. These residues are distributed across the four sub-pockets of the binding site (S1–S4) and also include essential elements of the catalytic triad and the oxyanion hole.

To enhance the robustness and accuracy of the five structure-based pharmacophore models, an *in silico* alanine scanning mutagenesis was carried out using the Schrödinger suite.[26] This approach allowed us to systematically assess the contribution of selected amino acid residues to the overall binding free energy of the protein–ligand complexes corresponding to the five examined PDB structures (1BMA, 1BTU, 1ELE, 1HV7, and 1JIM).[94,141-144]

Specifically, the computational alanine scanning involved replacing individual residues with alanine and calculating the resulting changes in binding free energy. By comparing the energy values of the wild-type complexes with those of the mutated variants, it is possible to quantify the energetic contribution of each residue to stabilization. This analysis provides critical insights into which residues are essential for maintaining strong interactions and highlights the structural determinants underlying the pharmacophore features observed in each model.

For this purpose, a cutoff of $\Delta\Delta G_{stability}$ >3 Kcal/mol was used to select the key amino acids that were defined as hotspots. The analysis was performed excluding the residue Ala104; moreover, we excluded residues His60 and Ser203, given that these residues play a well-defined role in the catalytic activity of serine protease.

Analysing the results, mutation of residue Val224 resulted in a significant increase in the binding free energy in all examined complexes, as well as mutations of Thr236 and Thr221. In addition, all mutations that presented $\Delta\Delta G_{stability}$ > 3Kcal/mol were considered as relevant, paying more attention to residues Trp98, Val103, Thr221, and Phe223, which emerged as key residues across most of the studied ligand complexes. These residues were considered as hotspots. (Figure 14)

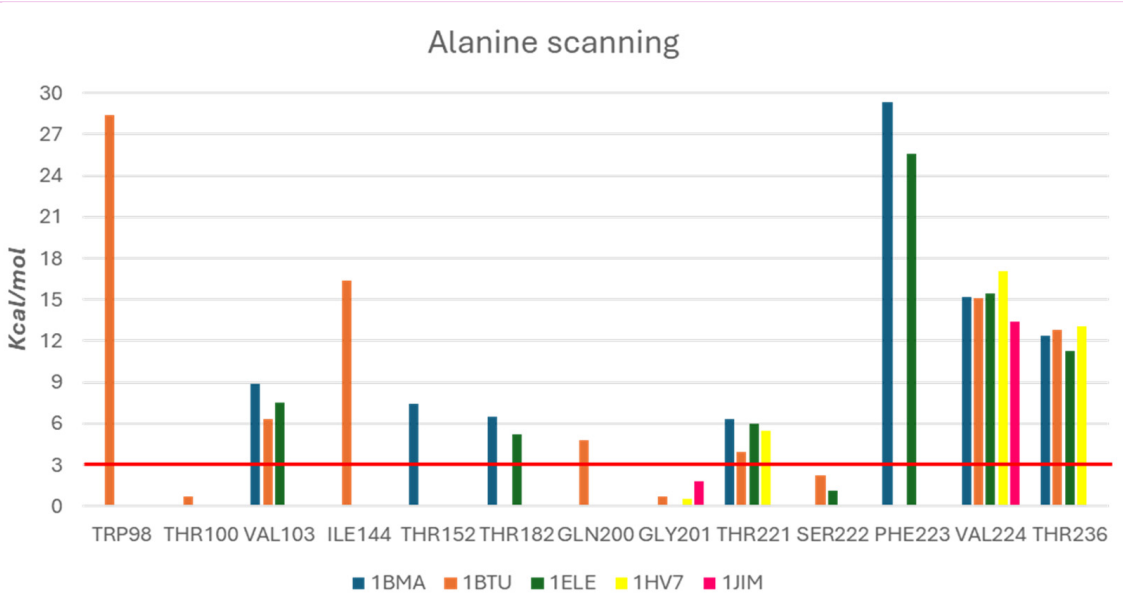

Figure 14: Representation of $\Delta\Delta G_{stability}$ contributions, evaluated using the Alanine Scanning module in the Schrödinger Suite.[26] Each bar is colour-coded according to the corresponding PDB entry and illustrates the interaction between the protein structure and crucial amino acid residues. The red horizontal line indicates the threshold for $\Delta\Delta G_{stability}$ greater than 3 kcal/mol.

The results obtained from the Alanine scanning analysis were used to refine the five initial pharmacophore hypotheses, ensuring that the features identified correspond to residues that contribute significantly to binding affinity. This refinement step was crucial to improve the biological relevance and predictive power of the models, eliminating features associated with residues that play only a marginal role in ligand recognition.

Subsequently, a merged pharmacophore model was generated by combining the conserved features across all five refined models. The final model comprises six hydrophobic features (yellow spheres, H_1–H_6), two hydrogen bond acceptors (red arrows, A_1–A_2), one hydrogen bond donor (green arrow, D_1), and a single aromatic ring (blue disk, Ar_1). In addition, twenty-nine excluded volumes were identified to represent sterically inaccessible regions within the binding site; these are not displayed in the schematic representation shown in Figure 15.

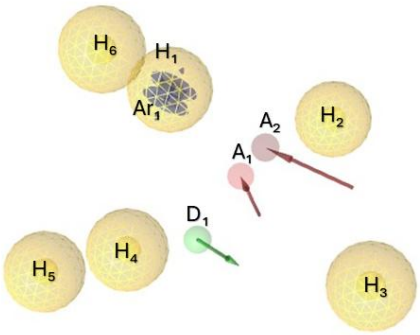

H_1	Val103
H_2	Ile144, Thr221. Val224, Thr236
H_3	Thr152
H_4	Val103, Phe223
H_5	Val103, Ala104, Thr182
H_6	Trp98, Val103
Ar_1	His60
A_1	Val224
A_2	Gln200
D_1	Val224

Figure 15: Merged pharmacophore model, obtained from the refinement of five structure-based models using Alanine scanning analysis. The final model consists of six hydrophobic features (H_1–H_6, yellow spheres), two hydrogen bond acceptors (A_1–A_2, red arrows), one hydrogen bond donor (D_1, green arrow), and one aromatic ring (Ar_1, blue disk). Twenty-nine excluded volumes were also identified but are not shown for clarity. The table summarizes all features and the amino acid residues engaged in each interaction. The image was created using LigandScout.[24]

To enhance the quality and reliability of the pharmacophore hypothesis, and given the high number of features initially identified, molecular dynamics simulations were performed on PPE–inhibitor complexes available in the RCSB Protein Data Bank. Molecular dynamics simulations are particularly valuable for assessing the temporal stability of key protein–ligand interactions under dynamic conditions. In this study, the protein–ligand Root-Mean-Square Deviation (PL-RMSD) was used as a quantitative metric to evaluate the structural stability of each complex throughout the simulation (see Supplementary Materials, Section 5.1).

Furthermore, interactions occurring for more than 30% of the total simulation time were evaluated. Based on this criterion, the following residues were identified as relevant interactions: Thr44, Arg64, Gln200, Gly201, Ser203, Val221, Ser222, Phe223, and Val224.

The combination of these results with the pharmacophore analysis highlighted three principal interaction patterns: (i) persistent polar contacts with Val224 and Gln200, and (ii) stable hydrophobic interactions with Phe223. These findings were subsequently incorporated into the refinement of the pharmacophore model, ensuring that it accurately reflects the most stable and functionally important binding interactions observed in the molecular dynamics simulations. (Figure 16)

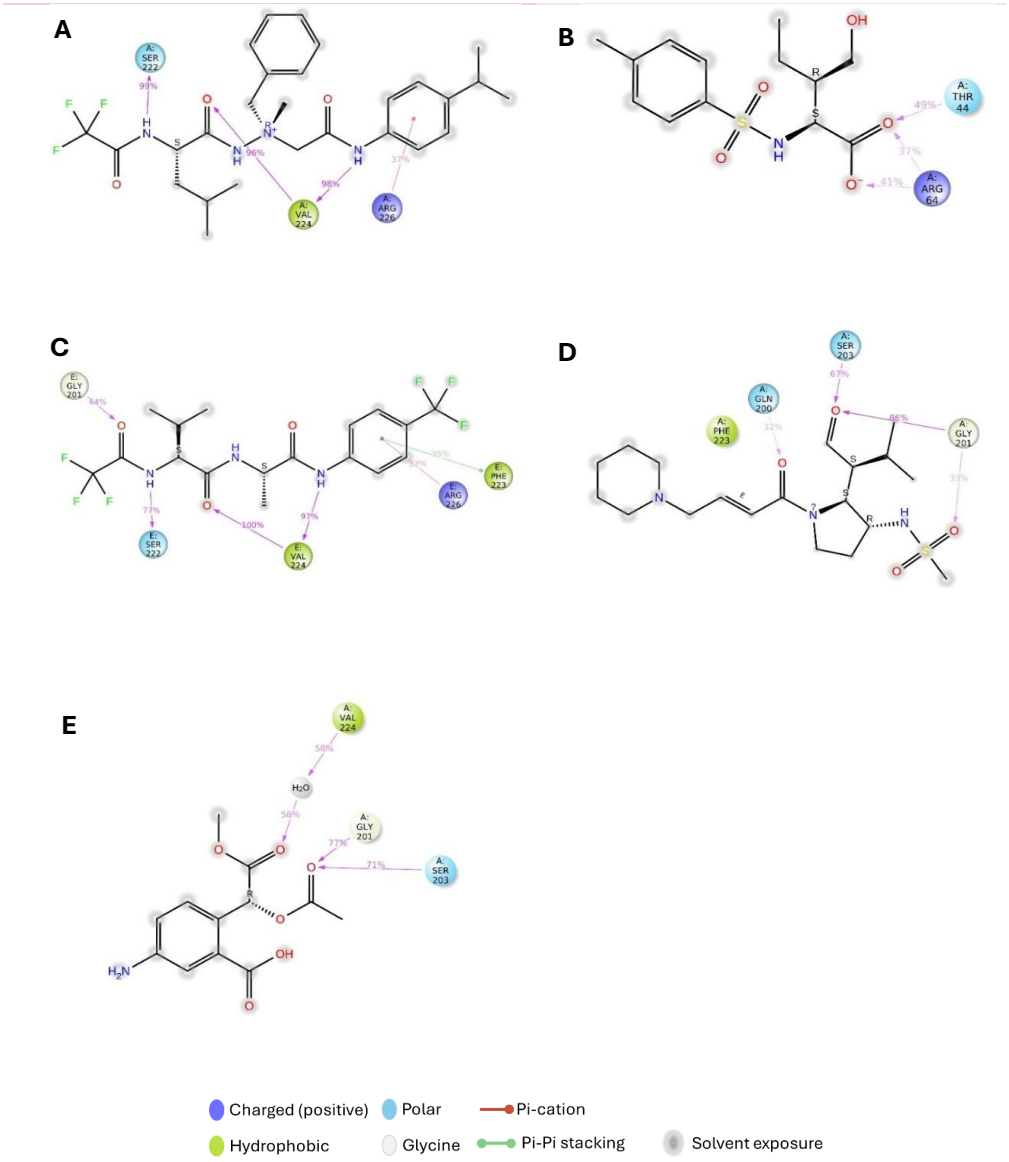

Figure 16: Frequency of residue–ligand interactions exceeding 30% of the total simulation time (500 ns), derived from molecular dynamics simulations of PPE–inhibitor complexes: (A) 1BMA, (B) 1BTU, (C) 1ELE, (D) 1HV7, and (E) 1JIM.

The results obtained from Alanine scanning and molecular dynamics simulations were used to refine and simplify the merged pharmacophore model. This refinement focused on preserving only those pharmacophoric features supported by stable and functionally relevant protein–ligand interactions.

In particular, the hydrogen bond features (A_1, A_2, and D_1) were retained, as they correspond to the crucial contacts with Gln200 and Val224. The hydrophobic features were further optimized as follows: the hydrophobic interaction H_2, associated with Val224, was preserved, along with H_4 and H_5, both of which contribute to stable hydrophobic contacts with Phe223. Given the close spatial proximity of H_4 and H_5, they were merged into a single hydrophobic feature with an increased tolerance radius to account for both interaction regions. Conversely, the redundant hydrophobic feature H_1 and the less relevant hydrophobic feature H_3 were removed to improve model specificity. Twenty-nine excluded volumes were maintained to represent sterically inaccessible regions within the binding site.

As a result of this refinement, the final pharmacophore hypothesis for elastase inhibitors comprises five key features directly related to the interactions with critical residues identified from the combined results of Figure 14 and Figure 16: two hydrophobic features (yellow spheres, H_2-H_{4-5}), two hydrogen bond acceptors (red arrows, A_1-A_2), and one hydrogen bond donor (green arrow, D1), as illustrated in Figure 17.

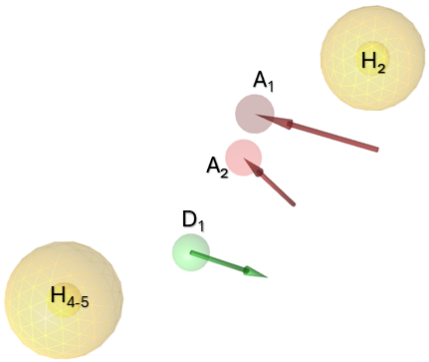

H_2	Val224
H_{4-5}	Val103, Ala104, Thr182, Phe223
A_1	Val224
A_2	Gln200
D_1	Val224

Figure 17: Refined pharmacophore model for PPE inhibitors, derived from alanine scanning and molecular dynamics analyses. The final model includes two hydrophobic features (H_2 and merged H_{4-5}, yellow spheres), two hydrogen bond acceptors (A_1 and A_2, red arrows), and one hydrogen bond donor (D_1, green arrow). Twenty-nine excluded volumes are present but not shown for clarity. The table lists each pharmacophoric feature and the corresponding amino acid residues involved in the interaction. The image was created using LigandScout.[24]

The optimized pharmacophore model was validated using a set of fifteen co-crystallized ligands available on the RSCB Protein Data Bank. The results were reported in the Supplementary Material (see Section 5.1).

Taken together, the results of these studies provide a robust and comprehensive framework for guiding subsequent drug discovery efforts. By integrating pharmacophore modelling, alanine scanning, and molecular dynamics simulations, the analysis identifies the key interactions and structural features critical for ligand binding within the PPE active site. Although minor differences between PPE and HNE may influence ligand recognition, the only key residue variation observed in the analysed region is the substitution of Gln200 in PPE with Phe192 in HNE, which is not expected to significantly impact the overall binding pattern. Therefore, the resulting PPE-based pharmacophore can be considered as a suitable surrogate for the preliminary screening of elastase inhibitors.

Based on the optimized pharmacophore model, a virtual screening was carried out on the in-house synthetic compound library, called CHIME23, which consists of a wide range of small heterocyclic molecules previously developed as active ligands in various human pathological contexts, including antiviral, neuroprotective, anticonvulsant, and anticancer applications. The screening identified molecules belonging to the class of N-substituted-[1H-benzimidazol-2-yl]thio]acetamides, a scaffold originally designed as a non-nucleoside reverse transcriptase inhibitor for HIV-1.[145]

Among these, seven compounds, designated **1**–**7**, were selected because they exhibited high pharmacophore fit scores, as shown in Figure 18.

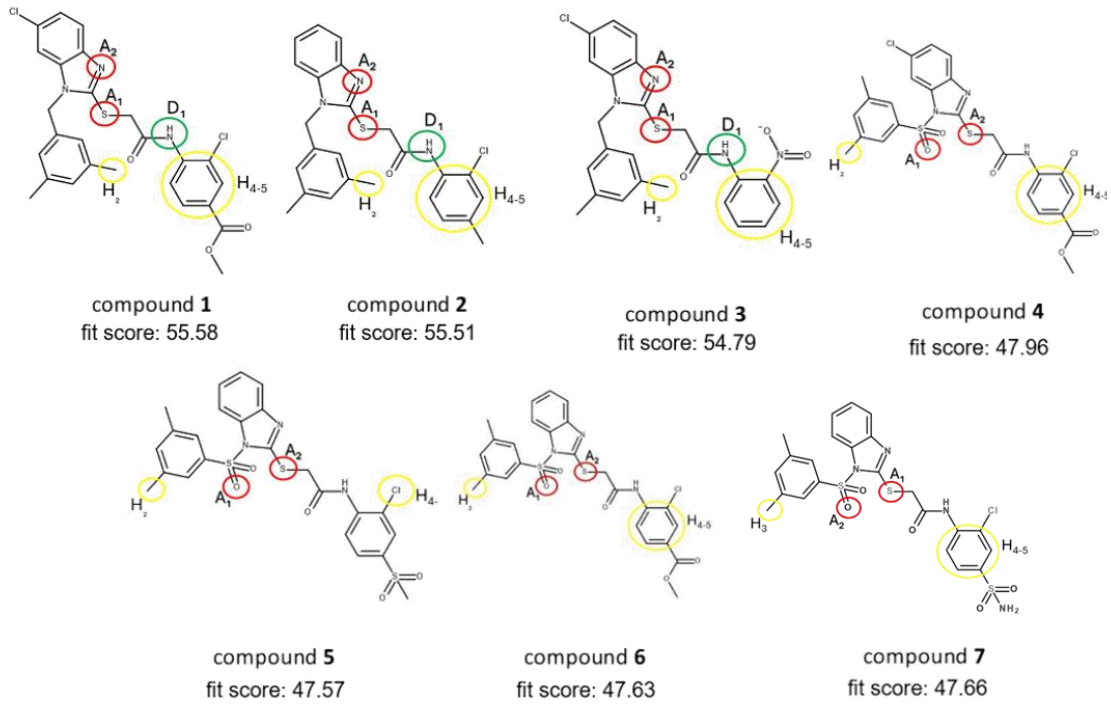

*Figure 18: Chemical structures of the seven N-substituted-[1H-benzimidazol-2-yl]thio]acetamide derivatives (compounds **1**–7) identified through pharmacophore-based virtual screening of the in-house library CHIME23. The structures highlight the pharmacophore features mapped onto each molecule, including hydrogen bond acceptors/donors and hydrophobic regions. Corresponding pharmacophore fit-scores are reported for each compound, indicating the degree of alignment with the optimized model.*

For the subsequent *in vitro* investigations, the selection focused on exploring structural variations considered relevant to biological activity, such as the nature and position of substituents on the benzimidazole-fused benzene ring, the presence of either a single or a pair of substituents on the aniline moiety, and the influence of the linker connecting the 3,5-dimethylphenyl group. Compounds **1**, **4**, and **6** were excluded to avoid possible interference arising from the non-specific esterase activity of PPE toward ester groups located at the para position of the aniline moiety.

Accordingly, three derivatives were chosen for experimental evaluation, such as compounds **2**, **3**, and **7**. None of these three compounds possessed PAINS (Pan-Assay Interference Compounds) alerts, as verified through the SwissADME platform (SwissADME, accessed May 12, 2024).

Preliminary biochemical assays were performed by the team of Prof. Antonella Fais at the University of Cagliari, using the PPE protein, the substrate N-succ-$(Ala)_3$-nitroanilide

(SANA), and oleanolic acid as a reference inhibitor (IC_{50} = 25.7 ± 1.38 μM). At a fixed dose of 50 μM, compounds **3** and **7** failed to reach the 30% inhibition threshold, indicating weak or negligible activity under the test conditions. In contrast, compound **2** showed a notable inhibitory activity against PPE, with an IC_{50} = 60.4 ± 1.98 μM. These findings suggest that the N-substituted-[1H-benzimidazol-2-yl]thio]acetamide chemotype represents a promising starting point for the development of novel elastase inhibitors and could be further optimized to enhance potency and selectivity for therapeutic applications targeting elastase-related pathologies.

To explore the potential binding pose of the most active compound **2** and its interaction mode with PPE, we performed a flexible docking study using the crystal structure of the elastase–0QN complex (PDB ID: 1ELE)[94] using software GOLD (v2024).[34,35]

Based on docking analysis, compound **2** engages in hydrophobic contacts with residues Val103, Ala104, Trp179, and Thr182 within the S4 sub-pocket, with its aniline fragment oriented toward this hydrophobic cavity. The amide –NH group forms a hydrogen bond with Val224, consistent with the pharmacophore model and alanine-scanning data. The dimethyl-benzyl substituent and benzimidazole core interact with key residues His60, Gln200, Thr221, Phe223, Val224, and Thr236, belonging to the S1–S2-S3 subsites. Overall, the docking results align well with the pharmacophore-based predictions, supporting the robustness of the computational approach. This validated docking protocol could thus be applied to guide the design of novel analogues of compound **2** and to identify new chemical entities through virtual screening of external compound libraries. (Figure 19)

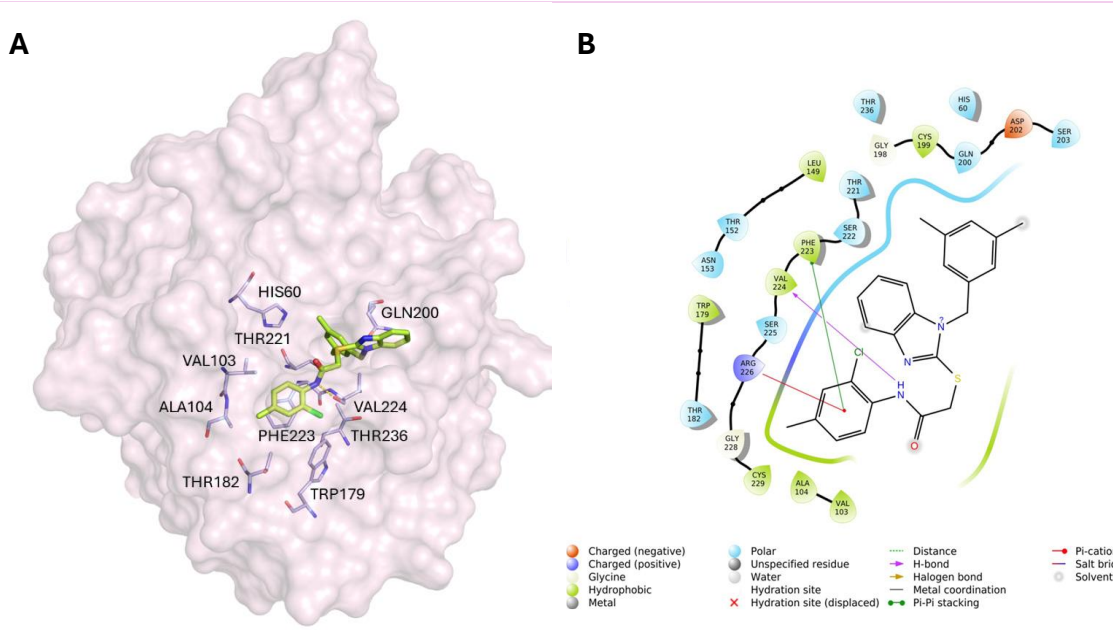

*Figure 19: Predicted binding mode of compound **2** (limon sticks) within the active-site cavity of porcine pancreatic elastase (lightpink surface, RCSB PDB: 1ELE).[94] Key amino acid residues involved in binding are shown as gray sticks. The hydrogen bond with Val224 is depicted as yellow dashed lines. The 3D representation was generated using PyMOL.[41] (B) Two-dimensional schematic of the main interactions between compound **2** and PPE, generated with Maestro.[26]*

3.2 INVESTIGATING THE LIGAND-BINDING PROPERTIES OF N-ARYLBENZIMIDAZOLES AS NOVEL ELASTASE INHIBITORS

The results described in this section have been the object of:

- **Publication:**
  - **Pitasi G**, Floris S, Mancuso F, Savoca G, Gitto R, Fais A, De Luca L. Investigating the Ligand-Binding Properties of N-arylbenzimidazoles as Novel Elastase Inhibitors. *ChemMedChem*. **2025** Dec 21:e202500879. doi: 10.1002/cmdc.202500879.

The previous multistep computational study led to the identification of the N1-arylmethylbenzimidazole derivative **2** (CAS 1562665-34-2, N-(2-chloro-4-methylphenyl)-2-[[1-[(3,5-dimethylphenyl)methyl]-1H-benzimidazol-2-yl]thio]acetamide, Figure 19) as a novel inhibitor of the PPE enzyme at micromolar concentration (IC_{50} = 60.4 μM).[76] This compound became our lead for structural optimization, which led to the discovery of several derivatives with antielastase activity.

Among them, N-(2-bromophenyl)-2-(6-chloro-1-(3,5-dimethylbenzyl)-1H-benzo[d]imidazol-2-ylthio)acetamide (**13**) exhibited the most potent inhibitory effects (IC_{50} = 41.1 μM)

3.2.1 RESULTS AND DISCUSSION

To perform preliminary structure-activity relationship (SAR) analysis, a new series of eight analogues of lead compound **2** (derivatives **8-15**) was designed and evaluated as competitive PPE inhibitors bearing an N^1-arylmethylbenzimidazole scaffold. These new derivatives were developed through simple structural modifications of the starting compound **2**, including the introduction of a chlorine atom at position C-6 (R_1) of the benzimidazole core and the substitution of the groups at positions 2 and/or 4 of the aromatic tail (R_2-R_3). (Figure 20)

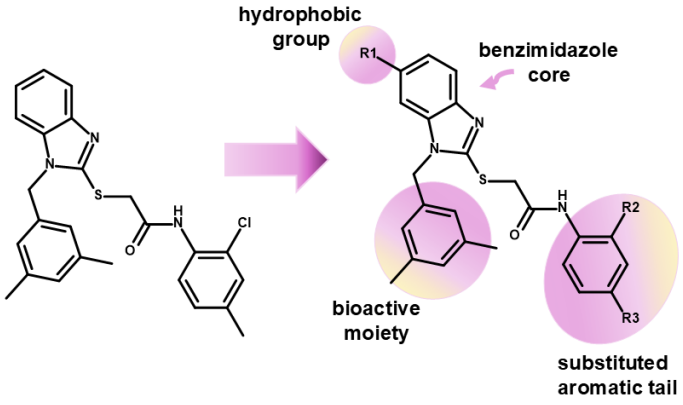

*Figure 20: Chemical structure of the starting compound **2** (N-(2-chloro-4-methylphenyl)-2-[[1-[(3,5-dimethylphenyl)methyl]-1H-benzimidazol-2-yl]thio]acetamide) and designed analogue derivatives, defined as compounds **8-15**. The image was created with Biovia Draw.*[120]

Compounds **8-13** were synthesized by the synthetic chemistry team in our research group. These compounds were subjected to biological assays by the team of Prof. Fais at the University of Cagliari. (Table 5)

Table 5: Percentage of inhibition (I%) at 50 mM against PPE.

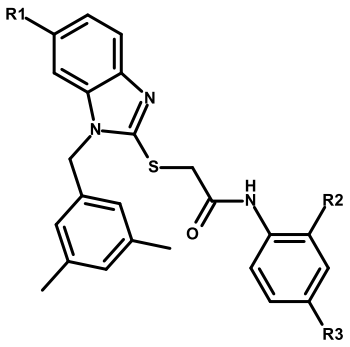

Compounds	R_1	R_2	R_3	%I @50 mM[a]	IC_{50} (µM)
2*	-H	Cl	CH_3	30.0±2.1	**60.4± 2.0***
8	-H	Cl	H	29.1 ±2.3	**N.D.**
9	-H	Br	H	26.5±0.4	**N.D.**
10	-H	Cl	SO_2CH_3	17.3±0.7	**N.D.**
11	-H	Cl	SO_2NH_2	19.3±0.9	**N.D.**
12	-Cl	Cl	H	57.4±2.6	**44.8 ± 1.4**
13	-Cl	Br	H	62.2±2.1	**41.1 ± 1.9**
14	-Cl	Cl	CH_3	40.6±0.7	**N.D.**
15	-Cl	Cl	SO_2CH_3	31.0±0.6	**N.D.**
oleanolic acid					**25.7 ± 1.38**

[a] I % values represent the mean ± standard deviation for three independent measurements (n = 3). * Data taken from reference.[76] N.D. not determined

Analysing the value of inhibition of this small series, it is possible to underline that removal of the 4'-methyl group on the aromatic tail of the starting compound **2** (R_3) did not affect the inhibitory effect. Consequently, the unsubstituted compounds, **8** and **9**, exhibited the same activity as the prototype compound **2**. As expected, introducing polar groups, such as $-SO_2CH_3$ or $-SO_2NH_2$, reduces the ability to inhibit PPE. Notably, all compounds with a chlorine atom at C-6 exhibited enhanced inhibitory effects compared

to the corresponding unsubstituted compounds (R_1=H). The most interesting compounds, **12** and **13**, showed a chlorine atom in the C-6 (R_1) and a halogen atom in the 2'-position of the phenyl moiety. Compounds **12** and **13** show IC_{50} values of 44.8µM and 41.1µM, respectively. Then, kinetic characterization using Lineweaver-Burk plot analysis revealed straight lines with different slopes intersecting at the Y axis (Figure 21 A-B), thus supporting competitive inhibitory effects. The inhibition constant (Ki) for inhibitors that bind to free enzyme (E) was obtained from the secondary graph as 25.8 µM (compound **12**) and 21 µM (compound **13**) (Figure 21 C-D). The analysis of the inhibition mechanism was performed by the team of Prof. Fais at the University of Cagliari.

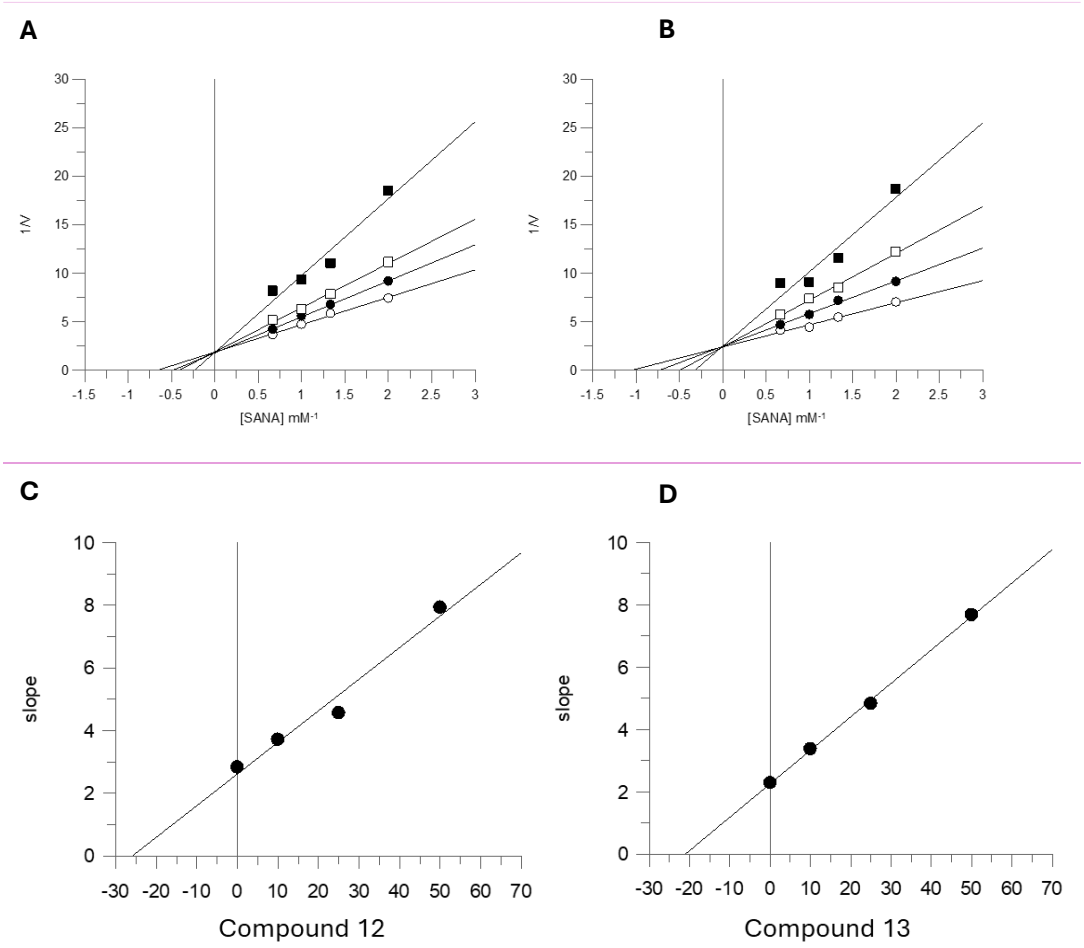

Figure 21: Inhibition of PPE activity by compounds 12 (A) and 13 (B). Lineweaver–Burk plots illustrating the inhibition of PPE activity using SANA as the substrate at concentrations of 0.5, 0.75, 1.0, and 1.5 mM-1. Each compound was tested at concentrations of 0 µM (○), 10 µM (●), 25 µM (□), and 50 µM (■). Secondary plots of the slope (Km/Vmax) versus the concentration of compound 12 (C) and compound 13 (D), used to determine the inhibition constant (Ki).

To rationalize the different activity values of this new class of PPE inhibitors and investigate their binding modes, in silico studies were performed. Molecular docking and dynamics simulations of compounds **12** and **13** were described in detail below, while the results for the other compounds in the series are reported in the Supplementary Material (See Section 5.2) Analysis of the protein-ligand interactions revealed a conserved binding mode for both compounds, characterized by key stabilizing hydrophobic contacts with different amino acid residues, such as Phe223, Val224, as well as the formation of a hydrogen bond with Arg226. In addition, both compounds established a halogen bond between their halogen substituent and residue Val224, further contributing to complex stabilization. (Figure 22).

MM-GBSA binding free energy calculations [23,26] on docked protein-ligand complexes showed binding free energies of -111.38 kcal/mol for compound **12** and -112.34 kcal/mol for compound **13**, showing highly favourable interactions. These computational results align well with the experimental inhibitory activity data for both compounds. (See Supplementary Material, Section 5.2)

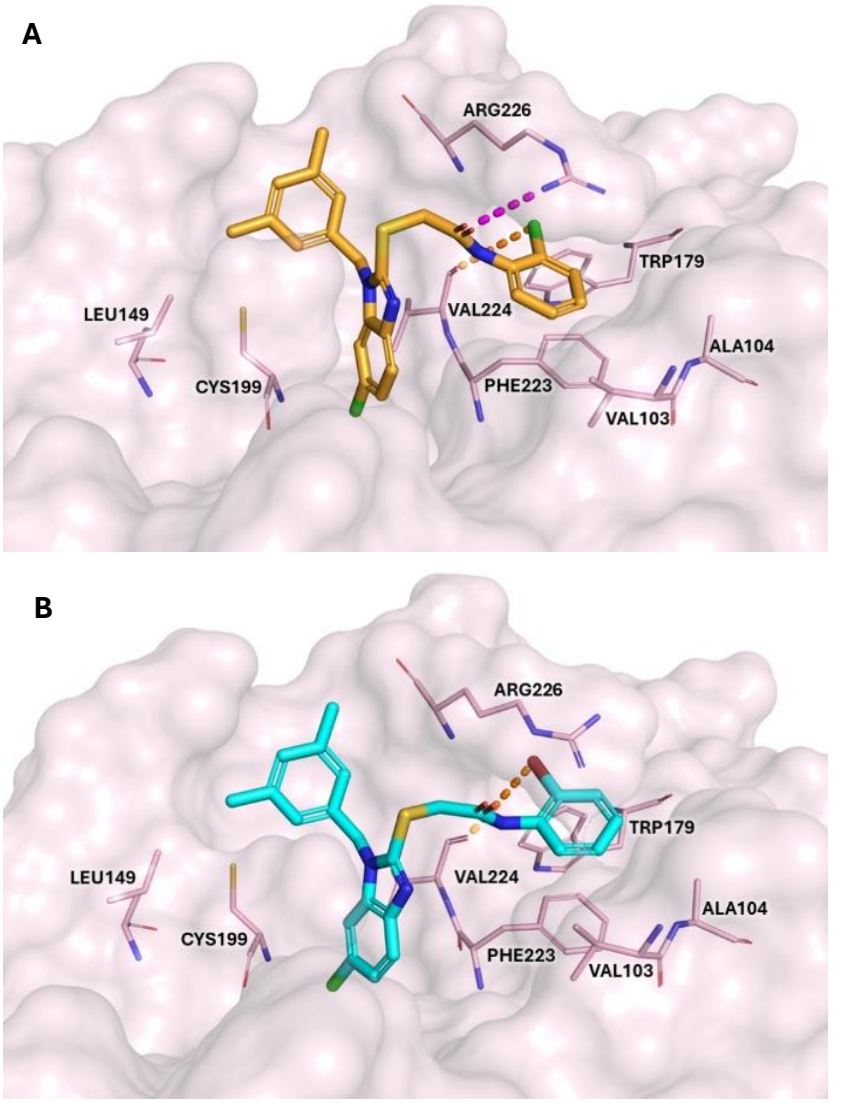

*Figure 22: Molecular docking poses of compounds **12** (A) and **13** (B) within the active pocket of elastase protein (RSCB PDB: 1ELE).[94] The protein is displayed as light-pink surface, while interacting amino acid residues are depicted as sticks in the same colour. Ligands are represented by sticks of different colours, bright orange for compound **12** and cyan for compound **13**, respectively. Hydrogen bonds are described as magenta dashed lines, while halogen bonds are described as orange dashed lines. Images were generated with PyMOL.[41]*

To further evaluate the stability of the protein-ligand complexes, molecular dynamics simulations were performed using three independent replicas for each ligand. (Figure 23) In all simulations, both ligands remained stably accommodated within the binding pocket throughout the simulation time, preserving the key interactions. The three replicas for each ligand showed comparable RMSD trends, and the overall mean trajectory (black line) reflected constant behaviour across simulations. The reproducibility of the results was confirmed by this agreement between replicates and indicates that the limited

fluctuations primarily arise from intrinsic ligand mobility and local conformational rearrangements within the binding site, rather than from any instability of the protein-ligand complexes. (Individual RMSD plots corresponding to each replica are reported in the Supplementary Material; see Section 5.2).

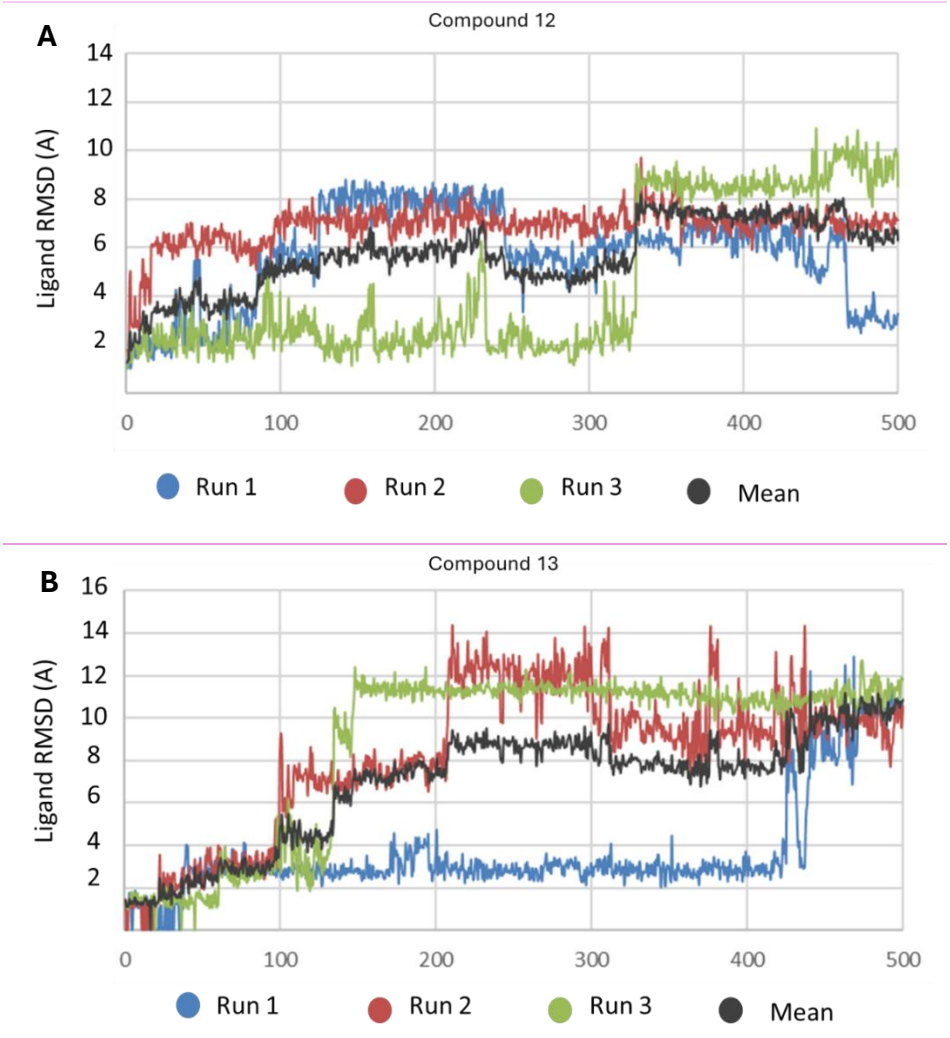

*Figure 23: Root Mean Square Deviation (RMSD) plots obtained from molecular dynamics simulations of PPE-ligand complexes are shown for compound **12** (A) and **13** (B). The simulations were carried out for 500ns and performed in triplicate for each complex.*

To obtain deeper insight into the binding behaviour of derivatives **12** and **13**, a comparative analysis with the starting compound **2** was performed. Given that both ligands, **12** and **13,** exhibited an identical binding mode, only compound **13** was shown in comparison with the binding pose of compound **2** in Figure 24. The superimposition

of the binding poses of compounds **2** and **13** revealed a distinct orientation within the active site. Specifically, the chlorinated benzimidazole core of compound **13** occupied the sub-pocket previously engaged by the dimethylbenzyl group of the reference ligand, whereas its dimethylbenzyl group shifted into the region originally populated by the benzimidazole group of the reference compound **2**. This apparent "binding mode inversion" suggested that the presence of the chlorine atom on the benzimidazole core promotes an alternative ligand orientation, which may be energetically more favourable and contribute to improved stabilization within the active site.

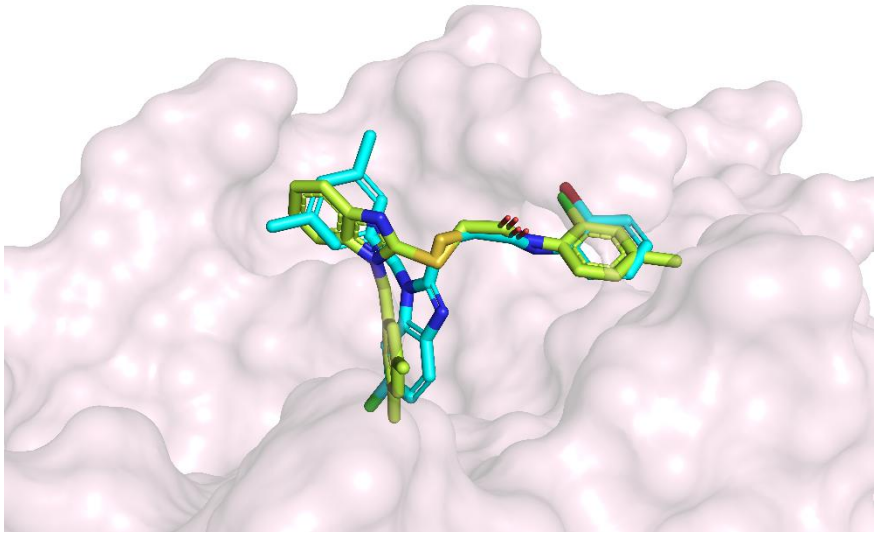

*Figure 24: Superimposition of binding poses of the reference compound **2** (limon sticks) with the compound **13** (cyan sticks). The protein is shown as a light-pink surface (RCSB PDB: 1ELE.[94] Images were created using PyMOL.[41]*

In silico ADME profiling using pkCSM freeware software[40] showed that compounds **12** and **13** exhibited acceptable predicted skin permeability values (-3.207 and -2.777, respectively), were non-sensitizing to the skin and non-mutagenic (Ames test). SwissADME.[37] Analysis revealed no PAINS or Brenk structural alerts, supporting the optimal drug-like profiles of both compounds.

Taken together, these results show that introducing a chlorine atom into the benzylimidazole core has a positive effect on PPE inhibitory activity. This effect is consistent with the ligand binding more favourably within the hydrophobic region of the catalytic site. Computational investigations showed a consistent trend in molecular

docking, molecular dynamics simulations, and MM-GBSA binding free energy calculations, thereby reinforcing the reliability of the observed structure-activity relationships. Collectively, these findings suggest that compounds **12** and **13** have the potential to be new promising lead candidates, characterized by increased lipophilicity compared to the parent compound **2**. This conclusion is further corroborated by enzymatic assays, which demonstrated improved inhibitory potency and revealed a competitive mechanism of PPE inhibition.

3.3 COMPUTATIONAL EVALUATION OF BIOACTIVE CONSTITUENTS FROM NATURAL EXTRACTS AS ELASTASE INHIBITORS

The results described in this section have been the object of:

- **Flash Communication:**
  - **Pitasi G,** Floris S, Mancuso F, Smeriglio A, Trombetta D, Gitto R, Fais A, De Luca L. SCICaSi2025- Società Chimica Italiana Congresso Congiunto delle Sezioni Calabria e Sicilia 2025: "*In Silico Strategies for the Discovery of Elastase Inhibitors as Potential Dermatological Agents";* Università della Calabria -, Italy; 1 - 2 December 2025

The identification of novel non-peptidic elastase inhibitors is crucial for developing alternative therapeutics and provides a robust validation of the applied computational strategy. The strong correlation between computational predictions and experimental enzymatic data confirmed the protocol's effectiveness for rational identification of new elastase inhibitors. This validated approach provides a valuable workflow for screening and optimizing elastase inhibitors derived from natural sources, thereby facilitating the discovery of structurally varied and pharmacologically relevant lead compounds. Therefore, the main constituents of four natural extracts were evaluated using the same computational workflow used for the identification and optimization of reference compound **2**.

3.3.1 RESULTS AND DISCUSSION

The optimized pharmacophore model described in paragraph 3.1.2 was subsequently employed to perform a virtual screening aimed at evaluating the most representative constituents identified in Orange and Lemon raw pomace extracts. The extracts were obtained through collaboration with Prof. Trombetta's research group of the University of Messina. Phytochemical profiling of the raw pomace extracts highlighted flavanones as the predominant fraction when quantitative analysis was considered. Orange extract contained mainly hesperidin (2.36 g/100 g) and narirutin (0.37 g/100 g), whereas lemon extract was dominated by hesperidin (1.20/100 g) and eriocitrin (1.14 g/100 g).[146] Based on their quantitative predominance, these three flavanones were selected for pharmacophore-based virtual screening. All three compounds exhibited a satisfactory fit to the pharmacophore model, matching most required features except one hydrophobic feature (H_2) (Figure 25), suggesting that these flavanones possess the minimum structural requirements to interact with the PPE active site.

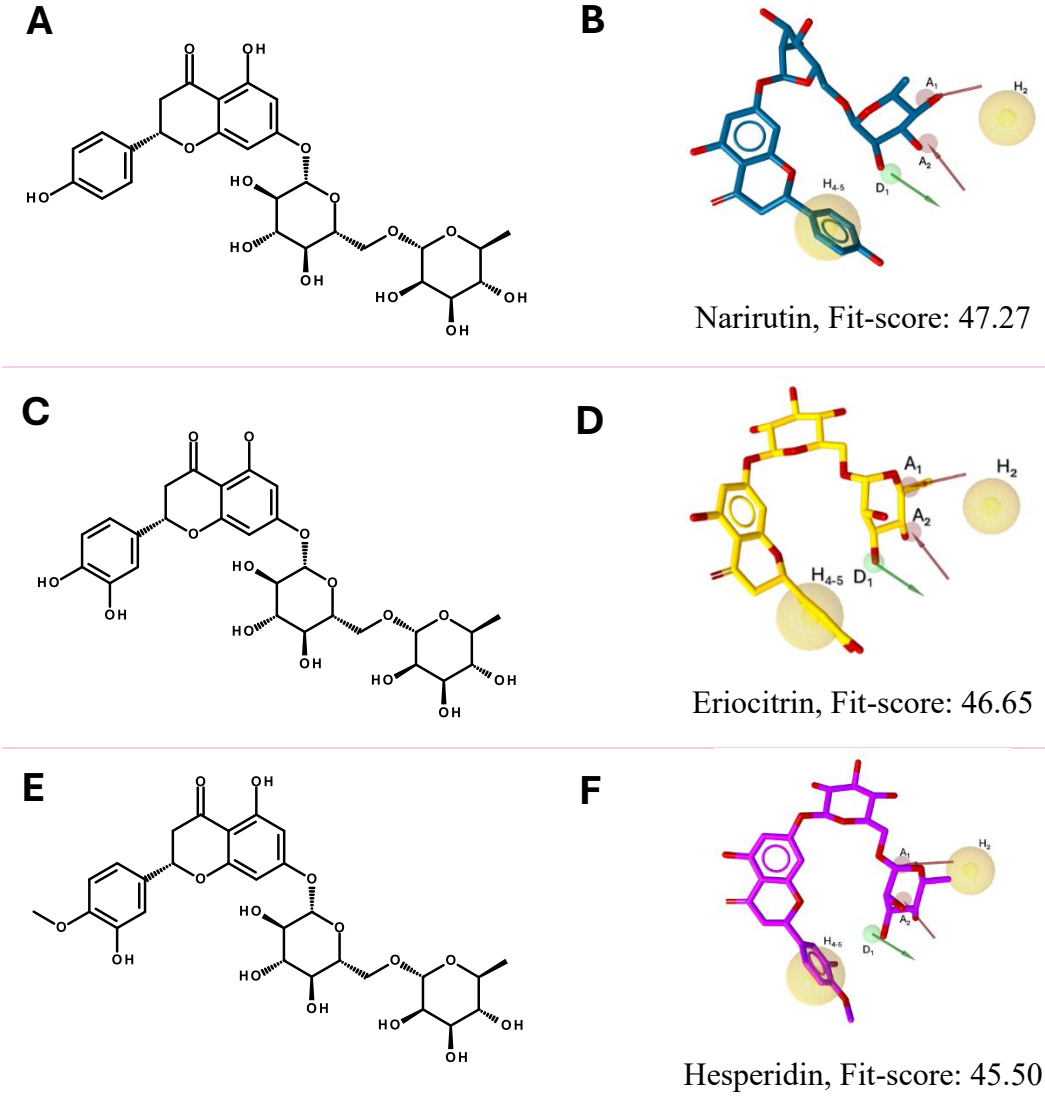

Figure 25: Chemical structures of the three flavanones present in lemon and orange extracts. The structures illustrate the mapping of the optimized pharmacophore features onto each molecule, including hydrogen bond acceptors/donors (red and green arrows, respectively), and hydrophobic regions (yellow spheres). The corresponding pharmacophore fit-scores are reported for each compound, providing a quantitative measure of their alignment with the optimized pharmacophore model. The images were created with LigandScout.[24]

To further rationalize the pharmacophore screening results, molecular docking simulations were subsequently performed, as described in the Materials and Methods section (See Paragraph 3.4). Docking results confirmed the ability of compounds to accommodate within the PPE active site. Although the predicted binding poses shown in Figure 26 do not perfectly match the pharmacophore fit (Figure 25), the compounds assume slightly different orientations while retaining the key pharmacophoric features required for recognition. In addition, the superimposition of the docking (best)pose of

these three flavanones with the co-crystallized ligand (RCSB PDB: 1ELE)[94] and compound **13** (described in Section 3.2) resulted in a comparable binding mode, confirming the reliability of the docking protocol and the plausibility of the predicted poses. (Figure 26) Notably, these three compounds showed the ability to establish an extensive hydrogen bonding network with several amino acids within the PPE active site, including Thr44, His60, Asn153, Gln200, Ser203, Ser222, Val224, and Arg226. These interactions are consistent with stabilization within the catalytic environment. In addition, the binding poses of ligands revealed multiple hydrophobic contacts with residues such as Tyr35, Cys45, Cys61, Val103, Ala104, Trp179, Phe223, and Val224. (Figure 26)

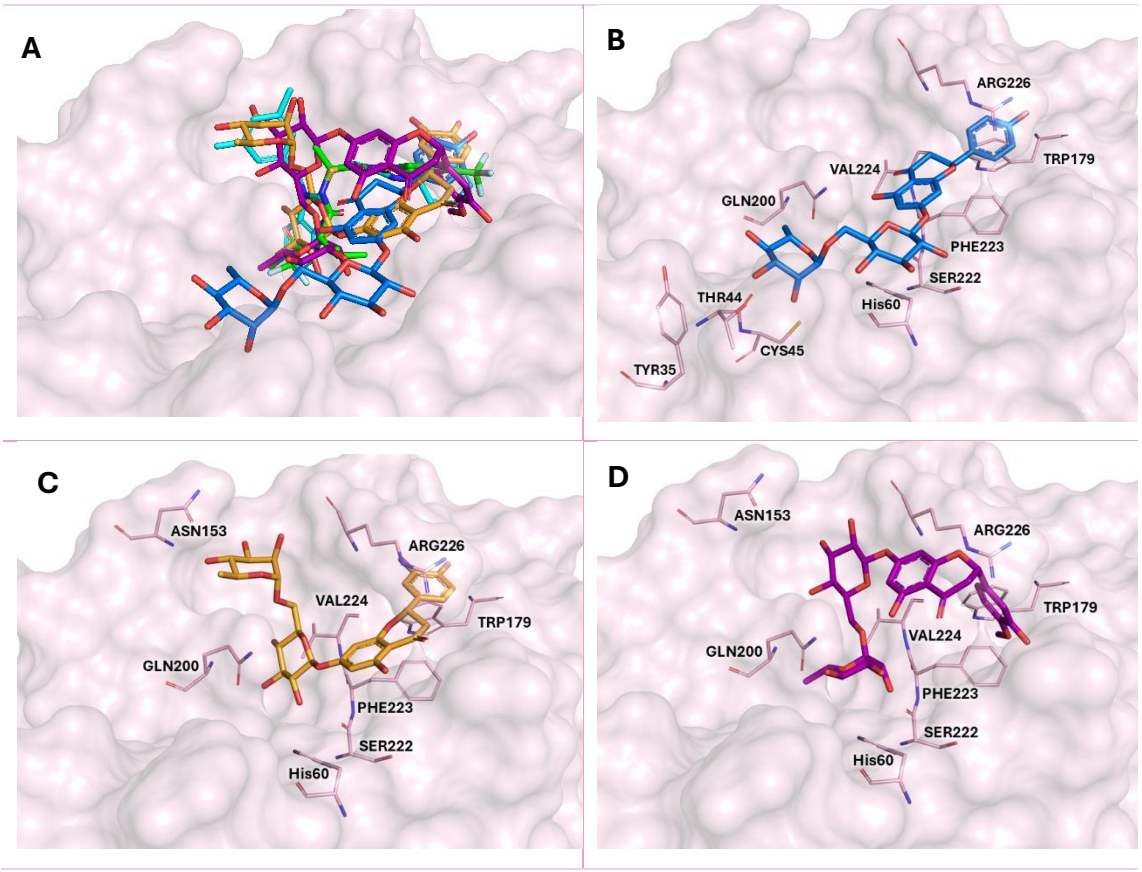

*Figure 26: Docking analysis of the selected flavanones within the PPE active site. The protein is shown as a light-pink surface, with interacting amino acid residues represented as sticks. (A) Superimposition of the docking poses of the co-crystallized ligand (RCSB PDB:1ELE; green sticks) and compound **13** (cyan sticks) with three selected flavanones, Naririutin (marine sticks), Eriocitrin (orange sticks), and Hesperidin (violet sticks). (B) Predicted binding pose of Naririutin. (C) Predicted binding pose of Eriocitrin, (D) Predicted binding pose of Hesperidin. The images were created with PyMOL.[41]*

To experimentally validate the preliminary in silico results, both crude extracts were evaluated for their inhibitory activity against the PPE enzyme at 50 mg/ml. Under these conditions, lemon extract showed weak inhibitory activity (8.3 ± 2.3%), while orange extract showed a moderate inhibition (14.7 ± 2.3%). Although these inhibition levels are relatively low, they remain consistent with the preliminary nature of the screening and the complexity of the extracts tested. Notably, crude extracts contain a mixture of active, weakly active, and inactive constituents, and the effective concentration of individual bioactive compounds is significantly diluted. Overall, the integrated computational workflow remains significantly productive. Future studies may improve the identification of new natural PPE inhibitors by using the evaluation of single pure compounds, structural optimization guided by docking insights, and the exploration of additional natural products derived from *Citrus* fruits or structurally related compounds.

3.4 METHODS AND COMPUTATIONAL WORKFLOW FOR THE IDENTIFICATION OF NOVEL ELASTASE INHIBITORS

Protein selection. To identify the most suitable protein structure for pharmacophore model generation, a systematic search was performed on PPE crystal structures available in the RCSB Protein Data Bank (https://www.rcsb.org/ accessed January 30, 2024). Only structures with a resolution better than 2.5 Å were considered, as higher-resolution data provide more accurate atomic coordinates and better definition of ligand–protein interactions. In addition, an R-factor threshold of <0.20 was applied to exclude structures with poor refinement quality. (Table 6)

Applying these criteria, five PPE–inhibitor complexes were selected (RCSB PDBs: 1BMA, 1BTU, 1ELE, 1HV7, and 1JIM).[94,141-144] A comparative analysis of the binding sites showed that all five inhibitors adopted a similar orientation and interaction pattern within the catalytic site. This high degree of binding mode conservation supported their suitability as structural templates for the pharmacophore model construction.

Table 6: Resolution and R-factor values for the PPE–inhibitor complexes selected from the RCSB Protein Data Bank. These crystallographic parameters were used to assess the quality of the chosen structures.

PDB	**RESOLUTION**	**R-FACTOR**
1BMA	1.80 Å	0.192
1BTU	1.60 Å	0.192
1ELE	2.00 Å	0.171
1HV7	1.70 Å	0.150
1JIM	2.31 Å	0.153

Protein preparation. To prepare the protein structures for further study, water molecules and cofactors were removed using Maestro.[26] For PDB entries 1BTU and 1JIM, amino acid residues were renumbered (Val16–Asn255) with VegaZZ[13] to match the numbering scheme used in the other structures. The 1BTU structure was used as a reference for aligning all other complexes via PyMOL.[41] Protein structures were then processed with the Protein Preparation Wizard (Schrödinger Release 2023-2)[26] using default parameters, with missing chains rebuilt using Prime of the Schrödinger suite.[26,30]

Pharmacophore modelling and validation. Pharmacophore models were generated using LigandScout v2021[24], with one model constructed for each of the five PPE–inhibitor complexes. For each model, the amino acid residues involved in ligand interactions were analysed using the Alanine scanning module of the Schrödinger Suite.[26] Following this analysis, the five individual models were refined and merged into a consensus pharmacophore, which was subsequently further optimized after molecular dynamics simulations.

The final pharmacophore model was validated using a set of fifteen co-crystallized PPE ligands retrieved from the Protein Data Bank (RCSB PDB: 1B0E, 1E36, 1ELD, 1ELF, 1FZZ, 1INC, 1MMJ, 1QGF, 2V35, 3HGP, 4YM9, 6QEN, 7EST, 8EST, and 9EST).

Virtual screening was carried out with the pharmacophore fit score as the ranking metric. The screening mode was set to "*match all query features*," the retrieval mode to "*best matching conformations*", and one pharmacophore feature was omitted to allow

greater flexibility in ligand matching. Eleven out of the fifteen validation ligands successfully matched the model, supporting its predictive reliability.

Molecular dynamics simulations were performed using Desmond (Schrödinger Release 2023-2).[26] Systems were built in an orthorhombic box (10 × 10 × 10 Å) containing TIP3P as the water model. Sodium and chloride ions were introduced to neutralize the system and to maintain a physiological salt concentration of 0.15 M. The OPLS4 force field was applied, with simulations run under NPT ensemble conditions (300 K, 1 atm). A total of five different molecular dynamics simulations were carried out, each for 500 ns. Trajectory analyses, including interaction profiling, were performed using the Simulation Interaction Diagram tool incorporated in the Desmond package.[26]

Molecular docking and validation. The molecular docking protocol was validated through several studies on five different PDBs, evaluating the re-docking of the co-crystallised ligand. Optimal performance was achieved using flexible docking in GOLD with the PPE crystal structure (PDB ID: 1ELE).[94] This structure was selected for subsequent docking experiments because it produced the lowest RMSD value (0.531 Å) between the best-scoring docked pose of the inhibitor and its co-crystallised conformation. The overlay of the experimental and re-docked binding poses of inhibitor 0QN is shown in the Supplementary Materials (See section 5.1)

The grid box centroid for docking studies was defined based on the five co-crystallized ligands used in pharmacophore model generation, with coordinates x = −12.2628, y = 20.1692, z = 37.7359. Amino acid residues within 6 Å of this centroid were set as flexible, including His60, Val103, Gln200, Ser203, Ser222, Phe223, and Val224. Docking studies were performed using a 10 Å box, and the CHEMPLP scoring function, with the "*Allow early termination*" option disabled. Each ligand was subjected to 100 genetic algorithm runs.

Ligands were pre-processed in Maestro using LigPrep,[26] generating possible ionization states at pH 7.0 ± 2.0 with Epik.[27] The best-scoring poses were analysed for binding interactions with the protein using Maestro.[26]

Binding free energy. The binding free energy calculations were performed using MM-GBSA implemented in the Prime module of the Schrödinger suite.[23,26] The VSGB implicit

solvent model was applied in combination with the OPLS2005 force field. Calculations were performed on protein-ligand complexes derived from flexible molecular docking. Prior to MM-GBSA evaluation, all complexes were minimized using the protein-ligand complex refinement utility available in the Schrödinger suite (Schrödinger Release 2025-3).[26] This refinement step was implemented to reduce local steric conflicts and optimize both ligand conformations and the orientation of the side chains of the binding site.

Molecular dynamics. Molecular dynamics simulations were performed in triplicate using the Desmond module in the Schrödinger suite.[26] Each system was built in an orthorhombic simulation box with a 10 Å buffer in all directions and solvated using the TIP3P water model. Counterions (Na^+ and Cl^-) were introduced to neutralize the system and obtain a physiological ionic concentration of 0.15 M. The OPLS5 force field was employed during all simulations, and simulations were conducted under NPT ensemble conditions, preserving a constant temperature of 300K and a pressure of 1 atm. Each trajectory was propagated for 500 ns, and the resulting data were subsequently analyzed using the Simulation Interaction Diagram tool available in the Schrödinger suite.[26]

3.5 CONCLUSIONS AND FUTURE DIRECTIONS

The results obtained from the three complementary studies clearly demonstrate that the integrated application of pharmacophore modelling, molecular docking, molecular dynamics simulations, and MM-GBSA calculations constitutes a powerful and predictive strategy for the identification of elastase inhibitors. The convergence of computational predictions and experimental data highlights the reliability of this approach and supports its potential in guiding the rational design of PPE inhibitors.

The benzimidazole-based scaffold has proven to be a versatile and chemically adaptable structure for PPE inhibition. Further chemical optimization of this scaffold may be very promising. Future efforts should focus on the systematic exploration of substituent effects and linker modifications, guided by validated binding modes to improve potency against elastase.

In parallel, the investigation of *Citrus* flavanones demonstrated the applicability of the optimized pharmacophore model to complex natural extracts. Although the inhibitory activity observed was modest, the computational results confirmed that major flavanones possess the essential structural features required for interaction with the PPE active site. Future studies should therefore include the evaluation of individual pure compounds and other natural extracts.

Moreover, virtual screening of larger libraries of synthetic and natural products represents a logical extension of this work. The validated computational workflow can be applied to identify new chemotypes with improved inhibitory profiles. Finally, to assess the translational relevance of the identified candidates, future studies should include evaluation against HNE as well as testing in appropriate cell or tissue models.

In conclusion, this work lays a solid and methodologically robust framework for the rational development of novel elastase inhibitors. It highlights the strategic value of integrating advanced computational methodologies with experimental validation and shows how this approach can effectively guide identification, optimization, and future translational development in modern drug discovery.

Chapter 4

CASE STUDY II - TYROSINASE

4.1 STRUCTURE-BASED DESIGN AND EVALUATION OF TYROSINASE INHIBITORS TARGETING BOTH HUMAN AND MUSHROOM ISOENZYMES

The results described in this section have been the object of:

- **Publication:**
  - Mirabile S, **Pitasi G**, Floris S, Schira K, Khettabi L, Soler-Lopez M, Scheuermann J, Gitto R, Germanò MP, Fais A, De Luca L. Structure-based design and evaluation of tyrosinase inhibitors targeting both human and mushroom isozymes. *RSC Med Chem*. **2025** Jun 23;16(8):3814-3825. doi: 10.1039/d5md00357a.

- **Poster Communication**:
  - **Pitasi G**, Mirabile S, Schira K, Scheuermann J, Germanò MP, Gitto R, De Luca L. Merck Young Chemists' Symposium 2024: *"In silico studies for the design of new tyrosinase inhibitors as component for skincare products*"; Hotel Sporting & Hotel Ambasciatori-Rimini, Italy; 13 - 15 November 2024

Due to the key role of TYR in hyperpigmentation skin, this enzyme represents a primary therapeutic target for the treatment of this disease. For this purpose, through a combination of computational studies and experimental data, the research group where I conducted my PhD research previously published that compound [4-(4-hydroxyphenyl)piperazin-1-yl](2-methoxyphenyl)methanone (MehT-3) shows comparable activity against AbTYR (IC_{50} = 3.52 μM) and hTYR (IC_{50} = 5.4 μM).[107] Specifically, MehT-3 showed inhibitory activities comparable to Thiamidol™ in hTYR (IC_{50} = 3.8 μM). Based on these promising results, a series of five MehT-3-derived compounds was designated and subjected to computational and experimental studies to investigate their inhibitory capabilities against AbTYR and hTYR.

4.1.1 RESULTS AND DISCUSSION

Starting from the previously reported MehT-3 derivative,[107] the study aimed to investigate the effect of different substituents on the inhibitory activity towards both

hTYR and AbTYR. Design strategies were also based on the hypothesis that insufficient hydrophilicity of MehT-3 could interfere with optimal recognition within the catalytic pockets of both enzyme isoforms. For this purpose, five analogues were designed, each bearing a different substituent at the N-1 position of the piperazine nucleus, as shown in Table 7. The 4-hydroxyphenyl ring bonded to the opposite N-4 atom was retained as a key structural element, essential for interacting with the catalytic cavity of both enzymes.

To reduce lipophilicity, the 2-methoxyphenyl moiety of MehT-3 was replaced with various R^1 fragments containing a polar group or short alkyl chains (1–2 carbon atoms). The R^1 fragments were chosen to preserve the structural motifs required for favourable interactions with both hydrophobic and polar residues located at the entrance to the hTYR and AbTYR catalytic cavities, as previously reported for MehT-3.[107]

*Table 7: Chemical structure of newly designed compounds **1-5** and the starting compound MehT-3.*

	R^1
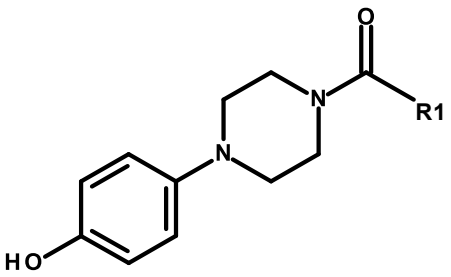	**MehT-3**, 2-methoxyphenyl[107] **1**, 2-$COOHC_6H_4$ **2**, 2-oxo-1,2-dihydropyridin-5-yl **3**, CH_3 **4**, CH_2CH_3 **5**, $CH_2NHCOCH_3$

To begin our study, we predicted the pharmacokinetic properties of these designed derivatives **1-5** to improve the chance of obtaining compounds possessing nice properties compatible with further development for treatment in humans. To predict the pharmacokinetic profile, the calculation of several parameters was carried out by the SwissADME[37] and pkCSM[40] web platforms. In detail, the SwissADME web server (accession date October 18, 2024) predicted that compounds **1-5** had no PAINS and Brenk alerts and all met the Lipinski rule (detailed data in Supplementary Material, Section 5.3). The second pharmacokinetic estimation was carried out by employing the pkCSM web server (accession date October 18, 2024) for all synthesized compounds and for the two reference compounds, such as Thiamidol™ and MehT-3. All designed compounds were

predicted to exhibit adequate skin permeability for transdermal delivery (see logKp values for skin permeability), and displayed favourable human intestine absorption, except for derivative **5**. All compounds present VDss values remaining within the allowed range, except for derivative **1**. Moreover, we calculated selected parameters associated with the metabolic pathway of designed derivatives **1-5**; as a result, none of the compounds was evaluated as a substrate of CYP2D6/CYP3A4; whereas only derivative **4** resulted potential inhibitor of CYP1A2, as found for Thiamidol™ and MehT-3. For the excretion, none of the compounds is expected to be substrates of the renal uptake transporter OCT2, thus minimising potential adverse interactions with concomitantly administered OCT2 inhibitors. Finally, all compounds **1-5** were not predicted to exhibit mutagenic potential in the AMES test, and none of the compounds was associated with skin sensitization as a potential adverse effect. According to these data, it could be predicted that all compounds possessed an acceptable pharmacokinetic profile. The results of these analyses are reported in the Supplementary Material. (See section 5.3)

In the second phase of this study, molecular docking and molecular dynamics simulations were employed to preliminarily investigate the interaction patterns of derivatives **1**-**5** with the AbTYR and hTYR isoforms.

Since compound **2** can undergo tautomerism, its tautomeric state was taken into account in the docking experiments. Specifically, based on the expected tautomeric equilibrium, *in silico* analysis was performed using the keto form, which was selected as the most representative species under the conditions adopted.

All computational analyses were performed using the same protocol, which contributed to discovering the inhibitor MehT-3. In detail, the crystal structure PDB 2Y9X[112] of AbTYR in complex with inhibitor tropolone was used for AbTYR, and the homology structure of hTYR, which is a transmembrane and highly glycosylated protein for which the three-dimensional structure is not currently available.[107]

In depth, docking simulations on the AbTYR cavity revealed that compounds **1-5** adopted binding modes similar to those of reference compound MehT-3. Specifically, the common feature 4-hydroxyphenylpiperazine moiety occupied the area of the catalytic site near the pair of copper ions, as reported in Figure 27; (Detailed interactions are also shown in 2D plots of intermolecular interactions reported in the Supplementary Material,

see Section 5.3). Only for compound **4**, the propionyl chain is oriented towards a different pocket, but it didn't show any clash with the protein.

Then, we can suppose that it is able to create contacts with AbTYR, like the other derivatives, including our active compound MehT-3.

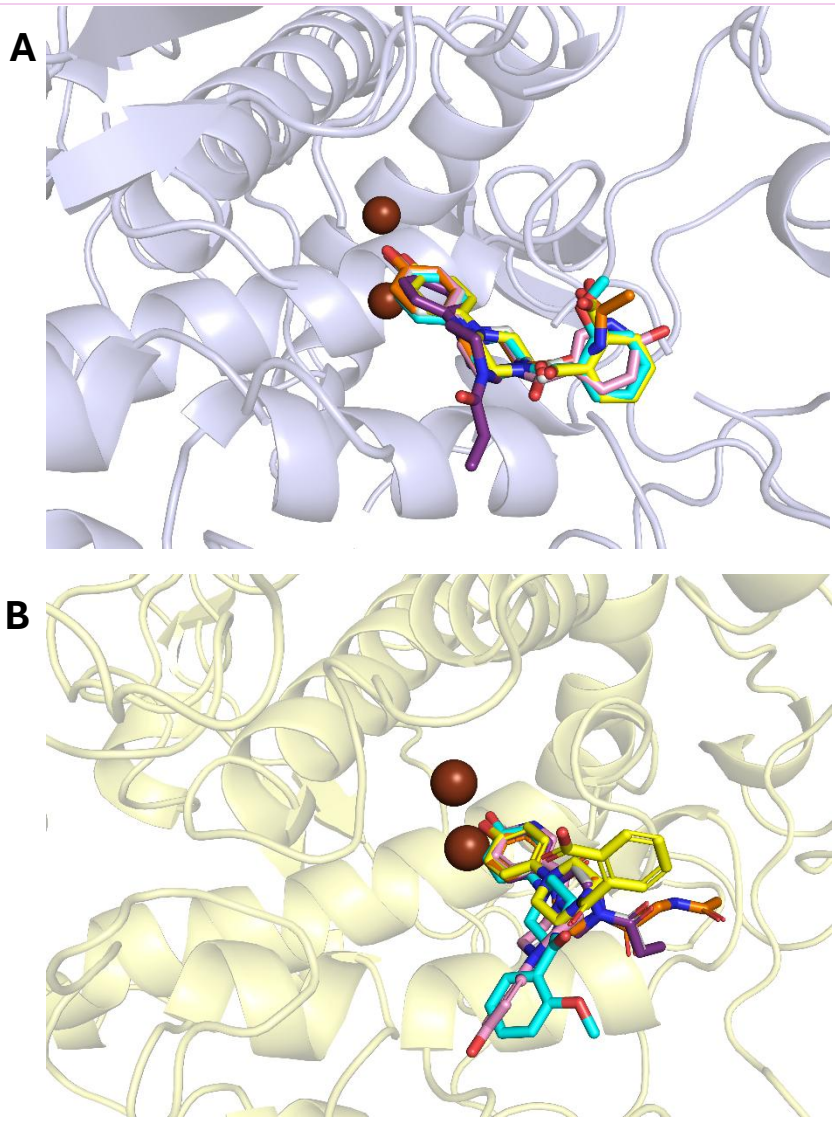

*Figure 27: Superimposition of the ligands with the reference compound, MehT-3, on the AbTYR (RCSB PDB: 2y9x)[112] (A) and homology model of hTYR[107] (B). The ligands are depicted as sticks of different colours: **1** yellow, **2** pink, **3** gray, **4** purple, **5** orange, and MehT-3 cyan. The proteins are represented as lightblue cartoon for AbTYR and paleyellow cartoon for hTYR homology model. Copper ions are shown as brown spheres. Images were created using PyMOL.[41]*

As displayed in Figure 27, the docking simulations within the hTYR active site indicated that the five studied compounds were generally found to occupy the catalytic

cavity; the tail of the **3, 4, 5** and **1** adopted a different orientation in the hTYR binding site when compared to parent active compound MehT-3, indicating that they may interact with the protein in slightly different ways, while still maintaining a similar interaction profile with other regions of the active site. Similarly to MehT-3, the compounds **1, 3, 4,** and **5** are oriented to the 4-hydroxyphenyl moiety towards the copper ions (2D plots of intermolecular interactions are provided in the Supplementary Material, see section 5.3). Instead, compound **2** was capable of coordinating the copper ions with the 4-ketopyridine moiety, whereas the 4-hydroxyphenyl portion exhibited a similar orientation when compared to the 2-methoxyphenyl tail of MehT-3.

To examine the conformational changes and stability of biomolecules over time, molecular dynamics simulations were performed following the protocol outlined in our previous study.[107] Dynamics simulations performed on AbTYR showed good stability of the complexes, as illustrated by the RMSD values (Figure 28).

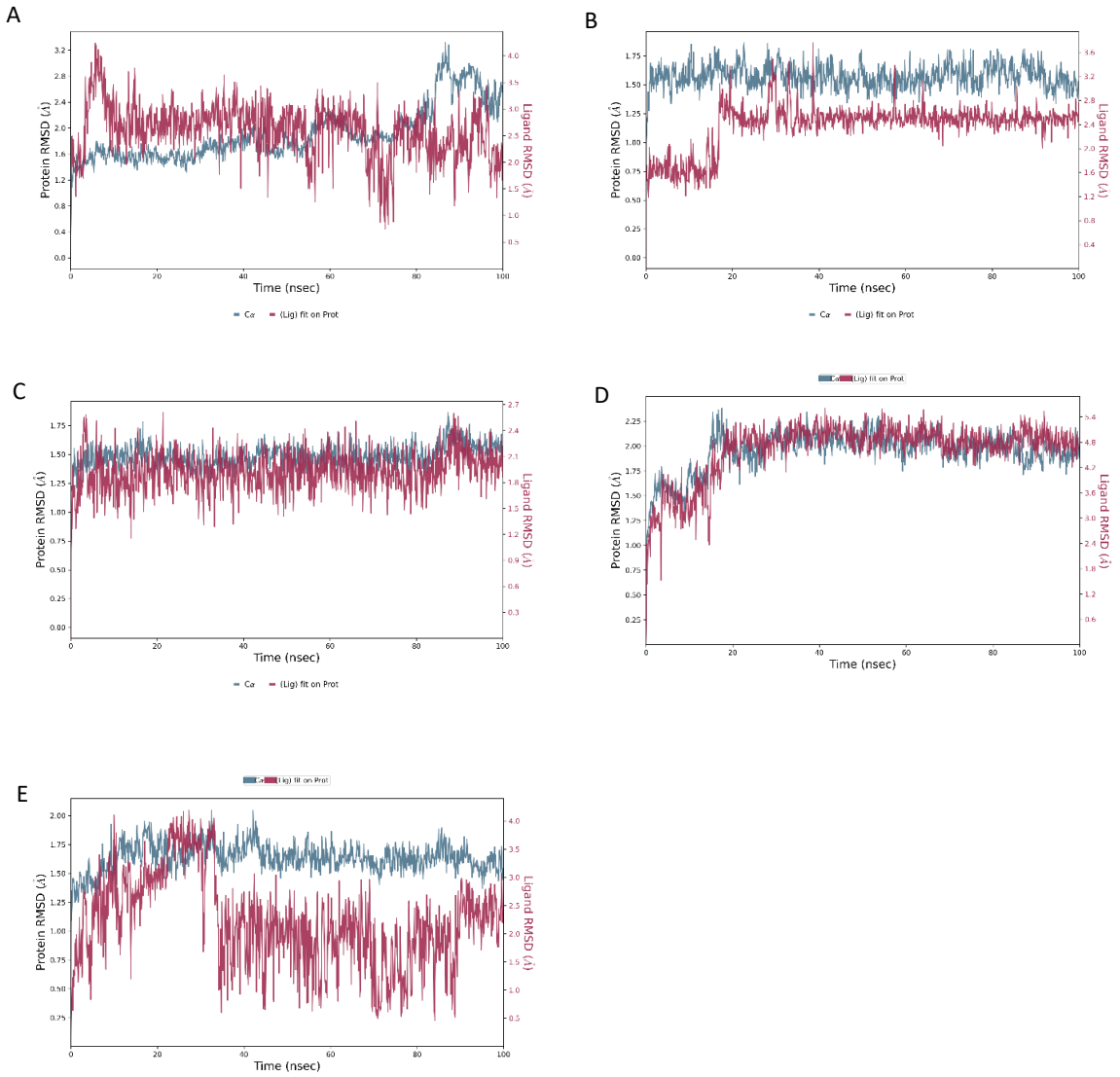

Figure 28: RMSD plots for AbTYR (RCSB PDB: 2Y9X) in complex with different designed compounds ***1*** *(A),* ***2*** *(B),* ***3*** *(C),* ***4*** *(D), and* ***5*** *(E).*

In particular, the protein-RMSD remained below values of 3.2 Å, suggesting that the enzyme structure remains stable during the entire simulation, with no substantial conformational changes. This behaviour represents a positive signal in terms of the reliability of the simulation and the robustness of the ligand-protein interaction. Ligand-RMSD values didn't exceed 5.4 Å, indicating that the ligands remain relatively stable within the binding site while showing a certain degree of flexibility. Overall, these results suggest that protein-ligand complexes remain stable during simulation.

Molecular dynamics studies on the homology model of hTYR[107] (Figure 29) showed protein backbone RMSD fluctuations of 1.5–4.5 Å, suggesting that the protein adopts a relatively stable conformation. Ligand RMSD profiles showed greater fluctuations, particularly for compounds **2** and **4**. Despite these variations, all ligands exhibited lower RMSD values than those observed for compound MehT-3, suggesting enhanced binding stability.

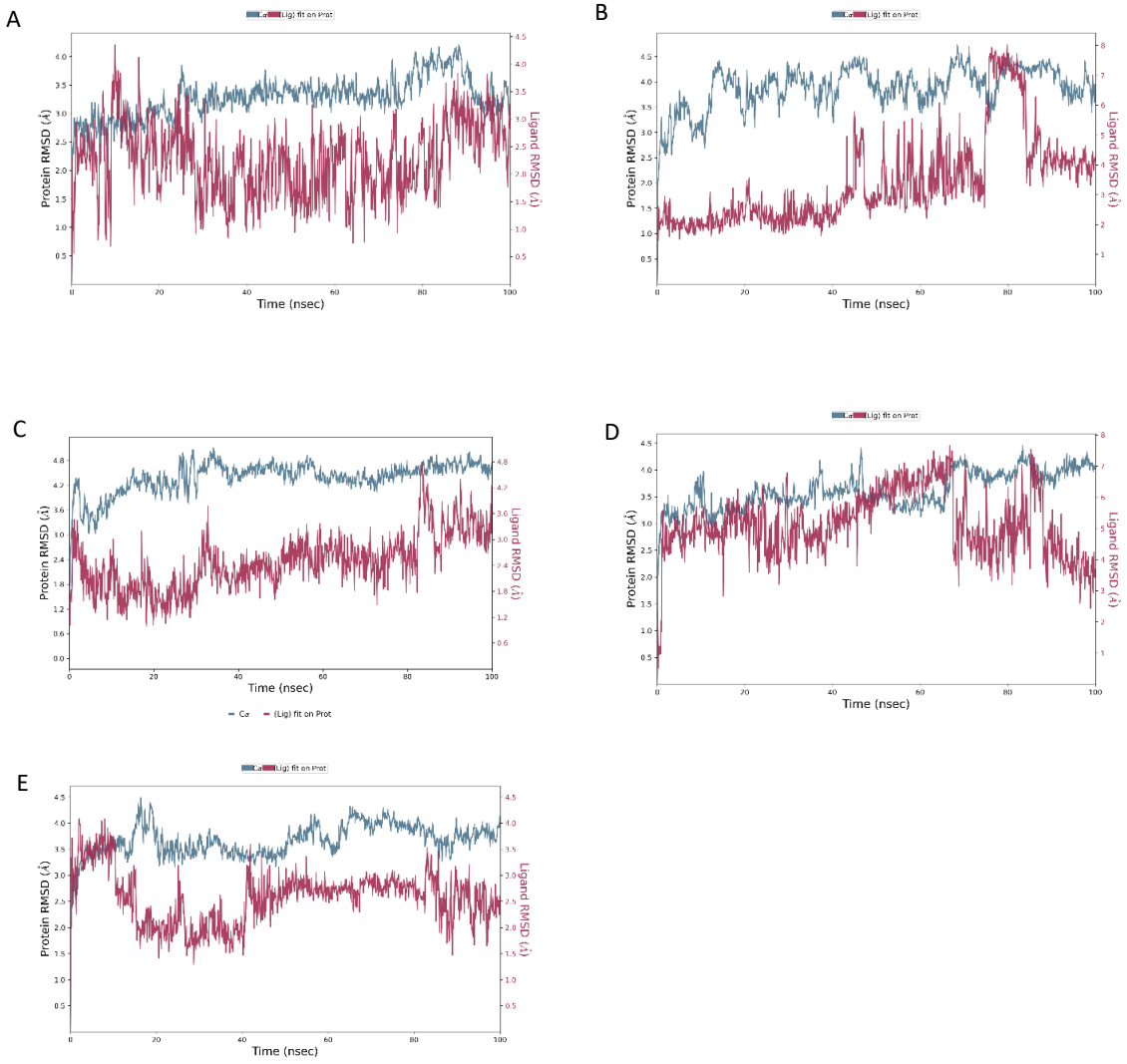

*Figure 29: RMSD plots for homology model of hTYR in complex with compounds **1** (A), **2** (B), **3** (C), **4** (D), and **5** (E).*

Overall, the designed compounds **1-5** were evaluated to establish favourable contacts within AbTYR and hTYR. Based on these computational results, the synthetic chemistry team of our research group was engaged to carry out the synthesis of these proposed compounds. Compounds **1-5** were biologically evaluated through collaborations with biology research groups (Table 8). All showed good inhibitory activity against AbTYR and hTYR, with IC_{50} values in the low micromolar range.

In the AbTYR inhibition assay, compound **5** emerged as the most potent inhibitor, showing comparable activity to reference MehT3. Notably, compounds **2**, **4**, and **5** were more active against AbTYR than kojic acid (IC_{50} = 17.76 μM), which generally serves as the standard reference compound for AbTYR assays.

Regarding the hTYR assay, compounds **2** and **3** have the highest inhibitory activity comparable to MehT-3 and to the marked compound Thiamidol^{TM} (IC_{50} = 3.8 μM).

Considering that melanin synthesis can contribute to oxidative stress through redox-active intermediates that generate reactive oxygen species (ROS) and reduce protective antioxidant levels, antioxidant agents have been demonstrated to mitigate hyperpigmentation and inhibit melanin production. Based on this rationale, a preliminary evaluation of the antioxidant properties of all synthesized compounds was performed via ABTS radical scavenging assay, revealing strong radical scavenging activity across the series, with **2**, **4**, and **5** outperforming the positive control Trolox.

*Table 8: Inhibitory effect of AbTYR and hTYR and antioxidant data for compounds **1-5**.*

ID	AbTYR IC_{50} (µM) *	hTYR IC_{50} (µM) *	EC_{50} (µM) **
1	40.7 ± 3.19^{a}	15.4 ± 1.2^{a}	17.1 ± 0.7^{a}
2	13.24 ± 2.24^{b}	$7.8 \pm 0.8^{a,b}$	9.5 ± 0.2^{b}
3	31.84 ± 3.37^{c}	5.3 ± 0.9^{b}	14.0 ± 0.9^{c}
4	$8.74 \pm 0.36^{b,d,e}$	24.1 ± 3.3^{c}	10.8 ± 0.3^{b}
5	$4.00 \pm 0.25^{d,f}$	27.2 ± 6.2^{c}	10.4 ± 0.1^{b}
MehT-3	$3.52 \pm 0.25^{e,f}$	5.4 ± 0.3^{b}	—
Trolox***	—	—	13.0 ± 1.1^{c}

Experiments were conducted in triplicate; IC_{50} values represent the concentration required to inhibit 50% of enzyme activity. * Different letters denote statistically significant differences between compounds within the same column ($p < 0.05$). Data represent the mean (±standard deviation, SD) of three independent experiments. **Different letters denote statistically significant differences between compounds within the same column ($p < 0.01$). ***Positive control.

Based on hTYR inhibition and antioxidant properties, compounds **2** and **3** were further studied, evaluating their ability to influence the viability of the human skin keratinocyte cell line HaCaT and showed low cytotoxicity in HaCaT cells. Cytotoxicity assays demonstrated that the two compounds displayed no cytotoxicity at concentrations required for effective hTYR inhibition. (Figure 30 A).

To further validate their antioxidant capacity, an antioxidant assay was performed using the skin keratinocyte cell line HaCaT. ROS levels were quantified both before and after H_2O_2-induced oxidative stress, following treatment with compounds **2** and 3 at concentrations ranging from 5 to 50 µM. As illustrated in Figure 30 B, both compounds dose-dependently reduced H_2O_2-induced ROS production. These findings corroborated the antioxidant activity observed via ABTS radical scavenging assay and demonstrated that compounds **2** and **3** effectively mitigate ROS formation in cellular systems.

Finally, the photoprotective activity of compounds **2** and **3** was assessed by determining their sun protection factor (SPF), comparing them to standard photoprotective agents (ferulic acid, caffeic acid, and cinnamic acid; Table 9). The promising SPF values suggest these compounds could reduce UV-induced oxidative

stress and photoaging by limiting UV absorption while providing direct antioxidant protection.

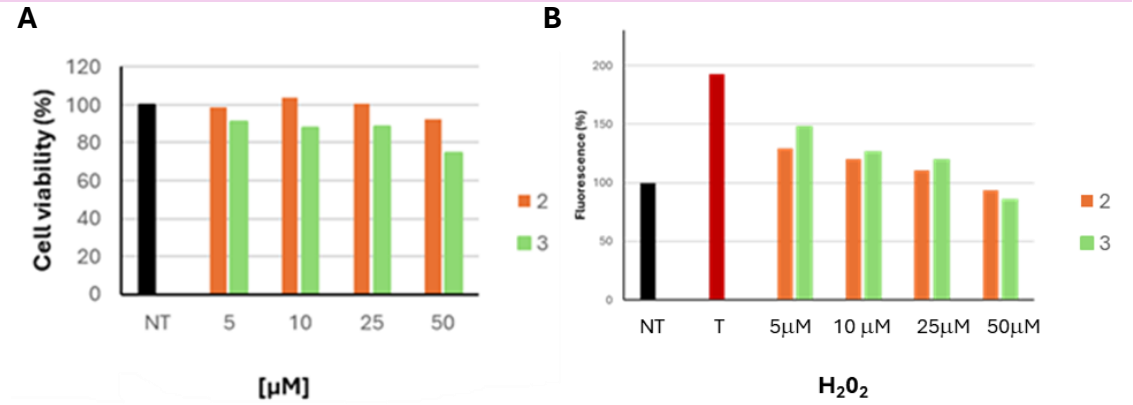

*Figure 30: (A) Cell viability of HaCaT cell line after treatment with varying concentrations of compounds **2** and **3**, ranging from 0 (NT) to 50 μM. (B) Inhibition of H_2O_2-induced ROS generation by compounds **2** and **3** on HaCaT cells. NT, non-treated cells; T, cells treated with H_2O_2 only.*

*Table 9: SPF values of compounds **2** and **3** and ferulic acid (**FA**), caffeic acid (**CA**), and cinnamic acid (**CI**) as reference compounds.*

ID	SPF*
2	7.36±0.02[a]
3	1.62±0.10[b]
FA[#]	7.5±0.2[a]
CA[#]	6.6±0.4[c]
CI[#]	2.0±0.2[b]

*Different letters denote statistically significant differences between compounds within the same column ($p < 0.005$).
[#] Data taken from literature.[147]

4.2 STRUCTURE-BASED DEVELOPMENT AND *IN SILICO* EVALUATION OF TYROSINASE INHIBITORS

The results described in this section have been the object of:

- **Poster Communication:**
  - **Pitasi G**. European School of Medicinal Chemistry (ESMEC): "*Computational approaches to tyrosinase inhibition: focus on 4-hydroxyphenyl-piperazine scaffold";* Palazzo Battiferri-Urbino, Italy; June 29 – July 03, 2025.

To identify novel tyrosinase inhibitors and based on the results obtained previously (see Section 4.1), a series of twenty-eight novel derivatives was designed, maintaining the 4-hydroxyphenylpiperazine core and simplifying the amide moiety to an amine. This structural modification aimed to preserve the essential pharmacophore while improving physicochemical properties and synthetic accessibility. The entire series was screened for inhibitory activity against AbTYR through enzymatic assays, and the most active candidates were subsequently subjected to *in silico* studies to further clarify their interaction profiles.

4.2.1 RESULTS AND DISCUSSION

Considering previous results, a rational structural simplification strategy was conducted by removing the carbonyl group and replacing the original amide moiety with an amine. Twenty-eight novel analogues (**6-33**) were designed and subsequently evaluated through preliminary enzymatic assays against AbTYR. (Table 10)

*Table 10: Chemical structures of the **6-33** and their preliminary inhibitory activity against AbTYR.*

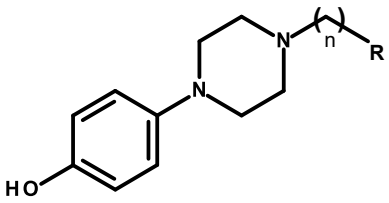

ID	n	R	IC_{50} (μM)
6	1	CH_3	55,48 ± 0.061
7	1	C_6H_5	40.78 ±5.14 μM
8	1	2-F-C_6H_4	40,01 ± 0.071
9	1	3-F-C_6H_4	22,39 ± 0.023
10	1	4-F-C_6H_4	8.20 ±1.38 μM
11	1	2-Cl-C_6H_4	92,03 ± 0.079
12	1	3-Cl-C_6H_4	49,17 ± 0.057
13	1	4-Cl-C_6H_4	31,30 ± 0.010
14	1	2-CH_3-C_6H_4	59,42 ± 0.38
15	1	3-CH_3-C_6H_4	24,40 ± 0.074
16	1	4-CH_3-C_6H_4	18,41 ± 0.033
17	1	2,3-F_2-C_6H_3	122,60 ± 0.312
18	1	2,4-F_2-C_6H_3	9,38 ± 0.012
19	1	2,5-F_2-C_6H_3	77,40 ± 0.126
20	1	2,6-F_2-C_6H_3	66,89 ± 0.220
21	1	3,4-F_2-C_6H_3	10,70 ± 0.021
22	1	3,5-F_2-C_6H_3	24.61 ± 0.046
23	1	2,3-Cl_2-C_6H_3	28,73 ± 0.234
24	1	2,4-Cl_2-C_6H_3	47,91 ± 0.087
25	1	2,5-Cl_2-C_6H_3	6,03 ± 0.025
26	1	2,6-Cl_2-C_6H_3	36,80 ± 0.085
27	1	2,4-$(CH_3)_2$-C_6H_4	73,85 ± 0.105
28	1	3,5-$(CH_3)_2$-C_6H_3	23,62 ± 0.032
29	1	3,6-$(CH_3)_2$-C_6H_3	117,82 ± 0.092
30	1	3-Cl-5-F-C_6H_3	171,10 ± 0.441
31	1	3-Cl-4-F-C_6H_3	0.3 ± 0.001
32	1	3-F-4-Cl-C_6H_3	45,79 ± 0.142
33	2	4-F- C_6H_4	16,39 ± 0.009

This novel library aims to elucidate the contribution of amine substitution to inhibitory potency and selectivity, thus driving further optimization towards more effective and structurally simplified inhibitors.

All synthesized compounds were screened for their inhibitor activity on the diphenolase function of AbTYR, revealing IC_{50} values ranging from 0.3 μM to 171.10 μM. Compound **31** emerged as the most potent ligand of the series, with sub-millimolar potency (IC_{50} = 0.3 μM), while compounds **29** and **30** displayed markedly reduced inhibitory activity (IC_{50} = 117,82 μM and IC_{50} = 171,10 μM, respectively), indicating that their specific structural modifications negatively affect ligand-protein binding. A particularly relevant SAR trend appeared among fluorine-substituted derivatives: compounds **10**, **18**, and **21** (IC_{50}= 8.20 μM, IC_{50}= 9,38 μM, and IC_{50} = 10,70 μM, respectively) consistently showed improved potency, suggesting that fluorine improves target engagement. In the same context, the superior analogue of compound **10**, compound **33**, maintained low micromolar activity **(**IC_{50} = 16.39 μM), confirming the positive contribution of fluorine substitution. Interestingly, compound **25** (IC_{50} = 6,03 μM) showed a good inhibitory activity in the sub-group with chlorine substituents.

Based on these outcomes, compounds **10**, **18**, **21**, **25**, **31,** and **33** were selected as representative candidates for molecular docking studies. All compounds demonstrated the ability to position in proximity of the bi-copper center of AbTYR through the phenolic hydroxyl group. In addition, the aromatic ring establishes π–π stacking interactions with His259 and His263, while further stabilization of the complex is provided by a network of hydrophobic contacts involving Phe90, Phe264, Leu275, Pro277, Met280, Val283, Ala286, and Phe292. (Figure 31) Within this common interaction pattern, the most active compound **31** establishes an additional halogen interaction between the meta-position chlorine atom and the Arg268 residue. (Figure 31 B) A similar situation is observed for compound **25,** which forms an additional halogen bond with Val283 through the ortho-position chlorine atom. (Figure 31 C) These additional specific interactions with Arg268 and Val283 likely contribute to a more efficient stabilization of the ligands within the catalytic site, in accordance with their improved inhibitory profiles. Compound **33** represents a different case; the presence of a longer side chain induces a different binding mode, with the tail extending into a separate region of the binding cavity. However, the

ligand maintains coordination with the copper ions and key contacts, which may explain why it still exhibits appreciable inhibitory activity despite its altered orientation.

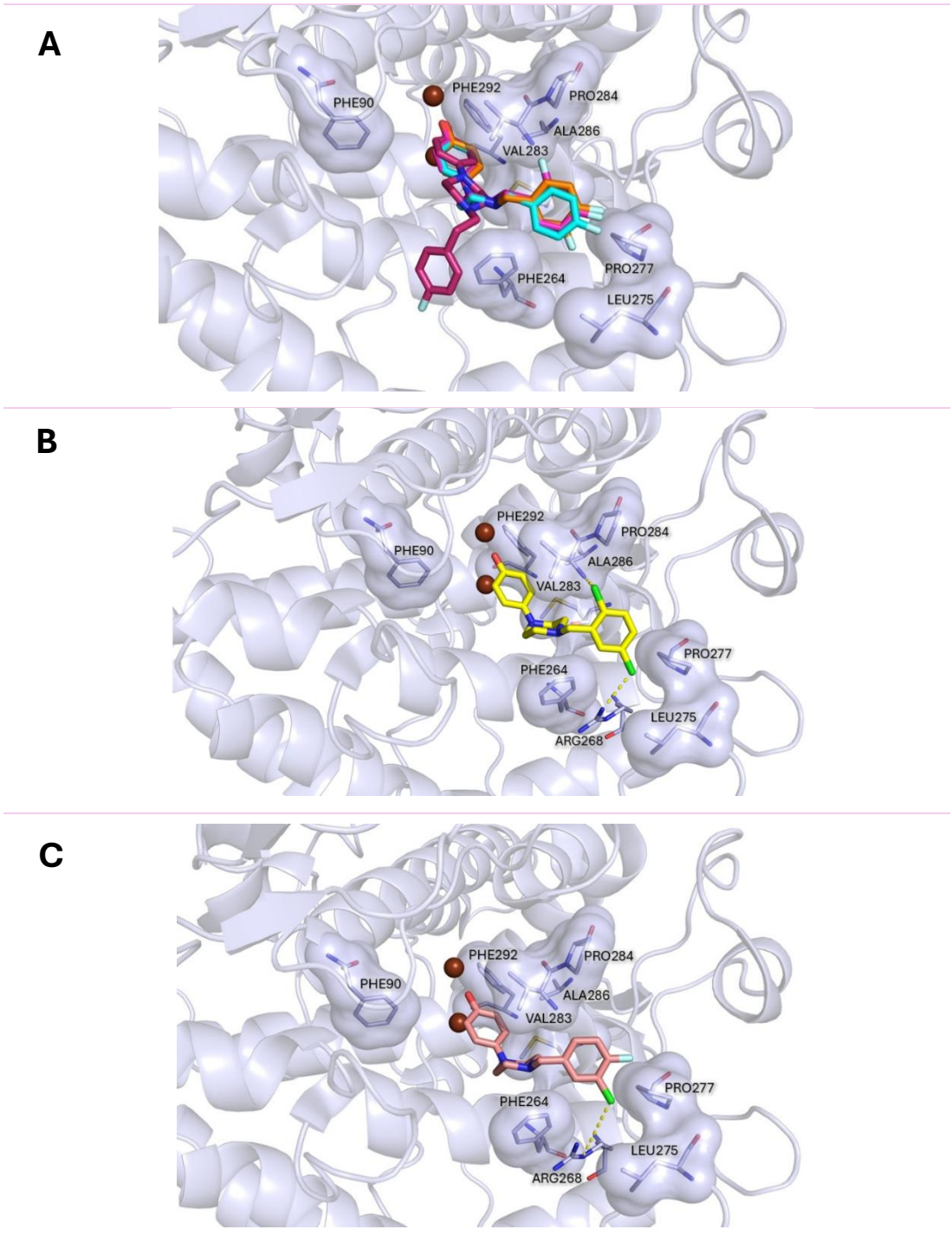

*Figure 31: Molecular docking poses of ligands **10** (cyan), **18** (magenta), **21** (orange), **25** (yellow), **31** (salmon), and **33** (warmpink). within the active site of AbTYR (RCSB PDB: 2Y9X) (A). The binding poses of compounds **31** (B) and **25** (C) are shown in detail. The protein is represented as a lightblue cartoon, with residues involved in hydrophobic contacts displayed as sticks and semi-transparent surfaces of the same colour. Halogen interactions are highlighted as yellow dashed lines. Copper ions are shown as brown spheres. Images were generated using PyMOL.*[41]

To evaluate the potential human relevance of the newly developed AbTYR inhibitors, predictive molecular docking studies were extended to hTYR. Although AbTYR represents a widely used model system for tyrosinase inhibition and allows for efficient screening in the early stages, differences in sequence identity, active site topology, and metal coordination environments may influence ligand recognition in the human enzyme. Therefore, performing a computational binding assessment on hTYR is crucial.

For these reasons, the five compounds (**10**, **18**, **21**, **25**, and **31**) that showed the best inhibitory activity and a conserved binding mode in AbTYR were also subjected to molecular docking studies on a homology model of hTYR. All ligands successfully positioned the phenolic moiety in proximity to the bi-copper catalytic center. The aromatic ring interacted with His202 and His367 through π–π stacking interactions, while additional hydrophobic contacts involving Phe207, Phe347, Ala357, Ile368, Val377, and Phe386 contributed to the stabilization of the ligand-enzyme complexes. (Figure 32) These interaction patterns are consistent with those previously identified as crucial for hTYR inhibition and support the reliability of the predicted poses.[107] Based on these encouraging computational results, the selected compounds are currently being evaluated in enzymatic assays against hTYR to experimentally validate their inhibitory efficacy.

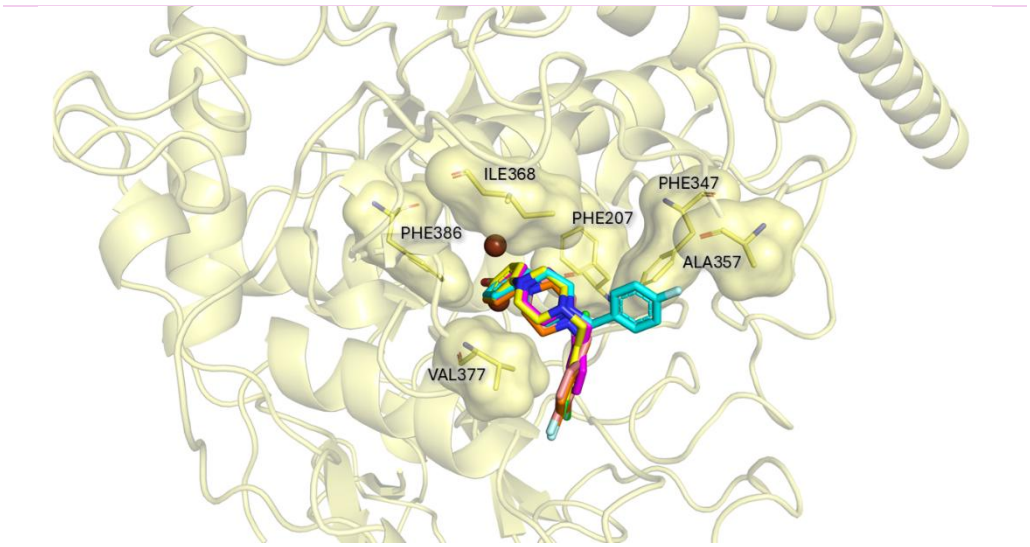

*Figure 32: Molecular binding poses of ligands **10** (cyan), **18** (magenta), **21** (orange), **25** (yellow), and **31** (salmon) within the active site of hTYR homology model.[107] The protein is shown as a paleyellow cartoon, with residues involved in hydrophobic contacts displayed as sticks and semi-transparent surfaces of the same colour. Copper ions are shown as brown spheres. Images were generated using PyMOL.[41]*

The results obtained demonstrate that the optimized 4-(piperazin-1-yl)phenol scaffold is capable of effectively inhibiting tyrosinase, supported by a well-defined interaction model within the catalytic site. The most active derivatives show improved stabilizing interactions, confirming the strong structure-activity relationship that emerged from this study. The promising inhibitory profiles observed encourage continued optimization and support the investigation of these compounds as candidates for future therapeutic strategies targeting pigmentation disorders and melanoma-related processes.

4.3 DEPIGMENTING ACTION AND BIOIMAGING OF LUMINESCENT BODIPY-BASED PIPERAZINYL PHENOL DERIVATIVES

The results described in this section have been the object of:

- **Publication:**
  - Mirabile S, Barattucci A, Bonaccorsi PM, Calderaro A, De Luca L, Germanò MP, Gitto R, Giuffrida A, Monforte M, Patanè GT, **Pitasi G**, Gangemi CMA. Depigmenting action and bioimaging of luminescent BODIPY-based piperazinyl phenol derivatives. Bioorg Chem. **2025** Nov 23;168:109271. doi: 10.1016/j.bioorg.2025.

Previous studies have identified 4-(piperazin-1-yl)phenol derivatives as effective TYR inhibitors and have shown that specific structural modifications can significantly enhance their inhibitory activity. Based on this knowledge, the present work focuses on the rational design of new molecules with dual functionality: tyrosinase inhibition and intrinsic luminescence. To achieve this aim, the consolidated TYR inhibitor pharmacophore was combined with a BODIPY fluorophore, leading to the development of innovative therapeutic candidates.

4.3.1 RESULTS AND DISCUSSION

Previous study identifies [4-(4-hydroxyphenyl)piperazin-1-yl](2-methoxyphenyl)methanone (MehT-3) as a highly effective tyrosinase inhibitor with an IC_{50} value of 5.4 μM and 3.5 μM toward hTYR and AbTYR, respectively.[107]

Notably, it was reported that the portion 4-(piperazin-1-yl)phenol (**PP**) was sufficient to inhibit AbTYR (IC_{50} = 28.9 μM). (Figure 33)

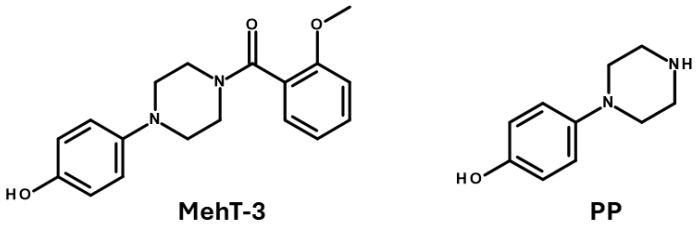

*Figure 33: Chemical structures of MehT-3 and the portion 4-(piperazin-1-yl)phenol (**PP**)*

This result confirmed that the piperazinylphenol moiety is a key determinant for enzyme inhibition, ensuring anchoring within the catalytic site through interactions involving the phenolic group and the dicopper center. These observations highlighted the **PP** core as a minimal pharmacophore suitable for further structural elaboration and functional integration. Based on these findings, a new strategy predicted the combination of TYR-inhibitory activity of the **PP** fragment with the luminescent properties of the BODIPY moiety, aiming to address the lack of luminescent TYR-inhibitor conjugates in the literature. Accordingly, three BODIPY-based 4-(piperazin-1-yl)phenol derivatives **34-36** were designed (Figure 34), evaluated by *in silico* study, and tested *in vitro* on AbTYR. In addition, *in vivo* studies in zebrafish embryos were performed to investigate depigmenting efficacy and biocompatibility.

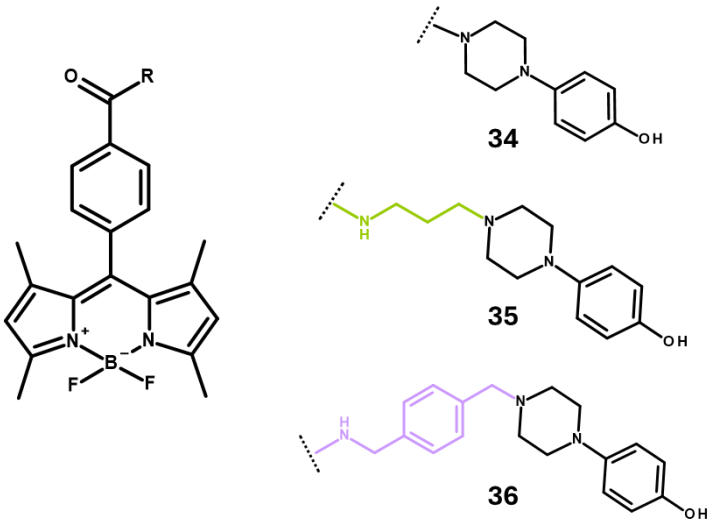

Figure 34: Chemical structure of BODIPY-based 4-(piperazin-1-yl)phenol derivatives **34-36**.

To elucidate the binding mode of the newly developed BODIPY-based 4-(piperazin-1-yl)phenol derivatives (**34-36**) and of the pharmacophore moiety (**PP**) within the active site of AbTYR, molecular docking simulations were performed. The results showed that **PP** is capable of achieving a favourable binding mode into the active pocket, establishing several hydrophobic interactions with amino acid residues Phe90 (F90), Val248(V248), Phe264 (F264), Met280 (M280), Val283 (V283), Ala286 (A286), and Phe292 (F292). Additionally, π-π stacking interactions with two different aromatic residues, such as His85 (H85) and His259 (H259), facilitated optimal ligand anchoring within the AbTYR active site. (Figure 35 A) Docking analysis of the designated BODIPY-derivatives (**34-36**) confirmed that the **PP** core remains oriented towards the copper ions, preserving coordination and the primary interaction network observed for the reference fragment **PP**. Furthermore, compounds **34** and **35** established additional hydrophobic contacts with Leu63 (L63), Tyr65 (Y65), and Ala80 (A80), consistent with the increased steric occupancy imparted by their substituent orientation. Compound **36** exhibited a distinct binding mode within the enzyme cavity, which can affect both its binding strength and conformational stability. Despite their structural length and high conformational flexibility, all three BODIPY-based 4-(piperazin-1-yl)phenol derivatives **34-36** successfully accommodated within the AbTYR active site, supporting their potential ability to inhibit the biological target. (Figure 35 B) To complement the docking results, both docking scores and MM-GBSA binding free energy estimations were calculated

(Table 11). Notably, the new conjugates showed more favourable predicted binding affinities than the parental **PP** fragment, reinforcing the hypothesis that the BODIPY substitution improves target engagement and could result in improved inhibitory activity.

*Table 11: Docking score and MM-GBSA values of **PP** and compounds **34-36**.*

ID	Docking score (Kcal/mol)	MM-GBSA (Kcal/mol)
PP	28.58	-31.59
34	42.24	-58.55
35	53.36	-66.82
36	51.38	-63.60

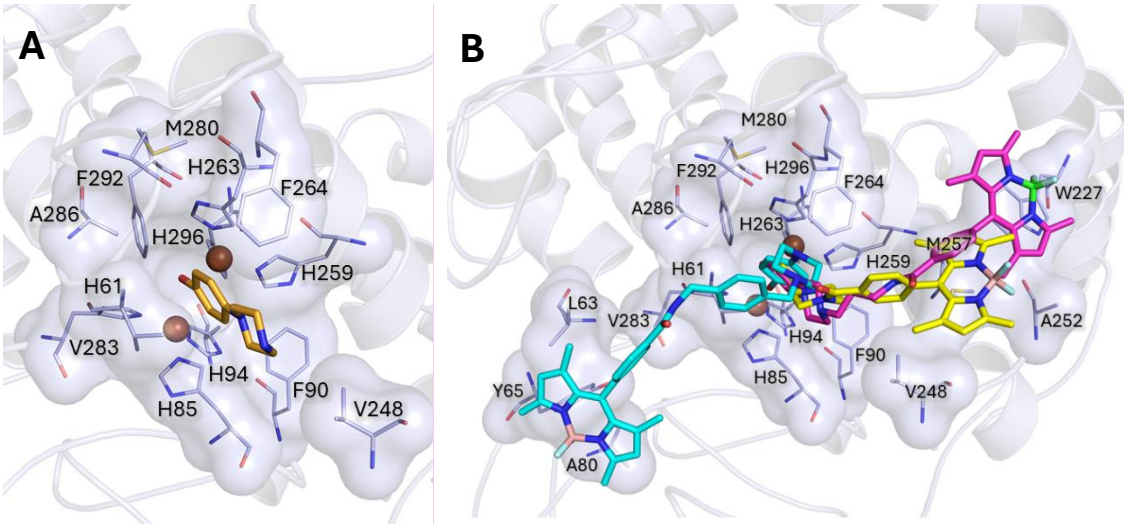

*Figure 35: Representation of docking poses on AbTYR (RCSB code: 2Y9X). The protein is shown as a lightblue cartoon, with the binding site depicted in sticks and the surface of the same colour. The ligands are depicted as sticks in different colours. (A) Binding mode representation of **PP** (orange sticks) within the AbTYR active site. (B) Binding mode of **34** (yellow sticks), **35** (magenta sticks), and **36** (cyan sticks) within the AbTYR active site. Copper ions are shown as brown spheres. The images were created with PyMOL.*[41]

Based on these in silico evaluations, compounds **34-36** were synthesized and subsequently evaluated through *in vitro* assays on AbTYR, followed by *in vivo* studies in zebrafish embryos.

Biological assays showed that all three luminescent derivatives were non-cytotoxic and that two of them, compounds **34** and **35**, present a significant inhibitory effect towards the monophenolase activity of tyrosinase. (Table 12)

*Table 12: Inhibitory activity of three BODIPY-derivatives **34-36** against AbTYR at 440 nm, compared with **PP**. The IC_{50} value of kojic acid (KA) is included as a positive control.*

ID	IC_{50}[a] Monophenolase (µM ± SD)	IC_{50}[a] Diphenolase (µM ± SD)
PP	34.93 ±1.56	34.25± 0.59
34	21.66 ±1.02	Nd
35	17.43 ±2.31	71.34 ±2.79
36	Nd	Nd
KA	70.37±2.49	22.05± 1.62

[a]IC_{50} values represent the concentration that produced 50% enzyme activity loss. All compounds were tested in a set of experiments in triplicate. Nd = not detectable.

The most significant results came from *in vivo* assay conducted on zebrafish embryos using compound **35**, which proved to be the most active tyrosinase inhibitor in the enzymatic assay. The introduction of BODIPY conferred luminescent properties and biocompatibility to the molecule, overcoming the *in vivo* toxicity observed for the parental fragment **PP**. This improvement highlights the potential of such derivatives for future biomedical applications. In addition, compound **35** induced a clear depigmenting effect in the animal model, consistent with its enzyme inhibition profile, thus supporting its relevance as a candidate for modulating melanogenesis. Overall, these findings support the continued development of this chemical platform towards innovative theragnostic solutions for pigmentation-related disorders. Both the synthetic work and the biological evaluations were performed in collaboration with external research groups.

4.4 METHODS AND COMPUTATIONAL WORKFLOW FOR THE IDENTIFICATION OF TYROSINASE INHIBITORS

Docking studies were performed using GOLD software,[34,36] using the same parameters of a validated protocol.

Protein and ligand preparation. The AbTYR structure was previously prepared using the Protein Preparation Wizard of the Schrödinger suite,[26] applying default settings. The homology model of hTYR was prepared as reported in a previous work of Ricci, F, and co-workers.[107] LigPrep was employed to prepare all ligands,[26] by setting OPLS4 as the force field and pH=7.4.

Molecular docking. The docking analyses were conducted using GOLD (v2024).[34,36] Each ligand was subjected to 100 genetic algorithm runs, and the resulting poses were clustered using a threshold value of 0.80 Å. For AbTYR, the crystal structure of the enzyme in complex with tropolone obtained from the RCSB Protein Data Bank (PDB code 2y9X)[112] was used. The binding site was delineated as a 10 Å radius around the coordinates (x: 10.021, y: −28.823, z: −43.596). A modified version of the ASP scoring function, incorporating metal coordination terms, was applied to achieve enhanced re-docking accuracy for the native ligand tropolone. For docking studies on the hTYR homology model, the binding site was delineated based on the overlay with l-Tyrosine from the BmTYR crystal structure (RCSB code: 4P6R) again using a 10 Å radius. For each analysis, the (best)pose from each ligand was evaluated for protein–ligand interactions using Maestro.[26]

Due to their higher molecular size and conformational flexibility, a 15 Å radius was applied for BODIPY-based derivatives to ensure complete accommodation within the docking grid.

Molecular dynamics: molecular dynamics simulations were carried out using Desmond 2024.[26] The systems were incorporated in an orthorhombic box of 15x15x15 Å dimension, parametrized with the OPLS4 as force field, and solvated using the TIP3P water model. To make the total charge of the system neutral, Na+ and Cl- ions were added to ensure charge neutrality and to achieve a physiological salt concentration of 0.15M. Simulations were performed for 100 ns using the NPT ensemble class at 310 K and

1.01325 bar. The results of the molecular dynamics were analyzed using the Simulation Interaction Diagram tool implemented in the Desmond package.[26]

Binding free energy: Binding free energy calculations of the protein-ligand complexes were carried out using the MM-GBSA method, as implemented in the Prime module of the Schrödinger suite.[23,26] The VSGB implicit solvation model was employed in combination with the OPLS2005 force field to estimate the relative stability of the complexes.

4.5 CONCLUSIONS AND FUTURE PERSPECTIVES

Among the various design strategies explored in this section, the 4-(piperazin-1-yl)phenol scaffold consistently emerged as a robust and versatile pharmacophore for tyrosinase inhibition. Structure-activity relationships clearly demonstrated that appropriate modulation of substituents, including the incorporation of halogens, can significantly reinforce binding interactions at the active site and enhance inhibitory potency. Several derivatives achieved low micromolar IC_{50} values against both AbTYR and hTYR, with some exceeding or matching recognized reference agents such as kojic acid, MehT-3, and Thiamidol™. In addition, the introduction of the BODIPY fluorophore successfully transformed the selected inhibitors into luminescent and biocompatible theranostic candidates. Notably, compound **35** exhibited a pronounced depigmenting effect *in vivo* in zebrafish embryos, fully consistent with its enzymatic inhibition profile. Overall, these results validate the design strategy and confirm that this chemical workflow offers excellent perspectives for the development of novel agents targeting tyrosinase. Based on these results, future research efforts should focus both on improving potency and selectivity towards hTYR through targeted structural refinement of the most promising analogues and on evaluating biodistribution, pharmacokinetics, and long-term safety through *in vivo* studies. Finally, it would be interesting to conduct formulation and delivery studies aimed at improving stability and skin penetration for dermatological applications.

5. SUPPLEMENTARY MATERIAL

5.1 SUPPLEMENTARY MATERIAL: EXPERIMENTAL SECTION 3.1

Table S1: RMSD plots of molecular dynamics of protein-ligand complexes available in RCSB PDB (PDB codes: 1BMA (A), 1BTU (B), 1ELE (C), 1HV7 (D), 1JIM (E)).[94,141-144]

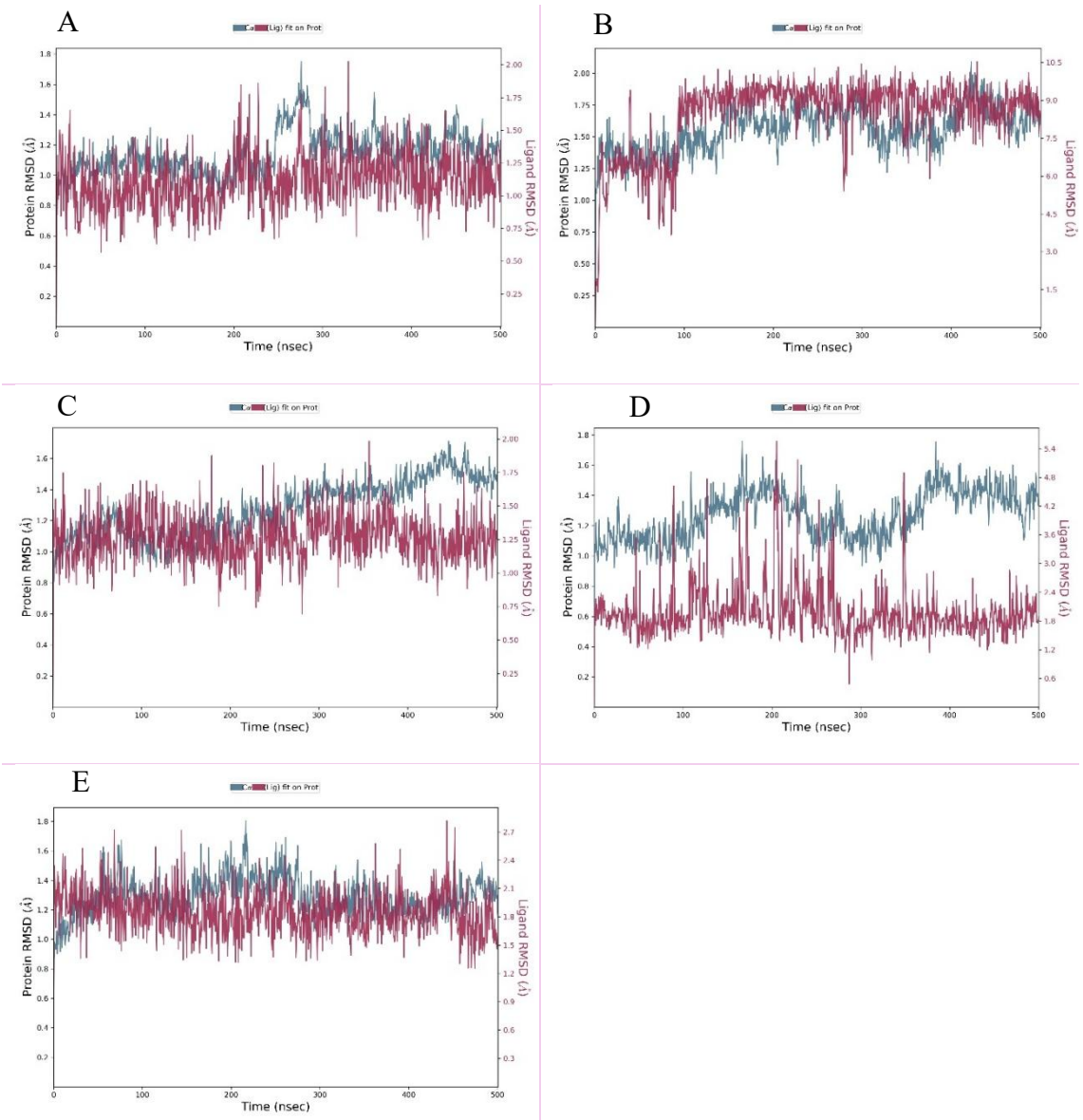

Table S2: List of co-ligands used as a validation set that fit the pharmacophore model and relative pharmacophore fit-score value. The validation set included fifteen ligands co-crystallized with porcine pancreatic elastase (RCSB PDB codes: 1B0E, 1E36, 1ELD, 1ELF, 1FZZ, 1INC, 1MMJ, 1QJF, 2V35, 3HGP, 4YM9, 6QEN, 7EST, 8EST, 9EST). Among them, eleven co-ligands successfully matched the pharmacophore model, and they are shown in the above-reported table.

PDB	Reference/DOI	Structure	Fitscore
2V25	DOI: 10.1039/b706622h	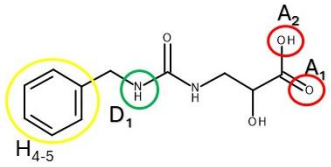	47,17
1QGF	DOI: 10.1021/bi990098y	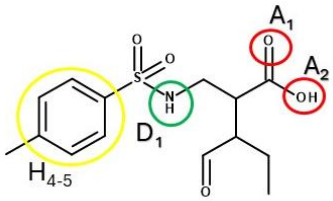	46,90
1E36	**DOI:** 10.2210/pdb1E36/pdb	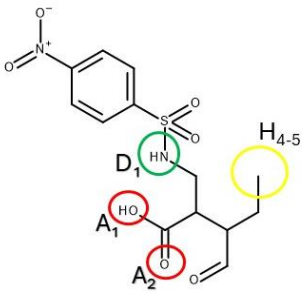	46,46
1INC	DOI: 10.1016/0022-2836(87)90291-9	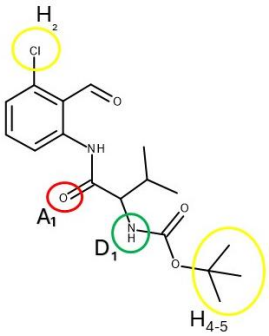	46,38

7EST	DOI: 10.1002/jmr.300030104	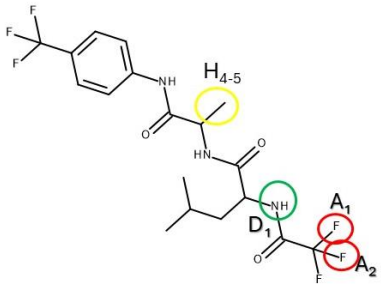	46,28
1ELD	DOI: 10.1021/bi00010a008	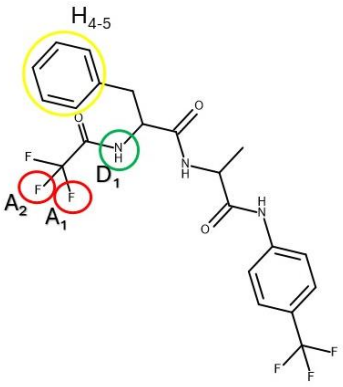	46,18
4YM9	DOI: 10.1002/cmdc.201600258	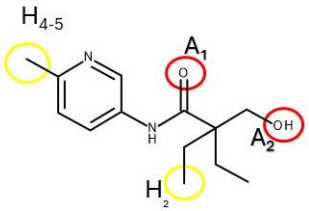	45,77
3HGP	DOI: 10.1021/ja9028846	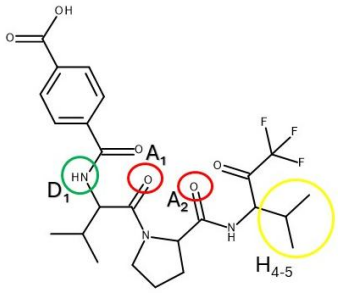	45,38
1FZZ	DOI: 10.1016/s0968-0896(00)00277-7	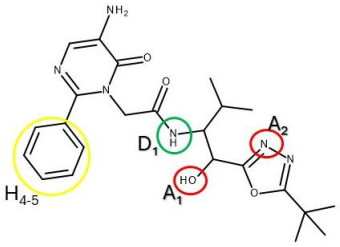	44,20

1B0E	DOI: 10.1021/jm970812e	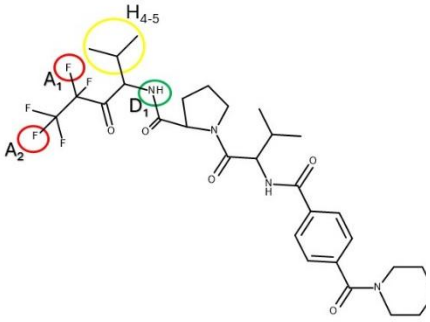	44,13
6QEN	DOI: 10.1021/acschembio.0c00090	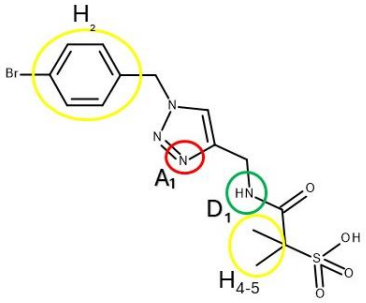	44,00

Figure S1: Superimposition of the best docking pose with the co-crystallized pose of ligand 1ELE.[94]

Flexible docking studies carried out with GOLD software on the 1ELE protein resulted in a (best)pose that restores the co-crystallized pose with RMSD values of 0.531 Å. The co-crystallised ligand pose is shown in orange, while the best docking pose is shown as a yellow stick. The image was created with PyMOL.[41]

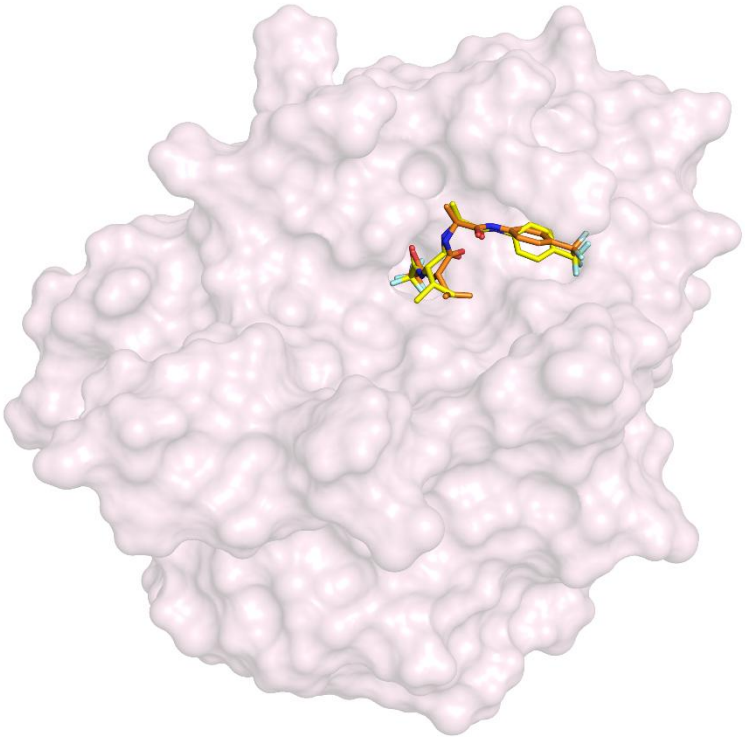

5.2 SUPPLEMENTARY MATERIAL: EXPERIMENTAL SECTION 3.2

Figure S2: Superimposition of the binding poses of ligands **8**–**15** with the reference compound **2**, represented as sticks in different colours, within the active site of porcine pancreatic elastase (PPE — PDB code: 1ELE).[94] The protein structure is represented as a lightpink surface. All ligands are accommodated in a common region of the binding pocket, showing similar orientation and interactions with key active site residues. The image is created with PyMOL.[41]

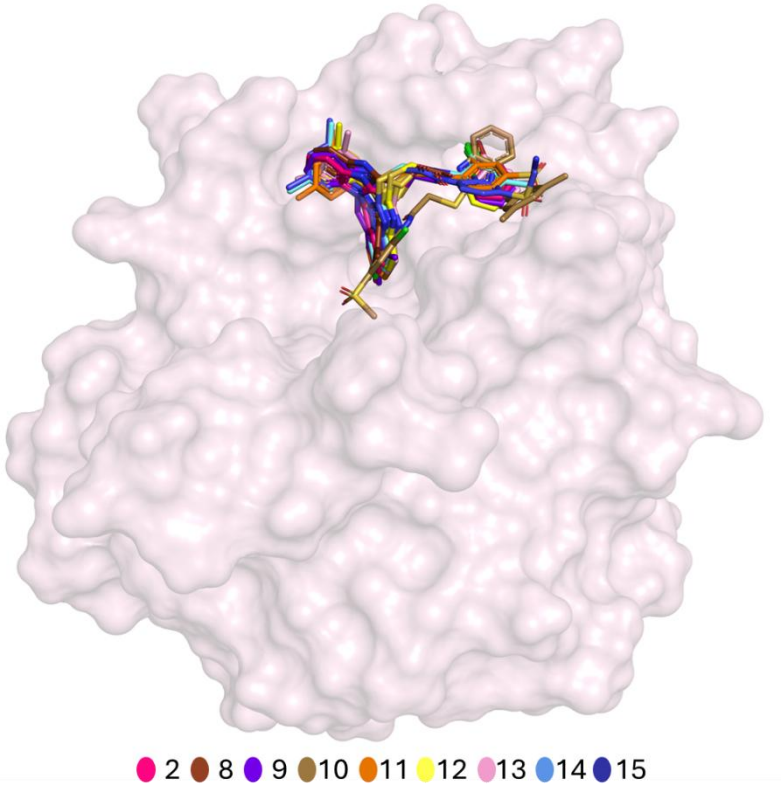

Table S3: MM-GBSA results for all eight ligands (**8**-**15**) and reference compound **2**. The calculation was performed using the Prime MM-GBSA module of the Schrödinger Suite on protein–ligand complexes that were previously minimized using the *Refine Protein–Ligand Complex*.[26]

ID	MM-GBSA (Kcal/mol)
2	-105.11
8	-91.44
9	-101.83
10	-91.24
11	-97.89
12	-111.38
13	-112.34
14	-109.74
15	-103.95

Table S4: Individual RMSD plots for compounds **12** and **13** obtained from three independent 500 ns molecular dynamics simulation replicas. Panels A, C, and E correspond to replicas 1, 2, and 3 of compound **12**, respectively, while panels B, D, and F show replicas 1, 2, and 3 of compound **13.**

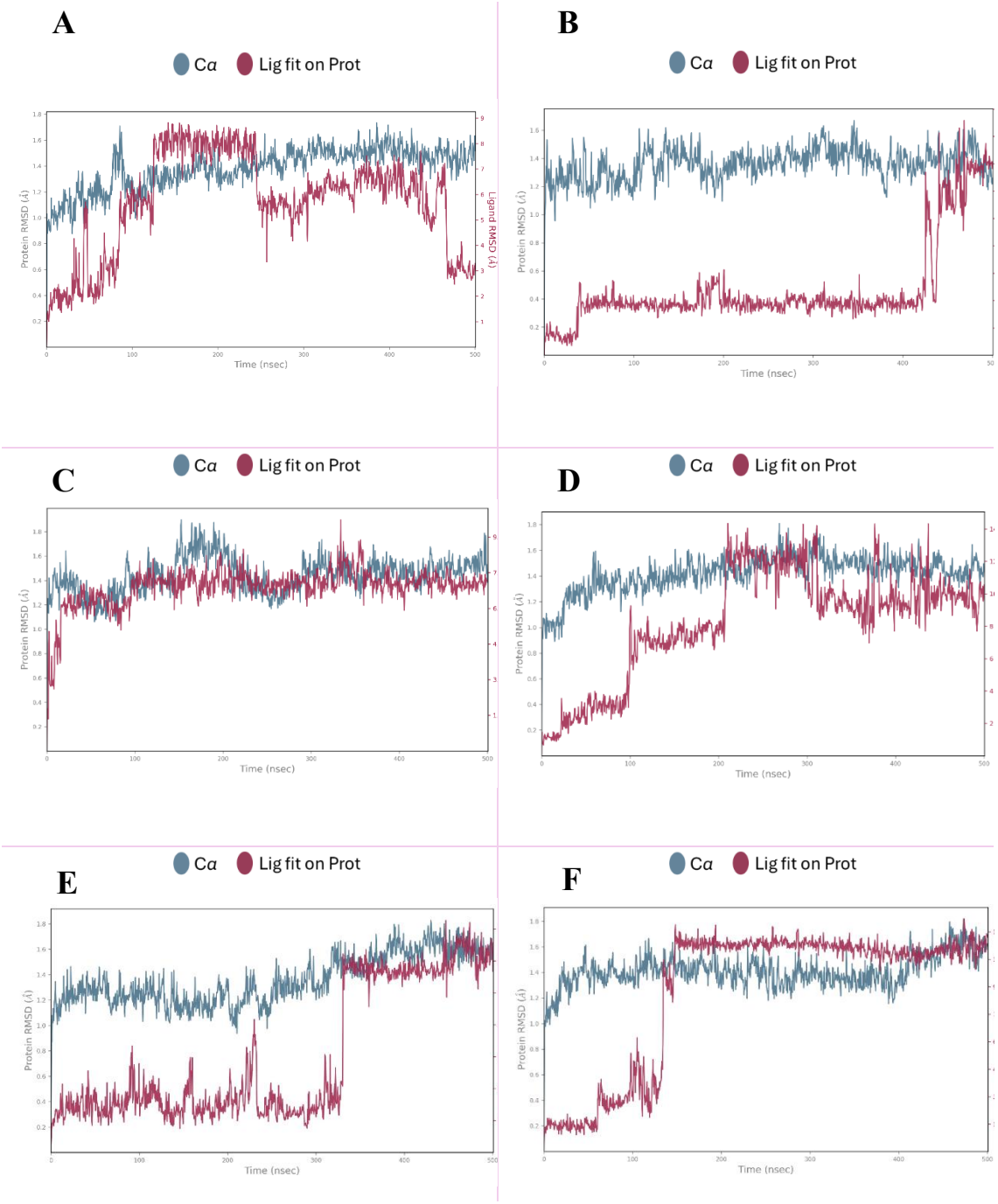

5.3 SUPPLEMENTARY MATERIAL: EXPERIMENTAL SECTION 4.1

Table S5: Physicochemical properties for compounds **1-5**, MehT-3 and Thiamidol calculated with SwissADME.[37]

	Physicochemical properties					
ID	Molecular weight (g/mol)	Num. heavy atoms	Num. arom. heavy atoms	Num. rotatable bonds	HBA	HBD
1	326.35	24	12	4	4	2
2	299.32	22	12	3	4	2
3	220.27	16	6	2	2	1
4	277.32	20	6	5	3	2
5	234.29	17	6	3	2	1
MehT-3	312.36	23	12	4	3	1
Thiamidol	278.33	19	11	4	4	3

Table S6: Druglikeness properties for reference compounds Meht-3 and Thiamidol and compounds **1-5** calculated with SwissADME.[37]

	Druglikeness							
ID	Lipinski	Ghose	Veber	Egan	Muegge	Bioavaibility Score	Pains	Brenk
1	YES	YES	YES	YES	YES	0.55	0	0
2	YES	YES	YES	YES	YES	0.56	0	0
3	YES	YES	YES	YES	YES	0.55	0	0
4	YES	YES	YES	YES	YES	0.55	0	0
5	YES	YES	YES	YES	YES	0.55	0	0
MehT-3	YES	YES	YES	YES	YES	0.55	0	0
Thiamidol	YES	YES	YES	YES	YES	0.55	0	0

Table S7: 2D plots of the interactions between compounds **1-5** and AbTYR. Pictures were generated by the ligand interaction diagram available in Maestro.[26] Violet is positively charged residues, green represents hydrophobic residues, red is negatively charged, cyan denotes polar, and gray represents metal ions.

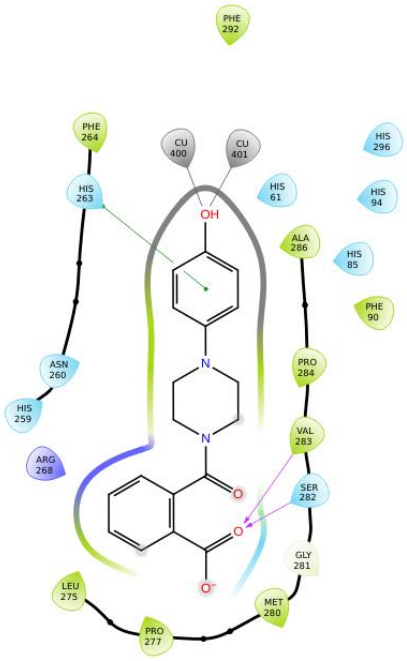

1

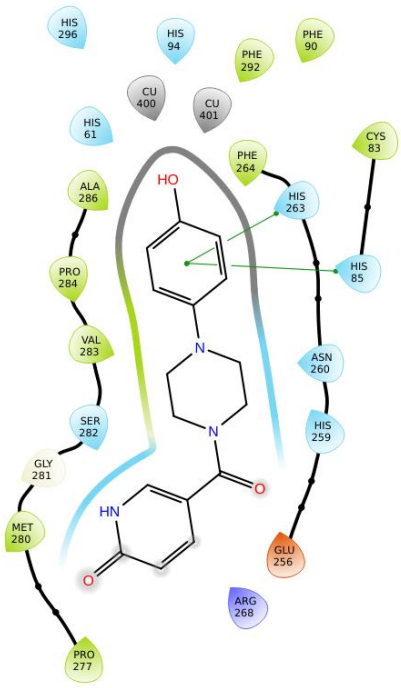

2

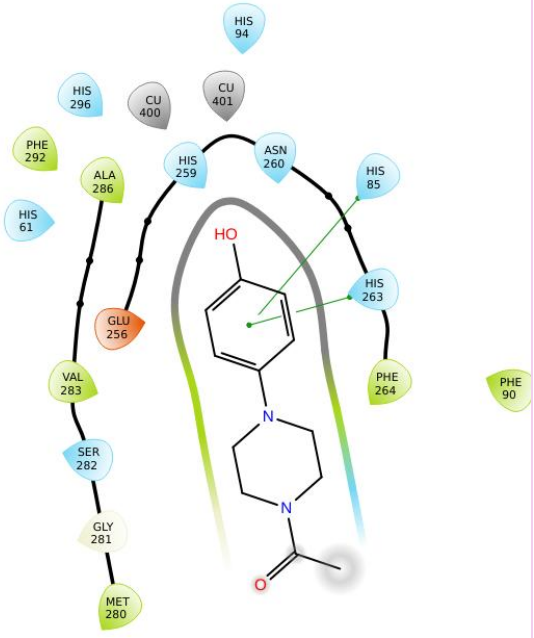

3

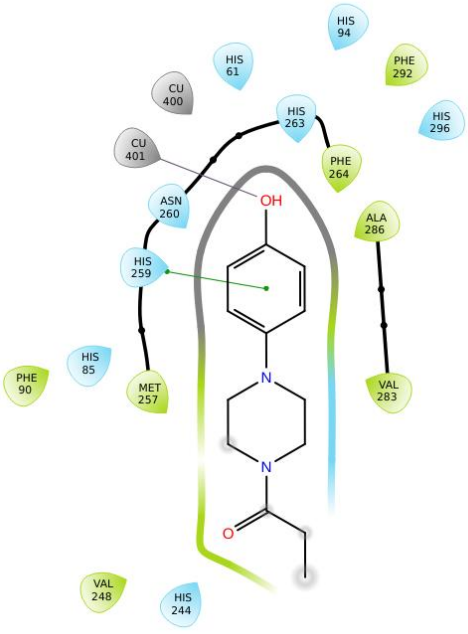

4

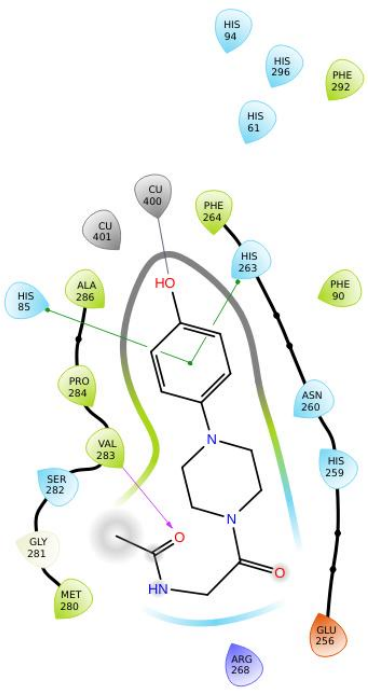
HIS 94
HIS 296
PHE 292
HIS 61
CU 400
CU 401
PHE 264
HIS 263
PHE 90
HO
HIS 85
ALA 286
PRO 284
ASN 260
VAL 283
HIS 259
SER 282
N
N
O
O
GLY 281
HN
MET 280
GLU 256
ARG 268

5

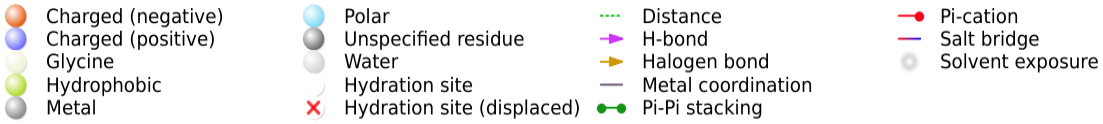
Charged (negative)
Charged (positive)
Glycine
Hydrophobic
Metal
Polar
Unspecified residue
Water
Hydration site
Hydration site (displaced)
Distance
H-bond
Halogen bond
Metal coordination
Pi-Pi stacking
Pi-cation
Salt bridge
Solvent exposure

Table S8: 2D plots of the interactions between compounds **1-5** and the homology model of hTYR. Pictures were generated by the ligand interaction diagram available in Maestro.[26] Violet is positively charged residues, green represents hydrophobic residues, red is negatively charged, cyan denotes polar, and gray represents metal ions.

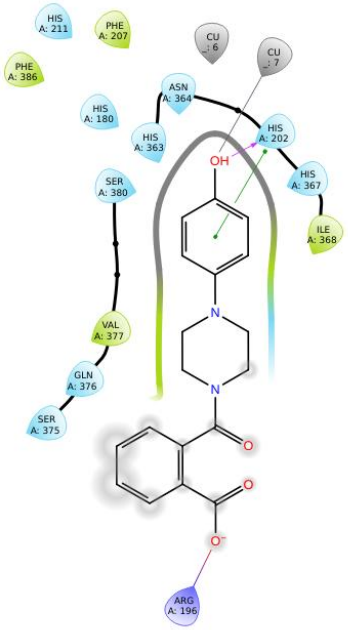

1

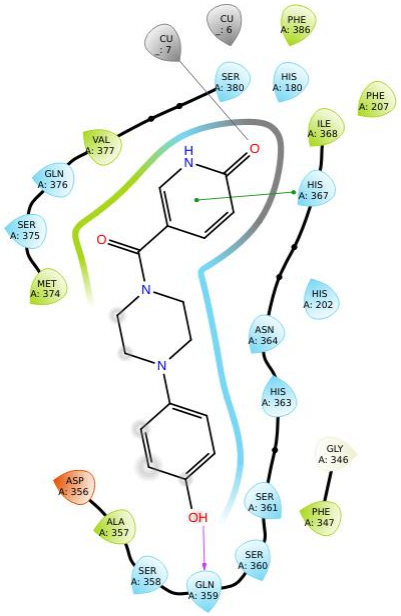

2

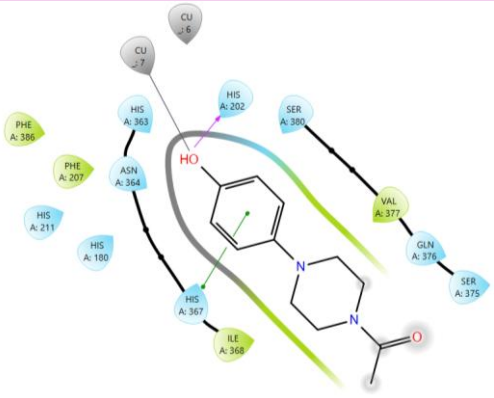

3

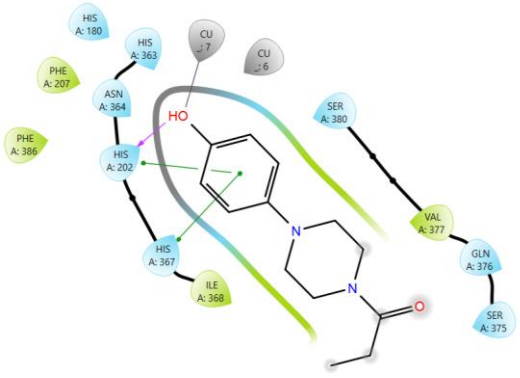

4

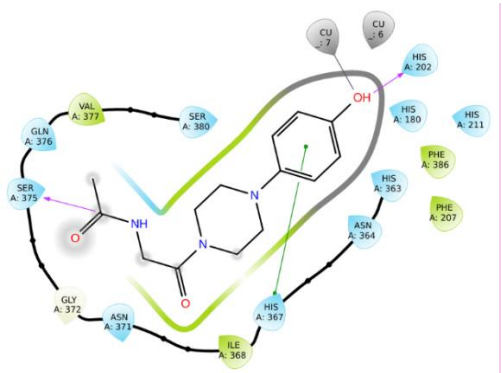
CU
: 7
CU
: 6
HIS
A: 202
OH
HIS
A: 180
HIS
A: 211
PHE
A: 386
HIS
A: 363
PHE
A: 207
ASN
A: 364
HIS
A: 367
ILE
A: 368
ASN
A: 371
GLY
A: 372
SER
A: 375
GLN
A: 376
VAL
A: 377
SER
A: 380
NH
O
N
N
O

5

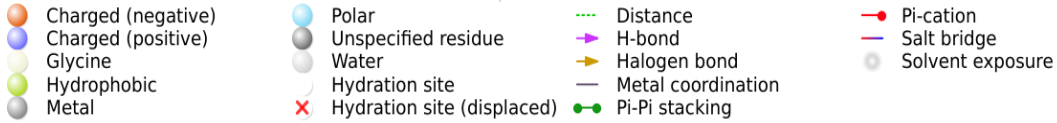
Charged (negative)
Charged (positive)
Glycine
Hydrophobic
Metal
Polar
Unspecified residue
Water
Hydration site
Hydration site (displaced)
Distance
H-bond
Halogen bond
Metal coordination
Pi-Pi stacking
Pi-cation
Salt bridge
Solvent exposure

BIBLIOGRAPHY

1. Zhang Y, Luo M, Wu P, et al. Application of Computational Biology and Artificial Intelligence in Drug Design. Int J Mol Sci 2022;23(21), doi:10.3390/ijms232113568
2. Song CM, Lim SJ, Tong JC. Recent advances in computer-aided drug design. Brief Bioinform 2009;10(5):579-91, doi:10.1093/bib/bbp023
3. Moro S, Bacilieri M, Deflorian F. Combining ligand-based and structure-based drug design in the virtual screening arena. Expert Opin Drug Discov 2007;2(1):37-49, doi:10.1517/17460441.2.1.37
4. Bassani D, Moro S. Past, Present, and Future Perspectives on Computer-Aided Drug Design Methodologies. Molecules 2023;28(9), doi:10.3390/molecules28093906
5. Niazi SK, Mariam Z. Computer-Aided Drug Design and Drug Discovery: A Prospective Analysis. Pharmaceuticals (Basel) 2023;17(1), doi:10.3390/ph17010022
6. Wu Z, Chen S, Wang Y, et al. Current perspectives and trend of computer-aided drug design: a review and bibliometric analysis. Int J Surg 2024;110(6):3848-3878, doi:10.1097/JS9.0000000000001289
7. Baig MH, Ahmad K, Roy S, et al. Computer Aided Drug Design: Success and Limitations. Curr Pharm Des 2016;22(5):572-81, doi:10.2174/1381612822666151125000550
8. Hasan MR, Alsaiari AA, Fakhurji BZ, et al. Application of Mathematical Modeling and Computational Tools in the Modern Drug Design and Development Process. Molecules 2022;27(13), doi:10.3390/molecules27134169
9. Seidel T, Wieder O, Garon A, et al. Applications of the Pharmacophore Concept in Natural Product inspired Drug Design. Mol Inform 2020;39(11):e2000059, doi:10.1002/minf.202000059
10. Macalino SJ, Gosu V, Hong S, et al. Role of computer-aided drug design in modern drug discovery. Arch Pharm Res 2015;38(9):1686-701, doi:10.1007/s12272-015-0640-5
11. Sastry GM, Adzhigirey M, Day T, et al. Protein and ligand preparation: parameters, protocols, and influence on virtual screening enrichments. J Comput Aided Mol Des 2013;27(3):221-34, doi:10.1007/s10822-013-9644-8
12. Jacobson MP, Pincus DL, Rapp CS, et al. A hierarchical approach to all-atom protein loop prediction. Proteins 2004;55(2):351-67, doi:10.1002/prot.10613
13. Pedretti A, Villa L, Vistoli G. VEGA--an open platform to develop chemo-bio-informatics applications, using plug-in architecture and script programming. J Comput Aided Mol Des 2004;18(3):167-73, doi:10.1023/b:jcam.0000035186.90683.f2
14. Xu M, Lill MA. Induced fit docking, and the use of QM/MM methods in docking. Drug Discov Today Technol 2013;10(3):e411-8, doi:10.1016/j.ddtec.2013.02.003
15. Amaro RE, Baudry J, Chodera J, et al. Ensemble Docking in Drug Discovery. Biophys J 2018;114(10):2271-2278, doi:10.1016/j.bpj.2018.02.038
16. Dhar A, Sisk TR, Robustelli P. Ensemble docking for intrinsically disordered proteins. bioRxiv 2025, doi:10.1101/2025.01.23.634614
17. Yan D, Ma Y, Chen X, et al. Molecular dynamics-driven drug discovery. Phys Chem Chem Phys 2025;27(24):12633-12651, doi:10.1039/d5cp00380f
18. Collier TA, Piggot TJ, Allison JR. Molecular Dynamics Simulation of Proteins. Methods Mol Biol 2020;2073(311-327, doi:10.1007/978-1-4939-9869-2_17

19. Vymětal J, Jurásková V, Vondrášek J. AMBER and CHARMM Force Fields Inconsistently Portray the Microscopic Details of Phosphorylation. J Chem Theory Comput 2019;15(1):665-679, doi:10.1021/acs.jctc.8b00715
20. Gargano S, Iacoviello DF, Iacovelli F, et al. Comparison among Amber-ff14SB, Amber-ff19SB, and CHARMM36 Force Fields for Ionic and Electroosmotic Flows in Biological Nanopores. J Chem Theory Comput 2025;21(22):11772-11782, doi:10.1021/acs.jctc.5c01032
21. Wang J, Wolf RM, Caldwell JW, et al. Development and testing of a general amber force field. J Comput Chem 2004;25(9):1157-74, doi:10.1002/jcc.20035
22. Lu C, Wu C, Ghoreishi D, et al. OPLS4: Improving Force Field Accuracy on Challenging Regimes of Chemical Space. J Chem Theory Comput 2021;17(7):4291-4300, doi:10.1021/acs.jctc.1c00302
23. Genheden S, Ryde U. The MM/PBSA and MM/GBSA methods to estimate ligand-binding affinities. Expert Opin Drug Discov 2015;10(5):449-61, doi:10.1517/17460441.2015.1032936
24. Wolber G, Langer T. LigandScout: 3-D pharmacophores derived from protein-bound ligands and their use as virtual screening filters. J Chem Inf Model 2005;45(1):160-9, doi:10.1021/ci049885e
25. Kainrad T, Hunold S, Seidel T, et al. LigandScout Remote: A New User-Friendly Interface for HPC and Cloud Resources. J Chem Inf Model 2019;59(1):31-37, doi:10.1021/acs.jcim.8b00716
26. Schrödinger Release 2025-4 : Maestro S, LLC, New York, NY, 2025.
27. Johnston RC, Yao K, Kaplan Z, et al. Epik: p. J Chem Theory Comput 2023;19(8):2380-2388, doi:10.1021/acs.jctc.3c00044
28. Yan Y, Yang M, Ji CG, et al. Interaction Entropy for Computational Alanine Scanning. J Chem Inf Model 2017;57(5):1112-1122, doi:10.1021/acs.jcim.6b00734
29. Kortemme T, Baker D. A simple physical model for binding energy hot spots in protein-protein complexes. Proc Natl Acad Sci U S A 2002;99(22):14116-21, doi:10.1073/pnas.202485799
30. Bhachoo J, Beuming T. Investigating Protein-Peptide Interactions Using the Schrödinger Computational Suite. Methods Mol Biol 2017;1561(235-254, doi:10.1007/978-1-4939-6798-8_14
31. Li J, Abel R, Zhu K, et al. The VSGB 2.0 model: a next generation energy model for high resolution protein structure modeling. Proteins 2011;79(10):2794-812, doi:10.1002/prot.23106
32. Shivakumar D, Williams J, Wu Y, et al. Prediction of Absolute Solvation Free Energies using Molecular Dynamics Free Energy Perturbation and the OPLS Force Field. J Chem Theory Comput 2010;6(5):1509-19, doi:10.1021/ct900587b
33. Smith MD, Rao JS, Segelken E, et al. Force-Field Induced Bias in the Structure of Aβ21-30: A Comparison of OPLS, AMBER, CHARMM, and GROMOS Force Fields. J Chem Inf Model 2015;55(12):2587-95, doi:10.1021/acs.jcim.5b00308
34. Jones G, Willett P, Glen RC, et al. Development and validation of a genetic algorithm for flexible docking. J Mol Biol 1997;267(3):727-48, doi:10.1006/jmbi.1996.0897
35. Verdonk ML, Cole JC, Hartshorn MJ, et al. Improved protein-ligand docking using GOLD. Proteins 2003;52(4):609-23, doi:10.1002/prot.10465

36. Liebeschuetz JW, Cole JC, Korb O. Pose prediction and virtual screening performance of GOLD scoring functions in a standardized test. J Comput Aided Mol Des 2012;26(6):737-48, doi:10.1007/s10822-012-9551-4
37. Daina A, Michielin O, Zoete V. SwissADME: a free web tool to evaluate pharmacokinetics, drug-likeness and medicinal chemistry friendliness of small molecules. Sci Rep 2017;7(42717, doi:10.1038/srep42717
38. Daina A, Michielin O, Zoete V. iLOGP: a simple, robust, and efficient description of n-octanol/water partition coefficient for drug design using the GB/SA approach. J Chem Inf Model 2014;54(12):3284-301, doi:10.1021/ci500467k
39. Daina A, Zoete V. A BOILED-Egg To Predict Gastrointestinal Absorption and Brain Penetration of Small Molecules. ChemMedChem 2016;11(11):1117-21, doi:10.1002/cmdc.201600182
40. Pires DE, Blundell TL, Ascher DB. pkCSM: Predicting Small-Molecule Pharmacokinetic and Toxicity Properties Using Graph-Based Signatures. J Med Chem 2015;58(9):4066-72, doi:10.1021/acs.jmedchem.5b00104
41. The PyMOL Molecular Graphics System VS, LLC.
42. Mooers BHM. Shortcuts for faster image creation in PyMOL. Protein Sci 2020;29(1):268-276, doi:10.1002/pro.3781
43. Rigsby RE, Parker AB. Using the PyMOL application to reinforce visual understanding of protein structure. Biochem Mol Biol Educ 2016;44(5):433-7, doi:10.1002/bmb.20966
44. Khavkin J, Ellis DA. Aging skin: histology, physiology, and pathology. Facial Plast Surg Clin North Am 2011;19(2):229-34, doi:10.1016/j.fsc.2011.04.003
45. Svitina H, Swanepoel R, Rossouw J, et al. Treatment of Skin Disorders with Aloe Materials. Curr Pharm Des 2019;25(20):2208-2240, doi:10.2174/1381612825666190703154244
46. Csekes E, Račková L. Skin Aging, Cellular Senescence and Natural Polyphenols. Int J Mol Sci 2021;22(23), doi:10.3390/ijms222312641
47. Fore J. A review of skin and the effects of aging on skin structure and function. Ostomy Wound Manage 2006;52(9):24-35; quiz 36-7
48. Naharro-Rodriguez J, Bacci S, Hernandez-Bule ML, et al. Decoding Skin Aging: A Review of Mechanisms, Markers, and Modern Therapies. Cosmetics 2025;12(4):144
49. Farage MA, Miller KW, Elsner P, et al. Intrinsic and extrinsic factors in skin ageing: a review. Int J Cosmet Sci 2008;30(2):87-95, doi:10.1111/j.1468-2494.2007.00415.x
50. Chaudhary M, Khan A, Gupta M. Skin Ageing: Pathophysiology and Current Market Treatment Approaches. Curr Aging Sci 2020;13(1):22-30, doi:10.2174/1567205016666190809161115
51. McCullough JL, Kelly KM. Prevention and treatment of skin aging. Ann N Y Acad Sci 2006;1067(323-31, doi:10.1196/annals.1354.044
52. Baumann L. Skin ageing and its treatment. J Pathol 2007;211(2):241-51, doi:10.1002/path.2098
53. Scheau C, Badarau IA, Mihai LG, et al. Cannabinoids in the Pathophysiology of Skin Inflammation. Molecules 2020;25(3), doi:10.3390/molecules25030652
54. Pająk J, Nowicka D, Szepietowski JC. Inflammaging and Immunosenescence as Part of Skin Aging-A Narrative Review. Int J Mol Sci 2023;24(9), doi:10.3390/ijms24097784

55. Agrawal R, Hu A, Bollag WB. The Skin and Inflamm-Aging. Biology (Basel) 2023;12(11), doi:10.3390/biology12111396
56. Thawabteh AM, Jibreen A, Karaman D, et al. Skin Pigmentation Types, Causes and Treatment-A Review. Molecules 2023;28(12), doi:10.3390/molecules28124839
57. Lee AY. Skin Pigmentation Abnormalities and Their Possible Relationship with Skin Aging. Int J Mol Sci 2021;22(7), doi:10.3390/ijms22073727
58. Davis EC, Callender VD. Postinflammatory hyperpigmentation: a review of the epidemiology, clinical features, and treatment options in skin of color. J Clin Aesthet Dermatol 2010;3(7):20-31
59. Slominski A, Tobin DJ, Shibahara S, et al. Melanin pigmentation in mammalian skin and its hormonal regulation. Physiol Rev 2004;84(4):1155-228, doi:10.1152/physrev.00044.2003
60. Hussein RS, Bin Dayel S, Abahussein O, et al. Influences on Skin and Intrinsic Aging: Biological, Environmental, and Therapeutic Insights. J Cosmet Dermatol 2025;24(2):e16688, doi:10.1111/jocd.16688
61. Yang Y, Wu Y, Xiang L, et al. Deciphering the role of skin aging in pigmentary disorders. Free Radic Biol Med 2025;227(638-655, doi:10.1016/j.freeradbiomed.2024.12.032
62. Zeng W, Song Y, Wang R, et al. Neutrophil elastase: From mechanisms to therapeutic potential. J Pharm Anal 2023;13(4):355-366, doi:10.1016/j.jpha.2022.12.003
63. Pintus F, Floris S, Fais A, et al. Extract: Inhibition of Skin Aging-Related Enzymes and Nanoformulation. Plants (Basel) 2022;11(14), doi:10.3390/plants11141849
64. Zaidi KU, Ali SA, Ali A, et al. Natural Tyrosinase Inhibitors: Role of Herbals in the Treatment of Hyperpigmentary Disorders. Mini Rev Med Chem 2019;19(10):796-808, doi:10.2174/1389557519666190116101039
65. D'Mello SA, Finlay GJ, Baguley BC, et al. Signaling Pathways in Melanogenesis. Int J Mol Sci 2016;17(7), doi:10.3390/ijms17071144
66. Heinz A. Elastases and elastokines: elastin degradation and its significance in health and disease. Crit Rev Biochem Mol Biol 2020;55(3):252-273, doi:10.1080/10409238.2020.1768208
67. Baumann L, Bernstein EF, Weiss AS, et al. Clinical Relevance of Elastin in the Structure and Function of Skin. Aesthet Surg J Open Forum 2021;3(3):ojab019, doi:10.1093/asjof/ojab019
68. Zolghadri S, Beygi M, Mohammad TF, et al. Targeting tyrosinase in hyperpigmentation: Current status, limitations and future promises. Biochem Pharmacol 2023;212(115574, doi:10.1016/j.bcp.2023.115574
69. Li J, Feng L, Liu L, et al. Recent advances in the design and discovery of synthetic tyrosinase inhibitors. Eur J Med Chem 2021;224(113744, doi:10.1016/j.ejmech.2021.113744
70. Chang TS. An updated review of tyrosinase inhibitors. Int J Mol Sci 2009;10(6):2440-2475, doi:10.3390/ijms10062440
71. Pillaiyar T, Manickam M, Namasivayam V. Skin whitening agents: medicinal chemistry perspective of tyrosinase inhibitors. J Enzyme Inhib Med Chem 2017;32(1):403-425, doi:10.1080/14756366.2016.1256882
72. Quan T, Fisher GJ. Role of Age-Associated Alterations of the Dermal Extracellular Matrix Microenvironment in Human Skin Aging: A Mini-Review. Gerontology 2015;61(5):427-34, doi:10.1159/000371708

73. Liu HM, Cheng MY, Xun MH, et al. Possible Mechanisms of Oxidative Stress-Induced Skin Cellular Senescence, Inflammation, and Cancer and the Therapeutic Potential of Plant Polyphenols. Int J Mol Sci 2023;24(4), doi:10.3390/ijms24043755
74. Liu T, Li S, Ying S, et al. The IL-23/IL-17 Pathway in Inflammatory Skin Diseases: From Bench to Bedside. Front Immunol 2020;11(594735, doi:10.3389/fimmu.2020.594735
75. Bode W, Meyer E, Powers JC. Human leukocyte and porcine pancreatic elastase: X-ray crystal structures, mechanism, substrate specificity, and mechanism-based inhibitors. Biochemistry 1989;28(5):1951-63, doi:10.1021/bi00431a001
76. Pitasi G, Brancale A, Floris S, et al. Computational Approach to Identifying New Chemical Entities as Elastase Inhibitors with Potential Antiaging Effects. Int J Mol Sci 2024;25(20), doi:10.3390/ijms252011174
77. Imokawa G, Ishida K. Biological mechanisms underlying the ultraviolet radiation-induced formation of skin wrinkling and sagging I: reduced skin elasticity, highly associated with enhanced dermal elastase activity, triggers wrinkling and sagging. Int J Mol Sci 2015;16(4):7753-75, doi:10.3390/ijms16047753
78. Talas U, Dunlop J, Khalaf S, et al. Human elastase 1: evidence for expression in the skin and the identification of a frequent frameshift polymorphism. J Invest Dermatol 2000;114(1):165-70, doi:10.1046/j.1523-1747.2000.00825.x
79. Weiss FU, Budde C, Lerch MM. Specificity of a Polyclonal Fecal Elastase ELISA for CELA3. PLoS One 2016;11(7):e0159363, doi:10.1371/journal.pone.0159363
80. Ocampo-Gallego JS, Pedroza-Escobar D, Caicedo-Ortega AR, et al. Human neutrophil elastase inhibitors: Classification, biological-synthetic sources and their relevance in related diseases. Fundam Clin Pharmacol 2024;38(1):13-32, doi:10.1111/fcp.12946
81. Takeuchi H, Gomi T, Shishido M, et al. Neutrophil elastase contributes to extracellular matrix damage induced by chronic low-dose UV irradiation in a hairless mouse photoaging model. J Dermatol Sci 2010;60(3):151-8, doi:10.1016/j.jdermsci.2010.09.001
82. Rijken F, Bruijnzeel PL. The pathogenesis of photoaging: the role of neutrophils and neutrophil-derived enzymes. J Investig Dermatol Symp Proc 2009;14(1):67-72, doi:10.1038/jidsymp.2009.15
83. Hornebeck LRaMPJaCFaGGaW. Interaction between elastin and elastases and its role in the aging of the arterial wall, skin and other connective tissues. A review. Mechanisms of Ageing and Development 1984;28(2):155-166, doi:https://doi.org/10.1016/0047-6374(84)90015-0
84. Vanjare BD, Seok Eom Y, Raza H, et al. Elastase inhibitory activity of quinoline Analogues: Synthesis, kinetic mechanism, cytotoxicity, chemoinformatics and molecular docking studies. Bioorg Med Chem 2022;63(116745, doi:10.1016/j.bmc.2022.116745
85. Hosseini Nasab N, Raza H, Eom YS, et al. Design and synthesis of thiadiazole-oxadiazole-acetamide derivatives: Elastase inhibition, cytotoxicity, kinetic mechanism, and computational studies. Bioorg Med Chem 2023;86(117292, doi:10.1016/j.bmc.2023.117292
86. Dige NC, Mahajan PG, Raza H, et al. Synthesis and characterization of new 4H-chromene-3-carboxylates ensuring potent elastase inhibition activity along with their molecular docking and chemoinformatics properties. Bioorg Chem 2020;100(103906, doi:10.1016/j.bioorg.2020.103906

87. Sinha S, Watorek W, Karr S, et al. Primary structure of human neutrophil elastase. Proc Natl Acad Sci U S A 1987;84(8):2228-32, doi:10.1073/pnas.84.8.2228
88. Navia MA, McKeever BM, Springer JP, et al. Structure of human neutrophil elastase in complex with a peptide chloromethyl ketone inhibitor at 1.84-A resolution. Proc Natl Acad Sci U S A 1989;86(1):7-11, doi:10.1073/pnas.86.1.7
89. Hansen G, Gielen-Haertwig H, Reinemer P, et al. Unexpected active-site flexibility in the structure of human neutrophil elastase in complex with a new dihydropyrimidone inhibitor. J Mol Biol 2011;409(5):681-91, doi:10.1016/j.jmb.2011.04.047
90. The PyMOL Molecular Graphics System V, Schr{\"o}dinger, LLC.},, Author = {{Schr\"odinger L, Date-Added = {2010-08-19 17:29:55 -0400}, et al.
91. Tamada T, Kinoshita T, Kurihara K, et al. Combined high-resolution neutron and X-ray analysis of inhibited elastase confirms the active-site oxyanion hole but rules against a low-barrier hydrogen bond. J Am Chem Soc 2009;131(31):11033-40, doi:10.1021/ja9028846
92. Thomson A, Kapadia SB. The specificity of the S1 and S2 subsites of elastase. Eur J Biochem 1979;102(1):111-6, doi:10.1111/j.1432-1033.1979.tb06269.x
93. Mattos C, Rasmussen B, Ding X, et al. Analogous inhibitors of elastase do not always bind analogously. Nat Struct Biol 1994;1(1):55-8, doi:10.1038/nsb0194-55
94. Mattos C, Giammona DA, Petsko GA, et al. Structural analysis of the active site of porcine pancreatic elastase based on the X-ray crystal structures of complexes with trifluoroacetyl-dipeptide-anilide inhibitors. Biochemistry 1995;34(10):3193-203, doi:10.1021/bi00010a008
95. Würtele M, Hahn M, Hilpert K, et al. Atomic resolution structure of native porcine pancreatic elastase at 1.1 A. Acta Crystallogr D Biol Crystallogr 2000;56(Pt 4):520-3, doi:10.1107/s0907444900000299
96. Alessandro Gerace and Valentina Masini and Letizia Crocetti and Maria Paola Giovannoni and Marta F. X-ray structural study of human neutrophil elastase inhibition with a series of azaindoles, azaindazoles and isoxazolones. Journal of Molecular Structure 2023;1274(134595, doi:https://doi.org/10.1016/j.molstruc.2022.134595
97. Crocetti L, Quinn MT, Schepetkin IA, et al. A patenting perspective on human neutrophil elastase (HNE) inhibitors (2014-2018) and their therapeutic applications. Expert Opin Ther Pat 2019;29(7):555-578, doi:10.1080/13543776.2019.1630379
98. Singh V, Singh N, Pradhan A, et al. Structure-activity relationships of dihydropyrimidone inhibitors against native and auto-processed human neutrophil elastase. Comput Biol Med 2023;161(107004, doi:10.1016/j.compbiomed.2023.107004
99. Wang F, Ma W, Fan D, et al. The biochemistry of melanogenesis: an insight into the function and mechanism of melanogenesis-related proteins. Front Mol Biosci 2024;11(1440187, doi:10.3389/fmolb.2024.1440187
100. Rzepka Z, Buszman E, Beberok A, et al. From tyrosine to melanin: Signaling pathways and factors regulating melanogenesis. Postepy Hig Med Dosw (Online) 2016;70(0):695-708, doi:10.5604/17322693.1208033
101. Lee J, Park YJ, Jung HJ, et al. Design and Synthesis of (Molecules 2023;28(2), doi:10.3390/molecules28020848
102. Gillbro JM, Olsson MJ. The melanogenesis and mechanisms of skin-lightening agents--existing and new approaches. Int J Cosmet Sci 2011;33(3):210-21, doi:10.1111/j.1468-2494.2010.00616.x

103. Lee SY, Baek N, Nam TG. Natural, semisynthetic and synthetic tyrosinase inhibitors. J Enzyme Inhib Med Chem 2016;31(1):1-13, doi:10.3109/14756366.2015.1004058
104. Zolghadri S, Bahrami A, Hassan Khan MT, et al. A comprehensive review on tyrosinase inhibitors. J Enzyme Inhib Med Chem 2019;34(1):279-309, doi:10.1080/14756366.2018.1545767
105. Roulier B, Pérès B, Haudecoeur R. Advances in the Design of Genuine Human Tyrosinase Inhibitors for Targeting Melanogenesis and Related Pigmentations. J Med Chem 2020;63(22):13428-13443, doi:10.1021/acs.jmedchem.0c00994
106. Lai X, Wichers HJ, Soler-Lopez M, et al. Structure and Function of Human Tyrosinase and Tyrosinase-Related Proteins. Chemistry 2018;24(1):47-55, doi:10.1002/chem.201704410
107. Ricci F, Schira K, Khettabi L, et al. Computational methods to analyze and predict the binding mode of inhibitors targeting both human and mushroom tyrosinase. Eur J Med Chem 2023;260(115771, doi:10.1016/j.ejmech.2023.115771
108. Hassan M, Shahzadi S, Kloczkowski A. Tyrosinase Inhibitors Naturally Present in Plants and Synthetic Modifications of These Natural Products as Anti-Melanogenic Agents: A Review. Molecules 2023;28(1), doi:10.3390/molecules28010378
109. Rubbab Pasha A, Khan M, Khan A, et al. Synthesis, in vitro, and in silico study of novel pyridine based 1,3-diphenylurea derivatives as tyrosinase inhibitors. Bioorg Chem 2024;152(107724, doi:10.1016/j.bioorg.2024.107724
110. Mason KGSaRLJaHS. Quaternary structure of mushroom tyrosinase. Biochemical and Biophysical Research Communications 1976;70(2):519-524, doi:https://doi.org/10.1016/0006-291X(76)91077-9
111. Celia WGaWHFaHJW. Sequence and structural features of plant and fungal tyrosinases. Phytochemistry 1997;45(7):1309-1323, doi:https://doi.org/10.1016/S0031-9422(97)00186-6
112. Ismaya WT, Rozeboom HJ, Weijn A, et al. Crystal structure of Agaricus bisporus mushroom tyrosinase: identity of the tetramer subunits and interaction with tropolone. Biochemistry 2011;50(24):5477-86, doi:10.1021/bi200395t
113. Iwata K, Doi A, Ohji G, et al. Effect of neutrophil elastase inhibitor (sivelestat sodium) in the treatment of acute lung injury (ALI) and acute respiratory distress syndrome (ARDS): a systematic review and meta-analysis. Intern Med 2010;49(22):2423-32, doi:10.2169/internalmedicine.49.4010
114. Ohmoto K, Yamamoto T, Okuma M, et al. Development of orally active nonpeptidic inhibitors of human neutrophil elastase. J Med Chem 2001;44(8):1268-85, doi:10.1021/jm000410y
115. Siedle B, Hrenn A, Merfort I. Natural compounds as inhibitors of human neutrophil elastase. Planta Med 2007;73(5):401-20, doi:10.1055/s-2007-967183
116. Martins FT, Assis DM, Dos Santos MH, et al. Natural polyprenylated benzophenones inhibiting cysteine and serine proteases. Eur J Med Chem 2009;44(3):1230-9, doi:10.1016/j.ejmech.2008.09.018
117. Kim JY, Wang Y, Uddin Z, et al. Competitive neutrophil elastase inhibitory isoflavones from the roots of Flemingia philippinensis. Bioorg Chem 2018;78(249-257, doi:10.1016/j.bioorg.2018.03.024
118. Salvador LA, Taori K, Biggs JS, et al. Potent elastase inhibitors from cyanobacteria: structural basis and mechanisms mediating cytoprotective and anti-

inflammatory effects in bronchial epithelial cells. J Med Chem 2013;56(3):1276-90, doi:10.1021/jm3017305
119. Luo D, Chen QY, Luesch H. Total Synthesis of the Potent Marine-Derived Elastase Inhibitor Lyngbyastatin 7 and in Vitro Biological Evaluation in Model Systems for Pulmonary Diseases. J Org Chem 2016;81(2):532-44, doi:10.1021/acs.joc.5b02386
120. BIOVIA DS.
121. Tsukahara K, Takema Y, Moriwaki S, et al. Selective inhibition of skin fibroblast elastase elicits a concentration-dependent prevention of ultraviolet B-induced wrinkle formation. J Invest Dermatol 2001;117(3):671-7, doi:10.1046/j.0022-202x.2001.01450.x
122. Liu S, Deng T, Cheng H, et al. Advances in Transdermal Drug Delivery Systems and Clinical Applications in Inflammatory Skin Diseases. Pharmaceutics 2025;17(6), doi:10.3390/pharmaceutics17060746
123. Mahrous MH, Abdel-Dayem SIA, Adel IM, et al. Efficacy of Natural Products as Tyrosinase Inhibitors in Hyperpigmentation Therapy: Anti-Melanogenic or Anti-Browning Effects. Chem Biodivers 2025;e202403324, doi:10.1002/cbdv.202403324
124. Boo YC. Arbutin as a Skin Depigmenting Agent with Antimelanogenic and Antioxidant Properties. Antioxidants (Basel) 2021;10(7), doi:10.3390/antiox10071129
125. Beaumet M, Haudecoeur R. Hydroquinone causes exogenous ochronosis through tyrosinase catalytic activity and highlights the need for genuine human tyrosinase inhibitors. Br J Dermatol 2025;193(5):817-818, doi:10.1093/bjd/ljaf315
126. Saeedi M, Eslamifar M, Khezri K. Kojic acid applications in cosmetic and pharmaceutical preparations. Biomed Pharmacother 2019;110(582-593, doi:10.1016/j.biopha.2018.12.006
127. Espín JC, Wichers HJ. Slow-binding inhibition of mushroom (Agaricus bisporus) tyrosinase isoforms by tropolone. J Agric Food Chem 1999;47(7):2638-44, doi:10.1021/jf981055b
128. Beaumet M, Lazinski LM, Maresca M, et al. Tyrosinase Inhibition and Antimelanogenic Effects of Resorcinol-Containing Compounds. ChemMedChem 2024;19(23):e202400314, doi:10.1002/cmdc.202400314
129. Arrowitz C, Schoelermann AM, Mann T, et al. Effective Tyrosinase Inhibition by Thiamidol Results in Significant Improvement of Mild to Moderate Melasma. J Invest Dermatol 2019;139(8):1691-1698.e6, doi:10.1016/j.jid.2019.02.013
130. Mann T, Gerwat W, Batzer J, et al. Inhibition of Human Tyrosinase Requires Molecular Motifs Distinctively Different from Mushroom Tyrosinase. J Invest Dermatol 2018;138(7):1601-1608, doi:10.1016/j.jid.2018.01.019
131. Ni X, Luo X, Jiang X, et al. Small-Molecule Tyrosinase Inhibitors for Treatment of Hyperpigmentation. Molecules 2025;30(4), doi:10.3390/molecules30040788
132. Vittorio S, Dank C, Ielo L. Heterocyclic Compounds as Synthetic Tyrosinase Inhibitors: Recent Advances. Int J Mol Sci 2023;24(10), doi:10.3390/ijms24109097
133. Draelos ZD. Cosmeceuticals: undefined, unclassified, and unregulated. Clin Dermatol 2009;27(5):431-4, doi:10.1016/j.clindermatol.2009.05.005
134. Martin KI, Glaser DA. Cosmeceuticals: the new medicine of beauty. Mo Med 2011;108(1):60-3
135. Lau M, Mineroff Gollogly J, Wang JY, et al. Cosmeceuticals for antiaging: a systematic review of safety and efficacy. Arch Dermatol Res 2024;316(5):173, doi:10.1007/s00403-024-02908-2
136. Crous C, Pretorius J, Petzer A. Overview of popular cosmeceuticals in dermatology. Skin Health Dis 2024;4(2):e340, doi:10.1002/ski2.340

137. Draelos ZD. Cosmeceuticals: efficacy and influence on skin tone. Dermatol Clin 2014;32(2):137-43, doi:10.1016/j.det.2013.12.002
138. Murphy MJ, Dow AA. Natural Cosmeceutical Ingredients for the Management of Hyperpigmentation in Hispanic and Latino Women. J Clin Aesthet Dermatol 2021;14(8):52-56
139. Roggenkamp D, Sammain A, Fürstenau M, et al. Thiamidol. J Dermatol 2021;48(12):1871-1876, doi:10.1111/1346-8138.16080
140. Quan T. Human Skin Aging and the Anti-Aging Properties of Retinol. Biomolecules 2023;13(11), doi:10.3390/biom13111614
141. Peisach E, Casebier D, Gallion SL, et al. Interaction of a peptidomimetic aminimide inhibitor with elastase. Science 1995;269(5220):66-9, doi:10.1126/science.7604279
142. Wilmouth RC, Westwood NJ, Anderson K, et al. Inhibition of elastase by N-sulfonylaryl beta-lactams: anatomy of a stable acyl-enzyme complex. Biochemistry 1998;37(50):17506-13, doi:10.1021/bi9816249
143. Simon JFMaMDDaLAHaPSaMRJaGGAIaGD. The discovery of a potent, intracellular, orally bioavailable, long duration inhibitor of human neutrophil elastase—GW311616A a development candidate. Bioorganic & Medicinal Chemistry Letters 2001;11(7):895-898, doi:https://doi.org/10.1016/S0960-894X(01)00078-6
144. Meyer EFJaPLGaRR. Stereospecific reaction of 3-methoxy-4-chloro-7-aminoisocoumarin with crystalline porcine pancreatic elastase. Journal of the American Chemical Society 1985;107(13):4091-4093, doi:10.1021/ja00299a063
145. Anna-Maria Monforte and Stefania Ferro and Laura and Giuseppa and Francesca Morreale and Christophe Pannecouque and Jan Balzarini and Alba C. Design and synthesis of N1-aryl-benzimidazoles 2-substituted as novel HIV-1 non-nucleoside reverse transcriptase inhibitors. Bioorganic & Medicinal Chemistry 2014;22(4):1459-1467, doi:https://doi.org/10.1016/j.bmc.2013.12.045
146. Ingegneri M, Braghini MR, Piccione M, et al. Pomace as a Source of Plant Complexes to Be Used in the Nutraceutical Field of Intestinal Inflammation. Antioxidants (Basel) 2024;13(7), doi:10.3390/antiox13070869
147. Rajnochová Svobodová A, Gabrielová E, Michaelides L, et al. UVA-photoprotective potential of silymarin and silybin. Arch Dermatol Res 2018;310(5):413-424, doi:10.1007/s00403-018-1828-6

Finanziato dall'Unione europea NextGenerationEU
Ministero dell'Università e della Ricerca
Italiadomani PIANO NAZIONALE DI RIPRESA E RESILIENZA
Università degli Studi di Messina

The PhD scholarship was funded under “I.3.3 Borse PNRR-Dottorati innovativi che rispondono ai fabbisogni di innovazione delle imprese”, XXXVIII cycle, DM352/2022.